

POLITECNICO DI MILANO

Facoltà di Ingegneria Industriale

Corso di Laurea in
Ingegneria Aeronautica



Thermal Fluid-Structure-Interaction on a Flat-Plate Model
in Hypersonic High-Enthalpy Flow

Relatore: Prof. Luigi VIGEVANO

Co-relatore: Dr.-Ing. Burkard ESSER

Tesi di Laurea di:

Marco COSTANTINI Matr. 720000

Anno Accademico 2008 – 2009

Table of contents

1.	INTRODUCTION.....	1
1.1	Work motivation and overview.....	2
1.2	Physical aspects along the re-entry.....	3
1.2.1	Aerothermodynamic effects.....	5
1.3	Surface characteristics.....	9
1.4	Design tools.....	10
2.	NUMERICAL TOOLS.....	15
2.1	Thermal analysis.....	15
2.2	Flow solver.....	17
2.3	Coupling methodology.....	21
3.	EXPERIMENTAL SET-UP.....	23
3.1	Arc-heated facility L3K.....	23
3.2	Temperature measurement system.....	27
3.2.1	Thermocouples.....	27
3.2.2	Optical temperature measurement technique.....	28
3.2.2.1	Pyrometers.....	30
3.2.2.2	Infrared cameras.....	32
3.2.3	Window transmittance calibration.....	33
3.2.4	Pyrometers' calibration.....	35
3.2.5	Temperature measurement accuracy.....	36
4.	PRELIMINARY NUMERICAL INVESTIGATIONS.....	39
4.1	Flow modeling.....	41
4.2	Structure modeling.....	42
4.3	Perfect gas computations.....	44

Table of contents

4.4	Model flow in thermochemical non-equilibrium	57
4.5	Divergent flow	69
4.6	Nozzle flow in thermochemical non-equilibrium.....	79
4.7	Summary of the results	87
5.	INVESTIGATIONS ON THE FLAT-PLATE MODEL	91
5.1	Investigated model and experimental campaign	91
5.1.1	Experimental results	98
5.1.2	Post-processing of the experimental data	112
5.2	Numerical investigations on the flat-plate model	115
5.3	Comparison of the results	124
5.4	Further numerical investigations	127
5.4.1	Full-catalytic behaviour of the surface	127
5.4.2	Imperfect thermal contact between horizontal plate and neighbouring components...	132
6.	CONCLUSIONS AND FINAL REMARKS	137
	APPENDIX A.....	139
	APPENDIX B.....	140
	APPENDIX C.....	142
	NOMENCLATURE	143
	BIBLIOGRAPHY.....	147

List of figures

1.2.1. Flow regimes encompassed along a re-entry trajectory	4
1.2.1.1. Aerothermodynamic collar.....	5
1.2.1.2. Vibrational and chemical phenomena for air in dependence on temperature and pressure.....	7
1.2.1.3. Partially catalytic behaviour of SiC and SiO ₂ at high temperature in presence of atomic oxygen and nitrogen.....	8
3.1.1. Schematic description of the arc-heated facilities L2K and L3K at DLR.....	23
3.1.2. Mass fractions distribution on the facility's centerline.....	26
3.1.3. N ₂ vibrational temperature along the facility's centerline and facility contour.....	26
3.2.1.1. Sketch of a thermocouple.....	27
3.2.2.1. Sketch of an optical device for temperature measurements.....	28
3.2.2.1.1. Temperature uncertainty at $\lambda=1\ \mu\text{m}$	31
3.2.2.2.1. Temperature uncertainty at $\lambda=10\ \mu\text{m}$	33
3.2.3.1. Sketch of the set-up for window transmittance calibration.....	34
4.1. Bi-dimensional investigated model.....	39
4.1.1. Fluid domain with initial mesh.....	41
4.2.1. Solved structure field and relative coordinate system.....	43
4.2.2. Quasi-structured mesh on the rear side.....	43
4.2.3. Sketch of the thermal load interpolation onto the structure nodes and of the temperature b.c. interpolation onto the flow nodes.....	44
4.3.1. Distribution of temperature and Mach number in the flowfield. Perfect gas modeling. $\alpha=10^\circ$	46
4.3.2. Distribution of temperature and Mach number in the flowfield. Perfect gas modeling. $\alpha=20^\circ$	47
4.3.3. Distribution of temperature and Mach number in the flowfield. Perfect gas modeling. $\alpha=30^\circ$	48
4.3.4. Temperature distribution on the coupling surface. Perfect gas modeling with radiative equilibrium boundary condition.....	49
4.3.5. Heat flux distribution on the coupling surface. Perfect gas modeling with radiative equilibrium boundary condition.....	50
4.3.6. Temperature distribution inside the structure (30° case).....	51
4.3.7. Distribution of the x - and z - components of the heat flux inside the structure (30° case).....	51
4.3.8. Qualitative heat flux vector distribution in the structure (30° case).....	52
4.3.9. Temperature distribution on the coupling surface. Perfect gas modeling with fluid-structure interaction (1 st coupling) and comparison with the uncoupled results.....	53
4.3.10. Heat flux distribution on the coupling surface. Perfect gas modeling with fluid-structure interaction (1 st coupling) and comparison with the uncoupled results.....	54
4.3.11. Temperature distribution on the coupling surface. Perfect gas modeling with fluid-structure interaction. Comparison between 1 st and 4 th coupling results.....	55
4.3.12. Heat flux distribution on the coupling surface. Perfect gas modeling with fluid-structure interaction. Comparison between 1 st and 4 th coupling results.....	55
4.3.13. Heat flux distribution on the coupling surface. Relationship between components of the heat flux and comparison with the acting load.....	57
4.4.1. Distribution of temperature and Mach number in the flowfield. Model flow in thermochemical non-equilibrium. $\alpha=10^\circ$	59

List of figures

4.4.2. Distribution of temperature and Mach number in the flowfield. Model flow in thermochemical non-equilibrium. $\alpha=20^\circ$.	60
4.4.3. Comparison of the temperature profiles in perpendicular direction and zoom in proximity of the surface. 10° configuration.	61
4.4.4. Temperature distribution on the coupling surface. Gas in thermochemical non-equilibrium with radiative equilibrium b.c. and comparison with perfect gas modeling.	61
4.4.5. Heat flux distribution on the coupling surface. Gas in thermochemical non-equilibrium with radiative equilibrium b.c. and comparison with perfect gas modeling.	62
4.4.6. N_2 and NO mass fraction profiles with respect to z -coordinate. Gas in thermochemical non-equilibrium with radiative equilibrium b.c. – 10° configuration.	63
4.4.7. O_2 and O mass fraction profiles with respect to z -coordinate. Gas in thermochemical non-equilibrium with radiative equilibrium b.c. – 10° configuration.	64
4.4.8. N mass fraction and density profiles with respect to z -coordinate. Gas in thermochemical non-equilibrium with radiative equilibrium b.c. – 10° configuration.	64
4.4.9. Temperature distribution on the coupling surface. Gas in thermochemical non-equilibrium with fluid-structure interaction and comparison with perfect gas modeling.	67
4.4.10. Heat flux distribution on the coupling surface. Gas in thermochemical non-equilibrium with fluid-structure interaction and comparison with perfect gas modeling.	67
4.5.1. Considered flow domain inside the L3K facility and its discretization.	70
4.5.2. Mach number distribution in the solved domain. Gas in chemical non-equilibrium and thermodynamic equilibrium.	71
4.5.3. Mass fractions distribution in the facility along the central streamline. Gas in chemical non-equilibrium and thermodynamic equilibrium.	71
4.5.4. Facility mesh and model mesh set up for first interpolation – 10° configuration.	72
4.5.5. Distribution of temperature and Mach number together with the velocity vectors in the flowfield. Divergent flow. $\alpha=10^\circ$.	74
4.5.6. Distribution of temperature and Mach number together with the velocity vectors in the flowfield. Divergent flow. $\alpha=20^\circ$.	75
4.5.7. Temperature distribution on the coupling surface. Divergent flow with radiative equilibrium b.c. and comparison with uniform flow.	76
4.5.8. Temperature distribution along the flow domain in correspondence to $z=0.001$ m. Comparison between divergent and uniform stream. 20° configuration.	76
4.5.9. Heat flux distribution on the coupling surface. Divergent flow with radiative equilibrium b.c. and comparison with uniform flow.	77
4.5.10. Temperature distribution on the coupling surface. Divergent flow with fluid-structure interaction and comparison with uniform flow.	78
4.5.11. Heat flux distribution on the coupling surface. Divergent flow with fluid-structure interaction and comparison with uniform flow.	79
4.6.1. Mach number distribution in the solved field. Gas in thermochemical non-equilibrium.	80
4.6.2. Distribution of temperature and Mach number in the flowfield. Nozzle flow in thermochemical non-equilibrium. $\alpha=10^\circ$.	81
4.6.3. Distribution of temperature and Mach number in the flowfield. Nozzle flow in thermochemical non-equilibrium. $\alpha=20^\circ$.	82
4.6.4. Distribution of temperature and Mach number in the flowfield. Nozzle flow in thermochemical non-equilibrium. $\alpha=30^\circ$.	83
4.6.5. Temperature distribution on the coupling surface. Nozzle flow in thermochemical non-equilibrium with radiative equilibrium b.c. and comparison with perfect gas modeling.	84
4.6.6. Heat flux distribution on the coupling surface. Nozzle flow in thermochemical non-equilibrium with radiative equilibrium b.c. and comparison with perfect gas modeling.	84
4.6.7. Temperature distribution on the coupling surface. Nozzle flow in thermochemical non-equilibrium with fluid-structure interaction and comparison with perfect gas modeling.	86

4.6.8. Heat flux distribution on the coupling surface. Nozzle flow in thermochemical non-equilibrium with fluid-structure interaction and comparison with perfect gas modeling.....	87
5.1.1. Investigated model (disassembled).....	91
5.1.2. Investigated model (mounted).....	92
5.1.3. Positioning of the thermocouples. Installation on the base support and positions after the integration of the KAPYROK.....	93
5.1.4. Sketch of the positions of thermocouples and pyrometers on the model.....	95
5.1.5. L3K test chamber.....	95
5.1.6. Model inside the L3K test chamber.....	97
5.1.7. Mass flow rate and reservoir pressure time evolution. Preliminary test-001.....	97
5.1.1.1. Pyrometers measurements. Spot 2. $\alpha=10^\circ$	99
5.1.1.2. Pyrometers measurements. Spot 2. $\alpha=20^\circ$	99
5.1.1.3. Pyrometers measurements. Spot 2. $\alpha=30^\circ$	100
5.1.1.4. Pyrometers measurements. Spot 4. $\alpha=10^\circ$	100
5.1.1.5. Pyrometers measurements. Spot 4. $\alpha=20^\circ$	101
5.1.1.6. Pyrometers measurements. Spot 4. $\alpha=30^\circ$	101
5.1.1.7. Pyrometers measurements. Spot 6.....	102
5.1.1.8. Thermocouples measurements. First row. $\alpha=10^\circ$	103
5.1.1.9. Thermocouples measurements. First row. $\alpha=20^\circ$	103
5.1.1.10. Thermocouples measurements. First row. $\alpha=30^\circ$	104
5.1.1.11. Thermocouples measurements. Second row. $\alpha=10^\circ$	104
5.1.1.12. Thermocouples measurements. Second row. $\alpha=20^\circ$	105
5.1.1.13. Thermocouples measurements. Second row. $\alpha=30^\circ$	105
5.1.1.14. Thermocouples measurements. Third row. $\alpha=10^\circ$	106
5.1.1.15. Thermocouples measurements. Third row. $\alpha=20^\circ$	106
5.1.1.16. Thermocouples measurements. Third row. $\alpha=30^\circ$	107
5.1.1.17. Thermocouples measurements. Fourth row. $\alpha=10^\circ$	107
5.1.1.18. Thermocouples measurements. Fourth row. $\alpha=20^\circ$	108
5.1.1.19. Thermocouples measurements. Fourth row. $\alpha=30^\circ$	108
5.1.1.20. Thermocouples measurements. Second perpendicular position.....	109
5.1.1.21. IR-camera measurements.....	109
5.1.1.22. IR-camera measurements in lateral direction.....	110
5.1.1.23. IR-camera records.....	111
5.1.2.1. Marker points used for the post-processing.....	112
5.1.2.2. Spots used for the post-processing.....	113
5.1.2.3. Measured temperatures over the spots with the different devices.....	114
5.1.2.4. Measured temperatures on the flat-plate. Corrected values.....	115
5.2.1. Fluid domain with final mesh. – 30° configuration.....	117
5.2.2. Structure field and relative coordinate system.....	117
5.2.3. Distribution of temperature and Mach number in the flowfield. $\alpha=10^\circ$	118
5.2.4. Distribution of temperature and Mach number in the flowfield. $\alpha=20^\circ$	119
5.2.5. Distribution of temperature and Mach number in the flowfield. $\alpha=30^\circ$	120
5.2.6. Temperature distribution on the coupling surface. Perfect gas modeling with radiative equilibrium boundary condition.....	121
5.2.7. Heat flux distribution on the coupling surface. Perfect gas modeling with radiative equilibrium boundary condition.....	121
5.2.8. Temperature distribution on the coupling surface. Perfect gas modeling with fluid-structure interaction and comparison with the uncoupled results.....	123
5.2.9. Heat flux distribution on the coupling surface. Perfect gas modeling with fluid-structure interaction and comparison with the uncoupled results.....	124
5.3.1. Comparison of the achieved temperatures on the plate. 10° configuration.....	125

List of figures

5.3.2. Comparison of the achieved temperatures on the plate. 20° configuration.	125
5.3.3. Comparison of the achieved temperatures on the plate. 30° configuration.	125
5.4.1.1. Heat flux distribution on the plate surface. Comparison between non-catalytic and full-catalytic ceramic surface.	128
5.4.1.2. Temperature distribution on the plate surface. Comparison between non-catalytic and full-catalytic ceramic surface.	129
5.4.1.3. Comparison of the achieved temperatures on the plate. 10° case. Test-003.....	130
5.4.1.4. Comparison of the achieved temperatures on the plate. 20° case. Test-006.....	130
5.4.1.5. Comparison of the achieved temperatures on the plate. 30° case. Test-008.....	131
5.4.2.1. Temperature distribution on the plate surface. Comparison with simulations with adiabatic inferior wall of the plate.	132
5.4.2.2. Temperature distribution on the plate surface. Comparison with simulations with adiabatic internal walls.	133
5.4.2.3. Temperature distribution on the plate surface. Comparison with simulations with adiabatic internal walls. Test-003, $\alpha=10^\circ$	134
5.4.2.4. Temperature distribution on the plate surface. Comparison with simulations with adiabatic internal walls. Test-006, $\alpha=20^\circ$	134
5.4.2.5. Temperature distribution on the plate surface. Comparison with simulations with adiabatic internal walls. Test-008, $\alpha=30^\circ$	135
C.1. Bi-dimensional model for the simulations of chapter 4.	142
C.2. Investigated flat-plate model. The measurement spots are also shown.	142

List of tables

3.1.1. Principal performance data of arc-heated facility L3K	24
3.2.3.1. Transmittance calibration for the IR-camera.....	34
3.2.4.1. Pyrometers' calibration.	35
3.2.5.1. Summary of the uncertainties.....	37
4.3.1. Reservoir and inflow conditions in L3K facility	45
4.3.2. Perfect gas properties	45
4.3.3. Convergence of the thermal quantities. Perfect gas modeling. $\alpha=10^\circ$	56
4.3.4. Convergence of the thermal quantities. Perfect gas modeling. $\alpha=20^\circ$	56
4.3.5. Convergence of the thermal quantities. Perfect gas modeling. $\alpha=30^\circ$	56
4.4.1. Inflow conditions for thermochemical non-equilibrium modeling in test chamber.	58
4.4.2. Heat flux and thermal gradient at the wall at $x=0.1$ m and $x=0.2$ m. 10° configuration with radiative equilibrium boundary condition	63
4.4.3. Mass fractions at the wall at $x=0.1$ m and $x=0.2$ m in comparison with the inflow values. 10° configuration with radiative equilibrium boundary condition.	65
4.4.4. Heat conductivity at the wall at $x=0.1$ m and $x=0.2$ m in comparison with the perfect gas modeling. 10° configuration with radiative equilibrium boundary condition.	65
4.4.5. Convergence of the thermal quantities. Thermochemical non-equilibrium. $\alpha=10^\circ$	66
4.4.6. Convergence of the thermal quantities. Thermochemical non-equilibrium. $\alpha=20^\circ$	66
4.4.7. Heat flux and thermal gradient at the wall at $x=0.1$ m and $x=0.2$ m. 10° configuration with fluid-structure interaction.....	68
4.4.8. Mass fractions at the wall at $x=0.1$ m and $x=0.2$ m in comparison with the inflow values. 10° configuration with fluid-structure interaction.....	69
4.4.9. Heat conductivity at the wall at $x=0.1$ m and $x=0.2$ m in comparison with the perfect gas modeling. 10° configuration with fluid-structure interaction.....	69
4.5.1. Inflow conditions and perfect gas properties for divergent flow.....	73
4.5.2. Convergence of the thermal quantities. Divergent flow. $\alpha=10^\circ$	77
4.5.3. Convergence of the thermal quantities. Divergent flow. $\alpha=20^\circ$	78
4.6.1. Inflow conditions and perfect gas properties. Nozzle flow simulated in thermochemical non-equilibrium.....	80
4.6.2. Convergence of the thermal quantities. Nozzle flow in thermochemical non-equilibrium. $\alpha=10^\circ$	85
4.6.3. Convergence of the thermal quantities. Nozzle flow in thermochemical non-equilibrium. $\alpha=20^\circ$	85
4.6.4. Convergence of the thermal quantities. Nozzle flow in thermochemical non-equilibrium. $\alpha=30^\circ$	86
4.7.1. Relative temperature difference with thermochemical modeling inside the chamber.....	88
4.7.2. Relative heat flux difference with thermochemical modeling inside the chamber.....	88
4.7.3. Relative temperature difference with divergent stream.....	88
4.7.4. Relative heat flux difference with divergent stream.....	88
4.7.5. Relative temperature difference with inflow quantities evaluated with nozzle in thermochemical non-equilibrium.	89
4.7.6. Relative heat flux difference with inflow quantities evaluated with nozzle in thermochemical non-equilibrium.	89
5.1.1. Positions of the thermocouples	94
5.1.2. Measurement positions of the pyrometers.....	94
5.1.3. Reservoir conditions and mass flow rate in the L3K facility.	97
5.1.4. Test cases.	98

List of tables

5.2.1. Convergence of the thermal quantities. Perfect gas modeling. $\alpha=10^\circ$	122
5.2.2. Convergence of the thermal quantities. Perfect gas modeling. $\alpha=20^\circ$	122
5.2.3. Convergence of the thermal quantities. Perfect gas modeling. $\alpha=30^\circ$	122
5.3.1. Comparison between measured and computed temperatures at the spots. $\alpha=10^\circ$	126
5.3.2. Comparison between measured and computed temperatures at the spots. $\alpha=20^\circ$	126
5.3.3. Comparison between measured and computed temperatures at the spots. $\alpha=30^\circ$	126
5.4.1.1. Convergence of the thermal quantities. Full-catalytic surface. $\alpha=10^\circ$	127
5.4.1.2. Comparison between measured and computed temperatures at the spots. Full-catalytic surface. $\alpha=10^\circ$	131
5.4.1.3. Comparison between measured and computed temperatures at the spots. Full-catalytic surface. $\alpha=20^\circ$	131
5.4.1.4. Comparison between measured and computed temperatures at the spots. Full-catalytic surface. $\alpha=30^\circ$	131
A.1. Principal material properties of C/C-SiC.....	139
A.2. Principal material properties of KAPYROK material	139
A.3. Principal material properties of used copper and stainless steel.....	139
B.1. Reaction rates. Gupta model.....	140

Abstract

The focus of this degree thesis is the validation of a numerical environment for the coupled analysis of thermal protection systems and hot structures in interaction with a high-enthalpy hypersonic flowfield. The simulation of the thermal fluid-structure interaction on a ceramic flat-plate model was conducted by means of the TAU code developed at DLR for the calculation of the flowfield and with the commercial software ANSYS for the thermal response of the structure. The comparison with experimental results was achieved with tests in the high-enthalpy facility L3K of DLR in Cologne, which enables reaching a steady-state of the temperature distribution on the surface thanks to its rather long running-time. Coupled simulations were proved to more effectively reproduce the distributions of the thermal quantities on the surface of the concerned ceramic plate. Different flow models for the high-temperature gas and for the stream conditions were numerically investigated in order to understand their impact on the surface quantities, which was demonstrated to be generally not significant. The computations were shown to properly capture the temperature trend on the objective surface, but the temperature values were underpredicted. Because of that, further numerical investigations were performed in order to understand the impact of a full-catalytic surface and of an absolutely imperfect thermal contact between the components. In this way, a partially catalytic behaviour of the ceramics at such temperature levels and a non-perfect thermal contact between some structure parts were pointed out.

Keywords: Fluid-structure interaction, coupled analysis, ceramic thermal protection system, high-enthalpy hypersonic flow, arc-heated facility, aerothermodynamics.

Sommario

La tesi è incentrata sulla validazione di un ambiente numerico che permetta di svolgere accuratamente la simulazione accoppiata di sistemi di protezione termica e hot structures sottoposti a un flusso ipersonico ad alto contenuto entalpico. Il calcolo dell'interazione termica tra fluido e struttura riguardante una lastra piana in materiale ceramico è stato portato a termine per la parte fluidodinamica grazie al software TAU, sviluppato al DLR, e per mezzo del software commerciale ANSYS per quanto riguarda la parte strutturale. Il confronto con risultati sperimentali è stato reso possibile da prove svolte nella galleria al plasma L3K presso la sede del DLR di Colonia. La galleria permette

il raggiungimento di condizioni stazionarie per la temperatura sulla superficie del modello, in quanto offre la possibilità di condurre test per tempi sufficientemente elevati. Le simulazioni che considerano l'accoppiamento si sono dimostrate più adatte per l'analisi dell'interazione fluido-struttura dal punto di vista termico rispetto a quelle non accoppiate. Si sono studiate differenti modellazioni per la corrente ipersonica, portando alla conclusione che l'effetto sulle variabili termiche presso la superficie del modello è poco significativo. Si è constatato che le simulazioni sono in grado di riprodurre efficacemente l'andamento della distribuzione di temperatura sulla superficie, ma i risultati delle computazioni si sono rivelati inferiori alle misure sperimentali. Per questo motivo ulteriori indagini numeriche sono state effettuate con lo scopo di individuare l'impatto di una completa cataliticità della superficie ceramica e di un eventuale contatto termico imperfetto tra le componenti del modello. Si è potuto così evidenziare il comportamento parzialmente catalitico della superficie impiegata a tali livelli di temperatura e l'influenza del contatto termico imperfetto tra alcune parti della struttura.

Parole chiave: interazione fluido-struttura, simulazioni accoppiate, sistema di protezione termica in ceramica, flusso ipersonico ad alto contenuto entalpico, galleria del vento al plasma, aerotermodinamica.

Chapter 1

Introduction

A space vehicle experiences along its trajectory from outer space to planetary surface extreme thermal loads, consequence of needing a deceleration from orbital velocities of several kilometers per second to prescribed landing velocities. The kinetic energy in the hypersonic free stream is dissipated and converted into gas thermal energy across the strong shock wave in front of the forebody region and through friction within the boundary layer [1]. A remarkable amount of the energy is transported towards the body surface. In accordance with the energy balance at the surface, this one is heated up. Thus, the temperature reaches very high values, both in the aftershock flowfield and on the vehicle's surface, causing the occurrence of so-called "high-temperature effects" on the fluid's atoms and molecules, such as dissociation, recombination, excitation of vibrational molecular degrees of freedom and ionization [2]. Moreover, chemical reactions in terms of oxidation and catalytic effects can take place on the body surface, increasing the acting aerothermal loads.

Therefore, the structure must be clearly designed not only in order to be capable of carrying the payload and the necessary fuel, but also to withstand these loads. The heat transfer rate is indeed the dimensioning criterion for some components of a spacecraft, such as the surface of the nose region and the wing leading edges [3].

A fundamental role is played by the exposure time: the system must satisfy different demands in accordance not only with the heating intensity, but also with its duration. The re-entry configuration and trajectory hence have a considerable influence [4].

Along the space transport history different kinds of solutions were adopted. In the case of the Apollo missions [5], which were subjected to extreme thermal loads but for a short exposure time, an ablative heat shield protected the core structure, while reusable fiber-reinforced ceramic materials were utilized for the tiles of the Thermal Protection System (TPS) of Space Shuttle [6] and BURAN [7].

A different philosophy lies behind the development and introduction of the so-called "hot structures". The key idea is no longer based on dividing the design of the structure in a "cold" bearing frame and in a TPS, but in coordinating the development of a unique, thermo-mechanical resistant concept able to achieve the requested mission, like e.g. the flaps of the X-38 aircraft [8]. This must be viewed in a more general design problem, where variables in terms of mass, costs, reliability, stability, smallest modification of the aerodynamics, systems integration, reusability, inspectability, montage, replaceability and

environmental compatibility play an essential role [9]. The optimization is achieved by means of the interplay of an appropriate choice of the new materials available nowadays, a well-studied return trajectory and a confident prediction of flowfield, thermo-mechanical loads and atmospheric conditions.

In the past, the physical nature of the problem usually was simplified by a series of assumptions in the common numerical and experimental tools, particularly with regard to structural discontinuities, surface quality and high-temperature effects, which obviously influence the interaction between fluid and structure. In absence of reliable experimental data, the approximation was taken into account by means of appropriate safety margins, in order to guarantee a conservative design, as obtained for instance in [10]. The consequence was an undesired mass – and implicitly costs – increase, or a mass subtraction from the payload capability.

In this context it is clear to understand the importance of well-validated tools, which are able to accurately reproduce and predict the intense fluid-structure interaction, which characterize the hot phase of the re-entry. Coupled simulations enable to properly capture the thermo-mechanical response of the structure, once the proof of the results of such tools is furnished by suited experiments in calibrated long-duration, high-enthalpy facilities, endowed of a sophisticated measurement technique.

Because of the complex phenomena which involve a hypersonic vehicle, ground-based tests still play a fundamental role for the simulation of such aerothermodynamic processes [11]. Therefore, the design of all re-entry machinery is performed through the integration of numerical tools and experimental facilities. Well-planned flight tests successively allow to get information otherwise not available on the ground and to verify the obtained predictions [1].

1.1 Work motivation and overview

Before numerical tools actually come into use for the prediction of the thermal load acting on the surface of a spacecraft, the validation of the procedure and the proof of the exactness of its results are necessary prerequisites. The present work takes its place in this perspective. The development of a suitable physical model capable of appropriately reproducing the fluid-structure interaction phenomena which involve the structure surface, the analysis of the coupled simulations results and their comparison with experiments are focal points of this thesis. For the collection of the experimental data a flat-plate model made of the ceramic material C/C-SiC is tested in the high-enthalpy facility L3K of DLR in Cologne.

After this introductory chapter, which discusses in outline the nature of the problem, chapter 2 describes the used numerical tools, with particular attention to the fluid-structure interaction in thermal terms. High-temperature effects, which can occur at such flow conditions, are considered in the physical model. The coupling procedure is also summarized in this chapter.

Chapter 3 contains the characterization of the tools used for the collection of the experimental data. The ground-based facility L3K which the tests are conducted in, the measurement technique and the applied instrumentation are treated in this chapter.

In chapter 4 preliminary numerical investigations are performed on an available geometry in order to tune the coupling procedure and to study the impact of different flow models on the thermal quantities at the coupling surface. The modeling of structure and fluid domain are carried out and different flow models are investigated (frozen flow, thermochemical modeling, divergent flow downstream of the facility nozzle). The fundamental influence of the fluid-structure interaction is demonstrated.

Chapter 5 deals with the actual comparison between computations and experiments and hence with the validation of the considered numerical modeling. The experimental campaign and the tested model are introduced and the measurements and their post-processing are presented. The numerical simulations on the flat-plate model are conducted and the computations are then compared with the measured data. Further numerical investigations are subsequently performed in order to better understand some aspects which have emerged during the comparison.

Chapter 6 summarizes the work, draws the conclusions and discusses potential future activities and developments.

1.2 Physical aspects along the re-entry

A spacecraft re-entering from its mission flies across various regions of the atmosphere, encountering different flow regimes. Figure 1.2.1 conceptually shows the different physical phases, which involve the body.

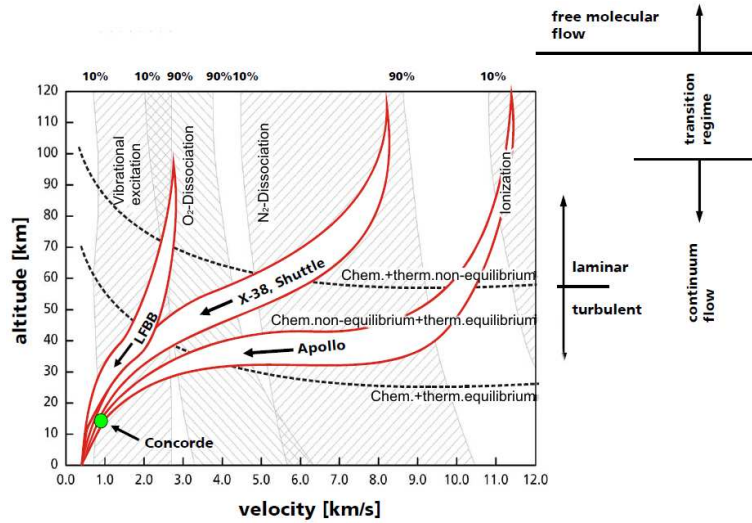


Figure 1.2.1. Flow regimes encompassed along a re-entry trajectory (from ref. [12]).

The Knudsen number, defined as the ratio between the molecular mean free-path length λ and a representative length scale L of the flowfield (usually in this case a characteristic dimension of the body):

$$Kn = \frac{\lambda}{L}, \quad (1.2.1)$$

regulates the influence of rarefied gas effects on flow conditions [3]. At very small Knudsen numbers (Kn of order of magnitude of 10^{-3} or below), i.e. for flight in low atmosphere layers where the air density is significant, continuum mechanics dominates the flow behaviour, while low-density effects must be taken into account at Knudsen numbers of order of magnitude about 1, where the gas is so rarefied that the molecular mean free-path length is comparable to the representative length scale: we speak in this case of free molecular flow. Transitional flow effects take place at intermediate Knudsen numbers and partially modify the continuum physics and the interaction between flow and structure.

In this context chemical processes and vibrational energy of the molecules must be considered as well. In order to understand their influence on the flowfield, some characteristic times can be introduced. The fluid-dynamic time τ_F is the characteristic time which a fluid element needs to cross the domain of interest, and usually is defined as the ratio between the characteristic length scale L and the free stream velocity V_∞ . The vibrational relaxation time τ_{vib} is the necessary time for a molecule's vibrational energy to reach equilibrium. The chemical

reaction time τ_{chem} is the characteristic time for chemical reactions. We speak of flow in local chemical or thermal equilibrium, respectively, if:

$$\tau_F \gg \tau_{\text{chem}} \quad (1.2.2)$$

or

$$\tau_F \gg \tau_{\text{vib}}, \quad (1.2.3)$$

which means that chemical reactions or vibrational energy have sufficient time to adjust while the fluid element moves through the flowfield. On the other hand, if:

$$\tau_F \ll \tau_{\text{chem}} \quad (1.2.4)$$

and

$$\tau_F \ll \tau_{\text{vib}}, \quad (1.2.5)$$

the fluid element moves out from the flow domain before any change in chemistry and vibrational energy state can occur, and we assume the flow as “frozen” (frozen flow). In all other cases, the flow is in chemical or thermal non-equilibrium [3].

1.2.1 Aerothermodynamic effects

As mentioned above, a variety of different physical processes involves a spacecraft along its re-entry trajectory. At hypersonic flow conditions, aerothermodynamic effects must be taken into account. On this point the so-called “aerothermodynamic collar” depicted in fig. 1.2.1.1 is particularly useful.

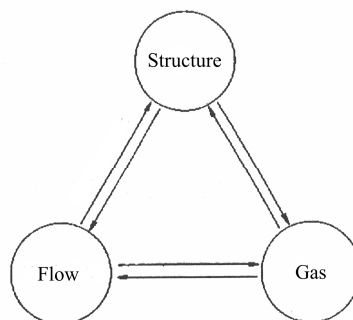


Figure 1.2.1.1. Aerothermodynamic collar (from ref. [13]).

The “classical” interaction between flow and structure is substantially influenced by thermal and chemical effects. These aspects are nicely treated by Koppenwallner [13], and are summarized here.

When flying through the atmosphere, a compression shock forms around the body, in front of the stagnation point region. Moreover, in the boundary layer the flow is slowed by shear stresses down to zero velocity at the wall. The very high flow kinetic energy is thus converted into thermal energy of the gas. The gas temperature can reach extreme high values, and the associated thermal loads acting on the structure imply the necessity of a special design for thermal protection.

Surface temperature distribution retroactively affects the flow, not only in terms of boundary condition and hence altering the energy balance at the surface, but also modifying the boundary layer development, i.e. its thickness and the thermal and velocity profile, as shown by Van Driest [14]. Thus, viscous interaction effects are in general rather relevant [3]: heat transfer increases, turbulent transition and flow separation are more likely to occur and the flight performances worsen [15].

The gas temperature can be high enough to excite vibrational molecular energy and cause the flow to become chemically reacting. Excitation of the vibrational degrees of freedom of the molecules begins for air at temperatures above 800 K, while dissociation of molecular oxygen takes place at temperatures between ca. 2000 K and ca. 4000 K, where only atomic oxygen is present. On the other hand, dissociation of molecular nitrogen proceeds between approx. 4000 K and approx. 9000 K, where only atomic nitrogen is present. Ionization of oxygen and nitrogen begins at temperatures above ca. 9000 K. However, it must be underlined that the gas behaviour also depends on the pressure. Reference [16] deals with these phenomena and figure 1.2.1.2, taken from it, helps to clarify the topic.

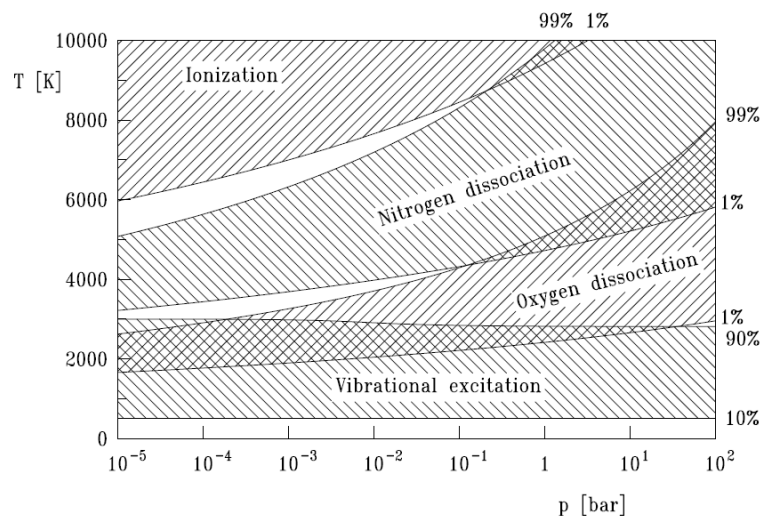


Figure 1.2.1.2. Vibrational and chemical phenomena for air in dependence on temperature and pressure (from ref. [16])

High-temperature effects considerably influence the gas nature and the fluid-structure interaction. The thermodynamic and transport properties can be deeply different from frozen flow, and diffusion mechanisms become very important. Heat transfer towards the structure can be remarkably enhanced, and energy transport due to species diffusion significantly contributes [3].

Moreover, rarefied gas conditions in association with compression shocks can alter the flowfield and worsen the flight performances [17]; in particular, dissociation remarkably affects the flow properties across a shock wave, since it is an endothermic reaction. The density behind the shock is hence higher than at frozen flow conditions, and the shock stand-off distance smaller [18].

At hypersonic flow condition, chemical interaction between gas and surface material must be considered as well. The works by Hald [9], Hilfer [19] and Laux [20] provide a satisfactory discussion of this subject. The utilized ceramic matrix composite materials, which are presented in the next section, are characterized by a matrix composed of silicon-carbide. Silicon and silicon-carbide can undergo oxidation in an environment containing oxygen. Passive oxidation forms a layer of SiO_2 over the body surface, while active oxidation forms gaseous SiO and CO and consequently causes a loss of material mass and a considerable increase of the temperature value at the surface. Both types of oxidation are associated with liberation of reaction enthalpy, and therefore with an increase of the heat flux loading the surface. The oxidation behaviour is basically regulated by the surface temperature and by the oxygen partial pressure.

Another important aspect of the surface properties must be taken into account. In a dissociated high-enthalpy flowfield, recombination reactions can take place at the material surface between SiC and SiO₂ and atomic oxygen and nitrogen. The recombination reactions liberate reaction enthalpy, which contributes to increase the heat flux loading the surface. The probability of occurrence of recombination is determined by the catalytic properties of the surface material: when all atoms reaching the surface undergo recombination, the material surface is defined full-catalytic, while a non-catalytic one is characterized by zero-occurrence of recombination reactions. According to [21], a helpful parameter for differentiating the catalytic behavior of a surface is the ratio between the recombining atoms \dot{N}_R and the total number of atoms which reach the surface \dot{N}_T :

$$\gamma = \frac{\dot{N}_R}{\dot{N}_T}. \quad (1.2.1.1)$$

For $\gamma=0$ the surface is considered non-catalytic, for $\gamma=1$ fully catalytic. Investigations by Stewart [22] showed a partially catalytic behavior for the C/C-SiC material, i.e. the catalytic properties of the surface depend on the temperature and on the oxidation state, as figure 1.2.1.3 clarifies.

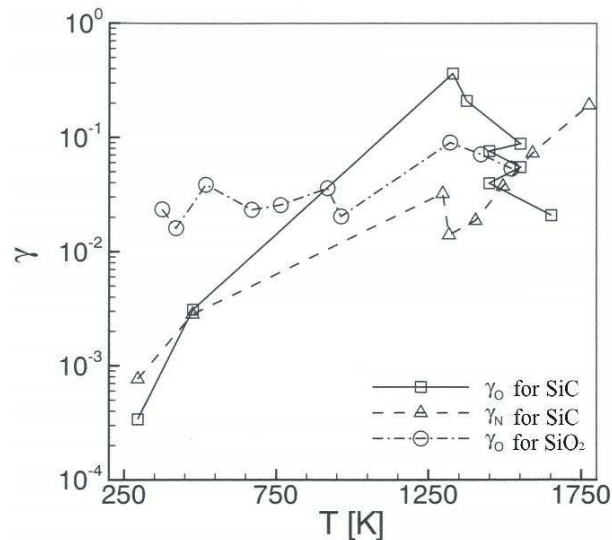


Figure 1.2.1.3. Partially catalytic behaviour of SiC and SiO₂ at high temperature in presence of atomic oxygen and nitrogen (from ref. [22]).

Also the surface quality plays a significant role. Depending on its characteristics, like roughness, presence of connection elements, etc., the boundary layer transition to turbulent conditions can be more likely to arise,

increasing the thermal load acting on the structure, see [14] and [23]. Turbulence causes indeed heat transfer rates much higher than for a laminar boundary layer, as expounded for example by Schneider [24].

Edges, gaps, steps and control surfaces are especially loaded zones. The flow involving these zones is particularly complex, comprehending significant three-dimensional effects, like crossflows, separations, re-attachments and vortices. The flow topology must be considered in its generality, because the inter-play of different effects can cause unexpected results [15]. For example, three-dimensionality can remarkably affect bi-dimensional predictions (see [25], [26] and [2]), while a different displacement of a gap or the formation of a step can vary the dimension of a separation bubble and thus increase the heat flux at the re-attachment line [27]. These problems can be especially crucial in association with control surfaces that can lose their efficiency, see [28] and [29].

In addition, thermal balance between convection, conduction and radiation must be taken into account. On opposite sides of gaps, steps and control surfaces, different view factors can cause a reduction of the radiative cooling (see [30] and [31]) or originate a radiative heating of otherwise not particularly loaded surfaces and thus intensify the local thermal load [32]. Convection in clefts [33] and heat conduction from hot to cold regions of the body, as shown in [30], [31] and [34], can affect the temperature and heat flux distribution as well.

1.3 Surface characteristics

As already mentioned, there is a crucial demand on the protection of a spacecraft against aerothermal loads.

A key-role is played by the radiative cooling of the body surface, in view of the high surface temperatures, as discussed in [35] and [36]. The choice of a material with high emissivity allows to obtain a high amount of radiative cooling and to effectively contrast the heat flux loading the structure.

Ablative surfaces were introduced in the Apollo Program [5]. The vehicle is covered with solid ablative material, which serves at first as heat sink; then increasing temperatures cause its endothermic transformation into gaseous state, reducing the thermal load on the vehicle [37].

There are several possibilities to perform active or passive cooling. This topic is well covered in [4]. Active cooling is effected for instance by blowing-out a cold gas over the surface in the boundary layer at laminar conditions: heat flux and surface temperature is thus contemporary reduced, as shown by [38] and [39]. An example of passive cooling is made possible by some zones of the vehicle surface which are set up as heat sinks, where either the surface can be

especially selected for an accentuated radiative cooling, or the local domain can be arranged for an elevated thermal capacitance, which can be exploited for a limited time, like in the case of the X-15 aircraft [40].

Because of their high-temperature withstand, rather high emissivity, low weight and good behaviour against corrosion, oxidation and erosion, ceramic matrix composite materials (CMC) are adequate for the employment in a reusable protection system against the high thermal loads, which space vehicles experience during the hot phase of their re-entry trajectory [41]. While in the past carbon fiber-reinforced CMC materials with carbon matrix were utilized, e.g. for Space Shuttle [6] and BURAN [7], carbon fiber-reinforced CMC materials with silicon-carbide matrix (C/C-SiC) are more and more diffused, see [42] and [43].

In the present work the C/C-SiC material developed by DLR Stuttgart [44] is employed for the numerical and experimental simulations. The temperature-dependent orthotropic material properties were broadly investigated within the collaborative research centre 259 (SFB 259 in German) of the University of Stuttgart, see [45] and [46]. Emissivity, specific heat capacity and heat conduction coefficients parallel and perpendicular to the fibers are the most interesting properties for the development of a thermal protection system. The present work relies on those data of the more recent investigations by Schäfer [30], because of the uncertainties inherently the manufacture process of the material [47]. The most important C/C-SiC properties are summarized in Appendix A.

1.4 Design tools

It must be emphasized that an exact knowledge of the thermal load acting on the body surface constitutes a fundamental requirement for the modern design of a spacecraft.

In the past, the design of a thermal protection system was principally based on analytical solutions of simple bodies, as spheres, cones, cylinders, wedges, etc. [48], which were compared with investigations in wind tunnel facilities on the corresponding surface domains and revised in accordance with corrections due to three-dimensional effects and laminar or turbulent flow conditions [25]. The extrapolated data were afterwards revised with real gas conditions data from flight experiments. The knowledge and reliability were, anyway, rather limited by the absence of a large data base, and the design approach principally relied on the minimization of risks due to complex flow topology and unknown phenomena [49]. Although the correlation procedure is still usual and technology improvements and experience allow more successful analysis (see for example [8] and [49]), the uncertainty in evaluating the thermal load with

regard to flight and wind tunnel experiments can unfortunately still reach even several percentage points.

As noted in [1], [8], [50], [51] and [52], the uncertainties in the flight experiment data principally lie on the influence of the manufactured surface quality, on the flow conditions, on the solar and inter-component cross radiation effects, on the catalytic properties of the surface, on the model complexity and on the uncertainties, usage limitations and integration of the instrumentation. These difficulties determine the complicacy to provide the model with the adequate measurement system [53] and hence to obtain quality data [1].

In the case of wind tunnel experiments the uncertainties mainly lie on the impossibility in reproducing all the relevant non-dimensional parameters [54], all the thermochemical effects [55] and the boundary layer transition [51], on the flow quality of the tunnel [56], on the perturbation impact of any kind of model support [1], on the presence of high levels of facility noise [24], on the complex measurement technique and on the often too short testing time available for getting the measurements [1].

In this context, long-time tools as the arc-heated facility L3K at DLR in Cologne, Germany, which the paragraph 3.1 is dedicated to, show noticeable advantages for the development and qualification of hot components of space vehicles, for the calibration of sensors for flight experiments, and for the validation of numerical tools [27].

Nowadays the improvement of computational tools has allowed to overcome many shortcomings of the other procedures, and to become the preferred method for the design of thermal protection in hypersonic flight [57]. Numerical simulations capable of including aerothermodynamic effects and comprehensively reproducing the involved fluid-structure interaction offer the chance of pursuing proper sensitivity analysis, which would not be possible – or only with extraordinary costs – using ground-based and flight tests, as pointed out by Hirschel [54] and Kolodziej [36].

The whole system is treated by decomposition and separated into interacting partitions (see [58] and [59]). The decomposition process is driven in this case by physical considerations, in view of the different nature of the two subsystems, fluid and structure. Each field is then separately discretized.

Initially, only the flowfield was simulated, usually with simple boundary conditions on the domain interface, like a fully catalytic, radiative equilibrium wall, as performed in [34] and [60]. The computed surface heat fluxes were then used as input for the structure thermal solver and hence to size the outer TPS layer. This methodology enables to obtain a conservative estimate of the system, which has, however, a critical impact on its mass and therefore on the vehicle performances. Neglecting the feedback of the structure, i.e. performing a one-way interaction [58], can lead to unphysical results. Reference [32] is an

interesting work which shows how disregarding the mutual interaction misrepresents the reality.

Two-ways coupled simulations show a better perspective. A tight coupling, where a complete system of equations which simultaneously considers both fields is solved [61], has been performed only for relatively easy problems, like in [62]. On the other hand, a loose coupling offers noteworthy advantages [58]: well-validated and highly-performing techniques and algorithms manage the separate discretization, adaptive mesh refinement and solution of each field; the use of non-matching models is easier; implementation, testing and validation can be conducted in a modular way; already available tools can be employed and are reusable for other projects. By reason of that and because of the different demands on modeling and computing the flow and the structure, a weak coupling is more adequate for simulating fluid-structure interaction phenomena at hypersonic conditions [63]. The necessary effort for the fluid solution and for the thermal analysis is indeed deeply different and appropriate domain decomposition techniques for non-overlapping domains can account for the diverse behaviors of the physical solutions [59]. The different codes are hence converted in subroutines alternatively called by a master code, and the coupling is performed just by information exchange at the interface between the two domains [61]. The solution procedure is then iterated until all field equations and coupling conditions are fulfilled [58]. The inter-field staggered iteration algorithm can thus be interpreted as the iterative solution of the complete system of equations characteristic of the monolithic approach [61]. However, the weak approach requires careful formulation and implementation to avoid degradation in stability and accuracy, and the iterations can be rather time-consuming [58]. If the circumstances favour a different discretization, non-matching grids are achieved at the interface. The conservation of mass, momentum and energy should be ensured, although this challenge is confined at this region, as discussed in [61] and [63].

The effort for steady problems, as the ones studied in the present work, is considerably lightened. A “classical” Dirichlet-Neumann iteration [59], gives very good results for an equilibrium problem, like the temperature distribution on a surface.

The validation of the numerical tools is fundamental for their subsequent employment in a design process. This is made possible by comparison with experimental data achieved at well-suited ground test facilities, as the mentioned L3K wind tunnel [64].

Apart from that, high-enthalpy wind tunnels still remain in themselves fundamental tools for the design and qualification of TPS components and hot structures, as long as the complexity of flow and aerotherodynamic fluid-structure interaction persists too challenging for numerical modeling, as [8] and [50] underline. Ground-based results can indeed be applied as bump factors for

the CFD database or directly for the creation of engineering models [65]. Although no wind tunnel is capable of complete duplication of the whole re-entry environment, diverse facilities can be employed to study different aspects. The restriction for the model scale due to the facility size implies, however, the possibility of investigating local effects on a properly chosen part [1].

On the other hand, computational simulations enable characterization of the flow quality in a ground-based facility, reproduction and analysis of phenomena not accessible to ground-tests, avoidance of limitations in model dimension as well as parametric studies, which would not be possible otherwise - or only with great expense [54].

As discussed so far, it is clear that the combined recourse to both, wind tunnels and numerical tools, is indispensable to cover satisfactory all aerothermodynamic processes experienced by a spacecraft and hence to properly achieve its design. Of course, it is important to remind that only the integration of these results with flight tests data allows an exhaustive understanding of the whole involved hypersonic environment.

Chapter 2

Numerical tools

This chapter describes the used numerical tools, with particular attention to the fluid-structure interaction in thermal terms. The coupling procedure is also outlined.

2.1 Thermal analysis

The simulation of the structure is accomplished thanks to the commercial finite element analysis code ANSYS [66]. Since in the present work the structural deformation is not taken into account, the investigations are limited to mere thermal analysis. The energy balance problem to be solved can be written in form of specific internal energy conservation [67]:

$$\rho c_p \dot{T} = Q_B - \nabla \cdot \mathbf{q}, \quad (2.1.1)$$

where ρ is the density, c_p the specific heat capacity at constant pressure, \dot{T} the temporal derivative of the temperature. The inner energy source term is depicted by Q_B , while \mathbf{q} is the heat fluxes vector, positive if subtracting energy from the body.

According to the procedure expounded by Zienkiewicz [68], equation (2.1.1) is weighted by virtual temperatures δT and integrated over the structure volume V_S with boundary S_S . By means of Gauss' theorem we obtain:

$$\int_{V_S} \delta T \rho c_p \dot{T} dV - \int_{V_S} \mathbf{q} \cdot \nabla (\delta T) dV = \int_{V_S} \delta T Q_B dV + \int_{S_S} \delta T q_N dS, \quad (2.1.2)$$

where q_N represents the heat flux normal to the surface contour (with local normal \mathbf{n} oriented outwards):

$$q_N = \mathbf{q} \cdot \mathbf{n}. \quad (2.1.3)$$

The heat flux vector \mathbf{q} can be related to the temperature gradients through Fourier's law:

$$\mathbf{q} = -\Lambda \nabla T, \quad (2.1.4)$$

where Λ is the heat conductivity tensor of the C/C-SiC material, which is:

$$\Lambda = \begin{bmatrix} \kappa_{//} & 0 & 0 \\ 0 & \kappa_{//} & 0 \\ 0 & 0 & \kappa_{\perp} \end{bmatrix} \quad (2.1.5)$$

for a reference system oriented as the material fibers [34]. As investigated in [46], the C/C-SiC material properties vary along with the temperature.

Once initial and boundary conditions are specified, the system of equations can be solved.

Following the finite element discretization, the temperature distribution and the temperature gradient inside the model are referred to the temperature of the nodes \mathbf{T} of the structure mesh by means of the shape functions \mathbf{N} and the gradients of the shape functions \mathbf{B} , hence:

$$T = \mathbf{N}\mathbf{T}, \quad (2.1.6)$$

$$\delta T = \mathbf{N}\delta\mathbf{T}, \quad (2.1.7)$$

$$\nabla(\delta T) = \mathbf{B}\delta\mathbf{T}, \quad (2.1.8)$$

$$\dot{T} = \mathbf{N}\dot{\mathbf{T}}. \quad (2.1.9)$$

Because of the arbitrariness of the virtual variations, accordingly to (2.1.6) – (2.1.9), the problem (2.1.2) can be expressed in the form:

$$\int_{V_s} \rho c_p \mathbf{N}^T \mathbf{N} dV \dot{\mathbf{T}} + \int_{V_s} \mathbf{B}^T \Lambda \mathbf{B} dV \mathbf{T} = \int_{V_s} Q_B \mathbf{N}^T dV - \int_{S_r} q_r \mathbf{N}^T dS + \int_{S_n} q_n \mathbf{N}^T dS, \quad (2.1.10)$$

where the boundary heat flux q_N has been split in a radiative contribution q_r and an external load q_n , in order to point out the possibility of specifying the kind of interaction at the interface. The radiative term has negative sign because it is supposed to decrease the inner energy of the structure (i.e. emitted heat flux), while q_n is supposed positive if increasing it. Also the structure contour is conceptually split in the different regions where the boundary terms act, but naturally S_r coincides partially or completely with S_n . Separating the external load q_n is particularly useful for a coupled analysis, since the Neumann boundary condition for the structure solver can be interpolated from the flow heat flux at the wall.

The radiative flux needs a detailed treatment. In case of “pure” radiation, namely between the surface and a sufficiently far background, the radiative heat

flux is assessed through the Stefan-Boltzmann constant σ , the surface total emissivity ε_T , the wall temperature and the background temperature T_u [69]:

$$q_r = q_{r,w} = \sigma \varepsilon_T (T_w^4 - T_u^4). \quad (2.1.11)$$

The surface is hence modeled at thermal equilibrium, in accordance with Kirchhoff's law [69]:

$$\frac{\alpha_T(T)}{\varepsilon_T(T)} = 1, \quad (2.1.12)$$

i.e. emissivity and absorptivity have the same value, but they can depend on surface temperature, introducing a further non-linearity.

On the other hand, if radiation between two surfaces occurs, the view factors between the surface elements must be taken into account. Reference [70] gives a satisfying analysis of the phenomenon and its finite element implementation.

Anyway, the investigated configurations (see chapters 4 and 5) are such that no radiative heat between the body surfaces takes place. The most general form for the system (2.1.10) is hence:

$$\underbrace{\int_{V_s} \rho c_P \mathbf{N}^T \mathbf{N} dV \dot{\mathbf{T}}}_{\mathbf{c}} + \underbrace{\int_{V_s} \mathbf{B}^T \mathbf{A} \mathbf{B} dV \mathbf{T}}_{\mathbf{k}} = \underbrace{\int_{V_s} Q_B \mathbf{N}^T dV}_{\mathbf{Q}_B} - \underbrace{\int_{S_r} q_{r,w} \mathbf{N}^T dS}_{\mathbf{Q}_r} + \underbrace{\int_{S_n} q_n \mathbf{N}^T dS}_{\mathbf{Q}_n}, \quad (2.1.13)$$

which may be summarized in the form:

$$\mathbf{c} \dot{\mathbf{T}} + \mathbf{k} \mathbf{T} = \mathbf{Q}_B - \mathbf{Q}_r + \mathbf{Q}_n. \quad (2.1.14)$$

The system (2.1.14) is non-linear because of the structure properties and the radiative terms and has to be iteratively solved. This is performed in ANSYS by means of the Newton-Raphson method [71].

2.2 Flow solver

The flow solver TAU developed at DLR [72] is based on the finite volume method for the solution of Navier-Stokes equations, which can be written in a general conservative form with respect to a Cartesian coordinates system, according to [1]:

$$\int_{V_F} \frac{\partial \mathbf{U}}{\partial t} dV + \int_{S_F} \mathbf{F} \cdot \mathbf{n} dS = \int_{V_F} \mathbf{Q} dV \quad (2.2.1)$$

where V_F is the control volume, S_F its boundary surface and \mathbf{n} the local normal vector to the surface, oriented outwards.

\mathbf{U} is the vector of the conservative flow quantities:

$$\mathbf{U} = \begin{Bmatrix} \rho_s \\ \rho \mathbf{u} \\ \rho E \end{Bmatrix}, \quad (2.2.2)$$

where ρ_s is the partial density of the species s , \mathbf{u} is the velocity vector with components u , v and w , and E is the total energy per unit mass. The density ρ of the gas mixture is obtained by species composition [73]:

$$\rho = \sum_s \rho_s. \quad (2.2.3)$$

\mathbf{Q} is the source vector, which depicts the mass sources ω_s as result of chemical reactions:

$$\mathbf{Q} = \begin{Bmatrix} \omega_s \\ \mathbf{0} \\ 0 \end{Bmatrix}. \quad (2.2.4)$$

\mathbf{F} is the flux tensor, which can be split in an inviscid and in a dissipative term, \mathbf{F}^{Eul} and \mathbf{F}^{ν} , respectively:

$$\mathbf{F} = \mathbf{F}^{\text{Eul}} + \mathbf{F}^{\nu}, \quad (2.2.5)$$

with:

$$\mathbf{F}^{\text{Eul}} = \begin{bmatrix} \rho_s \mathbf{u}^T \\ \rho \mathbf{u} \mathbf{u}^T \\ \rho E \mathbf{u}^T \end{bmatrix} + \begin{bmatrix} 0 \\ p \mathbf{I} \\ \rho \mathbf{u}^T \end{bmatrix}, \quad (2.2.6)$$

$$\mathbf{F}^v = \begin{bmatrix} D\nabla^T \rho_s \\ \mathbf{P} \\ \kappa\nabla^T T + D \sum_s h_s \nabla^T \rho_s + (\mathbf{P} \cdot \mathbf{u})^T \end{bmatrix}, \quad (2.2.7)$$

where p is the pressure, κ the heat conduction coefficient of the gas mixture, h_s the specific enthalpy per unit mass of the species s , T the temperature, \mathbf{P} the shear stress tensor and D the multi-component diffusion coefficient of the gas mixture. The gas considered in the present work is air. The gas particles are assumed to be at a temperature such that their radiative heat flux towards the surface can be neglected [3].

In accordance with [74], the total energy per unit mass is evaluated through:

$$E = \sum_s \frac{\rho_s}{\rho} e_s + \frac{1}{2} |\mathbf{u}|^2, \quad (2.2.8)$$

where e_s is the internal energy per unit mass of the species s , which contribute the internal energies associated with translation, rotation, vibration and electronic excitation to as well as the effective zero point energy:

$$e_s = e_s^{\text{tr}} + e_s^{\text{rot}} + e_s^{\text{vib}} + e_s^{\text{el}} + e_s^0. \quad (2.2.9)$$

The specific enthalpy per unit mass of the species s is consequently evaluated as:

$$h_s = e_s + \frac{\mathfrak{R}}{M_s} T, \quad (2.2.10)$$

where \mathfrak{R} is the universal gas constant and M_s is the molar mass of the species s . The shear stress tensor is defined in TAU under Stokes' hypothesis [75], i.e.:

$$\mathbf{P} = \mu \left[\nabla \mathbf{u}^T + (\nabla \mathbf{u}^T)^T \right] - \frac{2}{3} \mu (\nabla \cdot \mathbf{u}) \mathbf{I}, \quad (2.2.11)$$

where μ is the dynamic viscosity of the gas mixture.

The reaction models implemented in TAU for chemically reacting gas mixtures and the necessary reaction parameters refer to Park [76] and Gupta [77]. The mass source terms are thus obtained.

The dynamic viscosity of the species s is determined by means of a curve fit relation according to Blottner [78], while the viscosity of the gas mixture is evaluated through Wilke's composition rule [79].

Analogously to the calculation of the viscosity, the heat conduction coefficient of the species s is determined through a generalized Eucken's relation in accordance with Hirschfelder [80], under the assumption that the chemical composition is maintained in equilibrium with the local temperature, and the heat conduction coefficient of the gas mixture is provided by the mix rule, which can be referred to [73].

The multi-component diffusion coefficient D is approximated through the density, the viscosity and the Schmidt number Sc of the gas mixture, according to [81]:

$$D = \frac{\mu}{\rho Sc}, \quad (2.2.12)$$

where the mixture Schmidt number is assumed equal to 0.7.

Lastly, the pressure of the gas mixture is evaluated in conformity with Dalton's law [73]:

$$p = \sum_s \rho_s \frac{\mathfrak{R}}{M_s} T. \quad (2.2.13)$$

In case of frozen flow (see section 1.2), the gas behaviour can be approximated by the perfect gas model, and the procedure is undoubtedly simplified, since all terms depending on chemical reactions drop [74].

Sutherland's law is thus used for the determination of μ at not much elevated temperature – namely up to ca. 1000 K – above which the discrepancy with the reality is excessive and a modified Sutherland's law in accordance with [78] is implemented. The heat conduction coefficient is obtained directly from the dynamic viscosity, from the Prandtl number Pr and from the specific heat capacity at constant pressure c_p :

$$\kappa = \frac{c_p \mu}{Pr}, \quad (2.2.14)$$

assuming a suitable mixture Prandtl number of 0.72 [81].

Once initial and boundary conditions are specified [3], the system of equations can be solved by application of the finite volumes method [82].

The flow solver TAU is validated for unstructured, structured and hybrid meshes, and is capable of applying many central and upwind schemes [72], like Van Leer [83], AUSM (Advection Upstream Splitting Method) [84], AUSMDV [85] and EFM (Equilibrium Flux Method) [86]. TAU is capable of simulating subsonic, transonic and supersonic flows (see [87], [88] and [89], respectively), and laminar, transitional and turbulent flow condition can be treated (different turbulence models are implemented [72]). Moreover, chemical and thermal equilibrium and non-equilibrium can be considered.

Steady problems are solved through the introduction of a pseudo-time and then looking for the steady-state solution of the corresponding time-dependent problem [72].

The integration in time is performed by means of an explicit Runge-Kutta scheme according to Jameson [90]. Many acceleration techniques for the reduction of the computational time are included, such as local time-stepping, multi-grid algorithms and residual smoothing techniques [72].

TAU is basically composed of three main modules: the preprocessor, the flow solver and the adaptation module. The former generates the geometrical properties of the grids; the second one solves the system of equations, and its results are used by the latter module to refine the grid subdomains where the quality of the solution is still not sufficient. The refinement process is particularly helpful for shock waves and boundary layers, so that the flow quantities in wall and shock proximity can be accurately resolved [26].

2.3 Coupling methodology

As already mentioned in section 1.4, the weak coupling algorithm deals with a classical Dirichlet-Neumann procedure. The system (2.2.1) is solved in the fluid domain V_F for the flow quantities, with Dirichlet boundary conditions at the interface $\Gamma = V_F \cap V_S$ interpolated from the structure solution at the previous step. The structure problem (2.1.14) is then solved in V_S for the temperature, with Neumann boundary conditions on Γ . The inter-field iteration is thus performed sequentially [58]. According to [59], the algorithm can conceptually be summarized as follows:

0. a start solution is achieved in the fluid field, with isothermal or radiative adiabatic wall boundary condition for the flow solver on the interface Γ . $k=0$;

1. the heat flux $q_n^F(k)$ at the wall is computed from the flow solution and is provided to the structure solver as Neumann boundary condition, namely:

$$q_n^F(k) = \left(\kappa^F \frac{\partial T^F(k)}{\partial n} \right)_w + \left(D \sum_s h_s^F \nabla^T \rho_s^F \right)_w = q_n^S(k) \text{ on } \Gamma, \quad (2.3.1)$$

where energy transport due to chemically reacting flow is included along with thermal heat conduction;

2. $k=k+1$. The structural problem is solved. The temperature at the interface is computed from the structure solution and is supplied to the flow solver as Dirichlet boundary condition, in case relaxed in order to improve the convergence behavior or to stabilize the solution at the initial steps:

$$T_w^F(k) = \Phi T_w^S(k) + (1 - \Phi) T_w^F(k-1) \text{ on } \Gamma, \quad (2.3.2)$$

with $0.5 \leq \Phi < 1.0$;

3. solution of the flow field. Back to point 1. until a convergence criterion is satisfied.

The coupling quantities are linearly interpolated by means of the non-conservative algorithm developed in [31]. As shown in this work for a configuration similar to the present ones, the numerical influence of the coupling due to non-conservativeness and grid fineness is negligible as long as the characteristic grid dimensions of flow and structure discretizations at the coupling interface are not too different. The uncertainty amounts indeed to less than 2% for both, temperature and thermal flux.

Moreover, it is pointed out that the interface temperature is the appropriate convergence criterion to be chosen, since the convergence of the temperature is monotone, whereas the heat flux shows local peaks due to numerical effects. In fact, the flowfield should be solved very accurately for a proper heat flux evaluation, in view of the dependence of the heat flux on the temperature gradient, which is more sensitive to local errors than the temperature itself. The convergence of the interface temperature is hence selected as stop criterion for the inter-field iterations.

Chapter 3

Experimental set-up

The present chapter contains the characterization of the employed tools for the collection of the experimental data. The ground-based facility L3K which the tests are conducted in, the measurement technique and the used instrumentation are described here.

3.1 Arc-heated facility L3K

The experimental investigations, which play an important role in the current work, take place at the arc-heated facility L3K at DLR in Cologne, Germany. Arc-heated wind tunnels are able to provide a continuous, high-enthalpy flowfield for a long testing time (up to 30 minutes for L3K), and are suitable for the realistic reproduction and analysis of fluid-structure interaction phenomena at hypersonic flow conditions and therefore for the assessment of adequate thermal design criteria as well as for the validation of numerical tools [27].

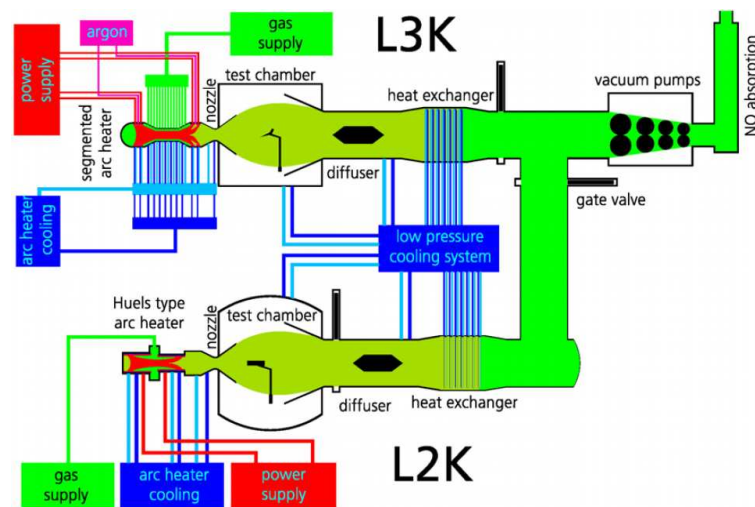


Figure 3.1.1. Schematic description of the arc-heated facilities L2K and L3K at DLR.

As shown in fig. 3.1.1, the arc-heaters supply two test legs, L2K and L3K. The considered L3K facility is supplied by a segmented arc-heater with a power level of 6 MW, which allows reaching reservoir specific enthalpies up to 25 MJ/kg. The facility can operate with gas mass flow rates between 0.03 and 0.3 kg/s and Pitot pressures between 2000 and 125000 Pa. Mach numbers between 3 and 10 are achieved by means of conical nozzles with a half angle of 12°. The nozzle throat diameter can be set to 14 or 29 mm and the exit diameter to 50,

100, 200, or 300 mm, thanks to the modular nozzle design. Unfortunately, the maximal attainable Reynolds number corresponds to an order of magnitude of 10^5 , which means that flight Reynolds numbers typical of the low-altitude re-entry phase of a spacecraft cannot be duplicated. Anyway, as already mentioned, the wind tunnel is one of the most appropriate tools for the design and validation of TPS components and hot structures. The principal performance data of the L3K facility are summarized in table 3.1.1.

The test chamber has square section normal to the free flow characterized by sides of 1.5 m and is 2 m long. Four main windows and ten further small windows enable optical access to the chamber. Flat-plate models with main dimensions of 330 mm (length)×270 mm (width)×55 mm (height) and stagnation point models with a diameter up to 150 mm can be tested in a nearly homogeneous hypersonic flowfield. Two model positioning systems are available: one offers the possibility of moving the model quickly into or from the flowfield and to set angular position around the tunnel axis, while the other one enables to adjust its angle of attack.

Table 3.1.1. Principal performance data of arc-heated facility L3K (from ref. [11]).

Mach number	3 - 10
Max. Reynolds number [m^{-1}]	10^5
Pitot pressure [hPa]	20 - 1250
Total enthalpy [MJ/kg]	6 - 25
Max. test duration [s]	1800

A vacuum pumping system allows obtaining the low pressure necessary for ignition of the arc-heater. Downstream of the test chamber, the L3K facility is equipped with a diffuser with a central body and with a heat exchanger. In this way the gas is decelerated and its temperature reduced below the upper operating limit for the vacuum pumps, which is 370 K. Depending on the acting thermal loads and electrical resistivity of the facility components, two different cooling systems are installed, one at high pressure with demineralized water and the other one at low pressure with raw water. Tests can be run with air and nitrogen. The facility is equipped also with a cleaning system, which enables absorption of toxic nitrogen oxide from exhaust gases. An automatic control system guarantees safety in a test environment characterized by high voltage, high current and strong electromagnetic fields, since it acquires and monitors all operational data.

Furthermore, experimental data are recorded by an acquisition system provided with 128 analogue input, 96 digital input/output channels and 32 filter and amplifier units, which makes possible sampling rates up to 100 kHz. An exhaustive discussion of the L3K facility and its supply systems is furnished by Gülhan in [91] and [11].

Because of the extreme flow conditions in a high-enthalpy wind tunnel, a satisfying flow characterization which covers all aerothermodynamic phenomena occurring in the tests is possible only with the help of numerical tools, although the reservoir conditions can be rather accurately determined from measurements. Numerical investigations for the assessment of the flow homogeneity in the facility were performed and compared with experimental data, see [27] and [92]. Only small differences arise in radial direction between flow axis and free stream boundary with bigger nozzle exit diameters, while the influence of the expansion wave generated at the nozzle exit is considerable at higher radii when using smaller nozzle exit sections. The agreement with experiments is generally good.

The recent work by Mack [31] is rather significant, since the whole tunnel – comprehending even the nozzle and the diffuser as well as the test chamber – were simulated, considering chemical non-equilibrium and thermodynamic equilibrium. Moreover, in this work different chemical and thermodynamic models were taken into account, variations with respect to reference reservoir conditions were examined and the influence of tunnel geometry and surface roughness were investigated. One of the main results of these simulations is that the flow “freezes” upstream of the nozzle exit in view of the very low density and that the thermochemical modeling close to the tested body has a negligible influence on the surface quantities. In fact, all thermochemical phenomena occur in the facility upstream of the test chamber, in view of the heating up of the gas through the arc-heater up to reservoir conditions and of the subsequent thermochemical relaxation in the nozzle. The mass fractions of the gas mixture components freeze in practice a bit downstream of the throat and they remain nearly unaltered down to the chamber. Further numerical investigations accounting also for thermodynamic non-equilibrium confirm this occurrence. These simulations are discussed in chapter 4, but some of their results are plotted in figures 3.1.2 and 3.1.3 in order to point out the evolution of the thermochemistry in the facility.

A perfect gas model can be hence satisfying for the flowfield around the model, whereas thermochemical modeling must be considered for the nozzle.

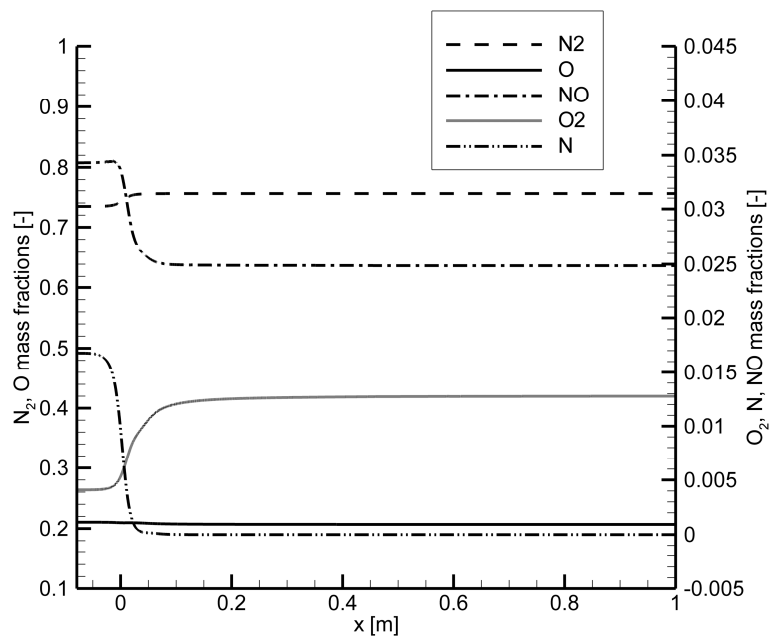
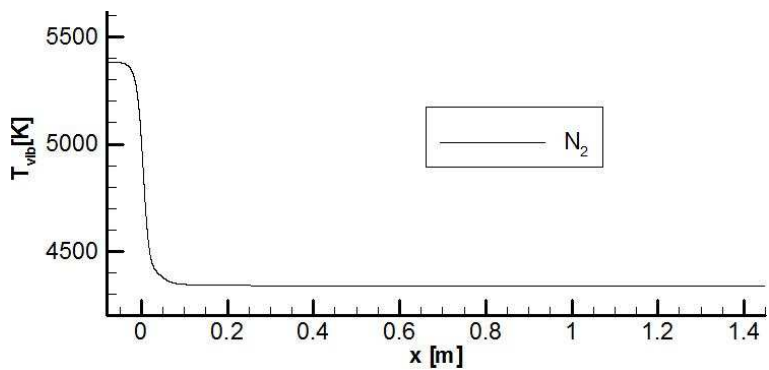
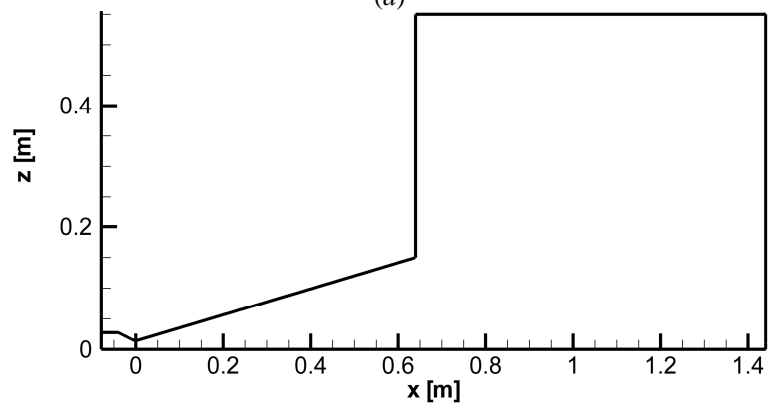


Figure 3.1.2. Mass fractions distribution along the facility's centerline.



(a)



(b)

Figure 3.1.3. N_2 vibrational temperature along the facility's centerline (a) and axisymmetric facility contour (b).

Moreover, at such tested Reynolds numbers the flow remains laminar throughout the whole flowfield in the test chamber [93]. The effect of the surface roughness may be indeed only to induce the boundary layer transition to turbulence [75]. According to [45], the surface roughness of the considered C/C-SiC material has an order of magnitude of the fiber diameter ($\sim 10^{-4}$ m), and the numerical investigations by Mack [31] allow sustaining that it has no influence on the flowfield, since the laminar boundary layer is much thicker.

3.2 Temperature measurement system

The temperature measurement system consists of thermocouples and non-intrusive optical devices, exactly pyrometers and an infrared camera. Two important aspects affect the reliability of thermocouple measurements in high-enthalpy flows and hence margin their employment on the model surface: firstly, the high-temperature stability of the adhesives, which fix the thermocouples on the surfaces; secondly, chemical reactions between thermocouple material and gaseous species released by the surface, which contaminate the flowfield.

Because of these reasons non-intrusive optical devices are adopted for the temperature measurements on the surface.

3.2.1 Thermocouples

A thermocouple offers a punctual temperature measurement and must be in contact with the investigated body. As sketched in fig. 3.2.1.1, a thermocouple is composed of two wires (the thermoelements) made of different metals, which are joined at the so called junction end, where the temperature must be measured. The wires are embedded in an isolation material and connected at the other end (the tail end), where the temperature is known. When the junction end is heated up, a voltage difference occurs at the tail end. An appropriate device can measure this thermoelectric voltage, which is a function of the temperature difference and of the materials constituting the wires. A sketch of a thermocouple is displayed in figure 3.2.1.1.



Figure 3.2.1.1. Sketch of a thermocouple.

In the reality, the thermoelectric voltage cannot be measured directly, since the link of the thermocouple with the measuring instrument implies the presence of a further voltage across the connection. Because of that, a reference junction or a compensation device is necessary. More details and a list of thermocouple types refer to [94].

The thermocouples chosen for the test campaign at L3K are of type K – class II (wire composition NiCr-Ni, maximal usage temperature 1372 °C, wire diameter 0.5 mm). The decision is basically dictated by their good long-time stability and by the recommended usage temperatures, which are suitable for the conducted experiments in view of a maximal recommended temperature of 1100 °C.

3.2.2 Optical temperature measurement technique

The optical temperature measurement technique (pyrometry) is non-intrusive, because it is based on the measure of the radiance emitted by a surface.

The layout for a pyrometric device is sketched in figure 3.2.2.1.

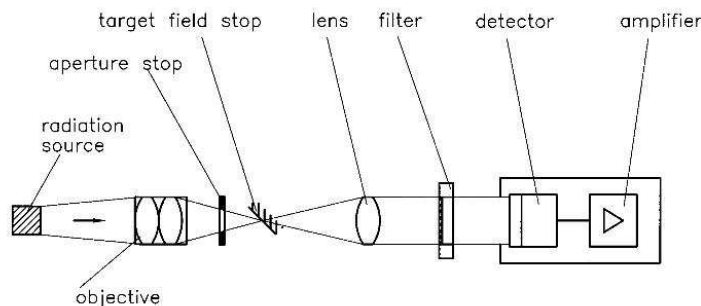


Figure 3.2.2.1. Sketch of an optical device for temperature measurements (from ref. [95]).

The objective captures the emitted radiance and a lens projects it to a radiance detector, which transforms the optical signal into an electrical signal, proportional to the emitted radiance. The aperture stop defines the amount of light coming towards the device and avoids getting-in irradiation from foreign objects. The field stop determines the field of view of the camera, since it prevents entrance of highly oblique rays.

Accordingly to the procedure described by Gülhan [95], the temperature of a body, whose radiation properties depend on the wavelength, can be evaluated thanks to a reference black body, which is characterized by unitary absorptivity and emissivity. The spectral specific radiance for unit solid angle $M_{\lambda,b}(\lambda, T)$ of a black body (index b), can be expressed through Planck's law [69]:

$$M_{\lambda,b}(\lambda,T) = \frac{2c_0^2 h \lambda^{-5}}{e^{\frac{hc_0}{k\lambda T_b}} - 1}, \quad (3.2.2.1)$$

where λ is the wavelength, c_0 the light speed in vacuum, h the Planck's constant and k the Boltzmann's constant. In accordance with Kirchhoff's law (2.1.12), the spectral specific radiance of the investigated body surface $M_\lambda(\lambda,T)$ can be expressed through its spectral emissivity $\varepsilon_\lambda(\lambda,T)$:

$$\varepsilon_\lambda(\lambda,T) = \frac{M_\lambda(\lambda,T)}{M_{\lambda,b}(\lambda,T)}, \quad (3.2.2.2)$$

in the following way:

$$M_\lambda(\lambda,T) = \varepsilon_\lambda(\lambda,T) \frac{2c_0^2 h \lambda^{-5}}{e^{\frac{hc_0}{k\lambda T}} - 1}. \quad (3.2.2.3)$$

If $\varepsilon_\lambda(\lambda,T)$ and T_b are known and considering (3.2.2.2) and (3.2.2.3), the temperature of the investigated body surface can be evaluated as follows:

$$\frac{e^{\frac{hc_0}{k\lambda T}} - 1}{e^{\frac{hc_0}{k\lambda T_b}} - 1} = \varepsilon_\lambda(\lambda,T). \quad (3.2.2.4)$$

Once the measured signal is calibrated by means of black body simulators (i.e. bodies, which behave in practice as a black body for some portion of the electromagnetic spectrum), the temperature value is thus available, see [32]. In fact:

$$T = \frac{A}{\ln\left(\frac{\varepsilon_\lambda(\lambda,T)\tau_\lambda(\lambda,T)M_\lambda(\lambda,T)}{B} + 1\right)}, \quad (3.2.2.5)$$

where A and B are calibration constants, given by the instrument producer, and $\tau_\lambda(\lambda,T)$ is the transmittance of the employed optical setup, which is achieved within the calibration preceding the actual tests (see section 3.2.3). The irradiation reaching the detector decreases in accordance with the transmittance of the atmosphere inside and outside the test chamber as well as the transmittance of the optical access to the model. Anyway, the transmittance of

the inner atmosphere can be in effect assumed as unitary, unless water vapor is present in the chamber [95], while the problem with the outer atmosphere can be avoided by simply positioning the device in contact with the glass (the transmittance inside the instrument can be reasonably considered unitary, too). On the other hand, the optical accesses are not transparent and this behaviour is worse at higher wavelengths, i.e. at $\lambda > 2\text{-}3\ \mu\text{m}$ [96]. The transmittance can be improved thanks to one or more anti-reflection layers, but it is not possible to obtain the unitary value. The main windows the L3K facility is equipped with are made of germanium [97] and have an anti-reflection coating which guarantees high transmittance in the range $\lambda = 8\text{-}12\ \mu\text{m}$ [98], while the small windows used for pyrometer access are made of fused quartz [96].

The spectral behaviour of radiance detectors, optical filters and lenses and the transmittance of the measurement path clearly influence the spectral response of an optical device. Relative considerations lead to the choice of the instrumentation, in particular in terms of appropriate spectral range and positioning [95]. It must be added that the knowledge of the spectral emissivity ε_λ of the surface of a C/C-SiC model is only approximate, because of the complexity of the manufacturing process involving the ceramics. Tests on the C/C-SiC material [99] present an uncertainty for the surface spectral emissivity that lies on $\Delta\varepsilon_\lambda = \pm 5\%$ for wavelengths above $1.3\ \mu\text{m}$ and up to $\Delta\varepsilon_\lambda = \pm 10\%$ for shorter wavelengths. Moreover, the uncertainty in set-up transmittance and surface emissivity may further be increased when the oxidation processes mentioned in section 1.2.1 occur, because of the variation of the surface properties and the formation of surrounding gases.

From the reasons above, and considering that the surface temperature of the model evolves from chamber temperature up to very high values, it is not possible to use the same type of instrument to obtain accurate values for the whole temperature range. Therefore several optical devices are contemporarily employed, so that different measurement ranges can be covered. Moreover, they must satisfy thermal resolution requirements. The local spectral emissivity of the material is thus used together with the expected temperature level in the specification of the appropriate spectral range of the optical device, accordingly to (3.2.2.3). Once the spectral range is defined, the more suitable device is chosen. At the operative conditions achieved in L3K, optical devices characterized by a spectral range in the near infrared region are the most appropriate [95].

3.2.2.1 Pyrometers

Pyrometers furnish punctual temperature measurements and are basically subdivided in two types: spectral pyrometers and two-colour pyrometers. The working principle of the former ones ensues what was previously explained;

therefore emissivity is necessary to determine the temperature, according to (3.2.2.5). Unfortunately, it is difficult to get a precise emissivity value in most of the cases, in particular for ceramic surfaces subjected to high-enthalpy flows, as mentioned in the preceding section.

The operational range of the spectral pyrometers available at L3K is about $1 \mu\text{m}$. In this range, an inaccurate value of the emissivity determines a certain error in the temperature, as shown in figure 3.2.2.1.1 for an uncertainty $\Delta\varepsilon_\lambda = \pm 0.05$ about a nominal emissivity $\varepsilon = 0.85$, according to Planck's law [69].

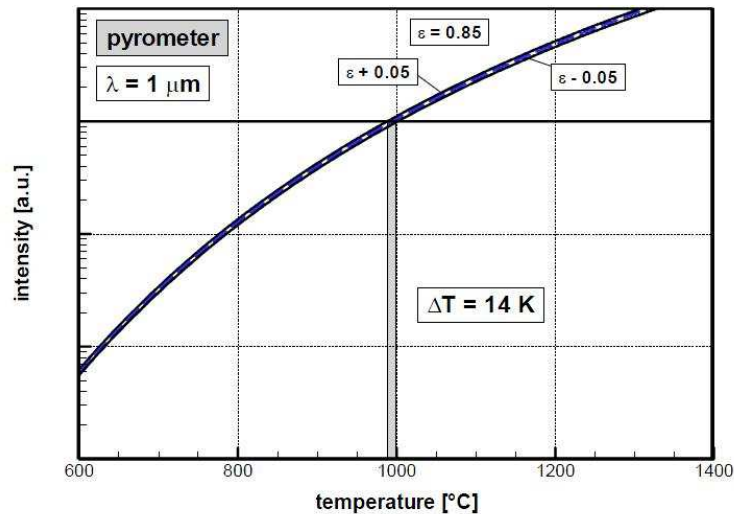


Figure 3.2.2.1.1. Temperature uncertainty at $\lambda=1 \mu\text{m}$ (from ref. [32]).

The induced uncertainty at a temperature level of $1000 \text{ }^\circ\text{C}$ is thus $\pm 7 \text{ }^\circ\text{C}$. Depending on the circumstances, this error may be tolerable or not. An alternative is presented by the usage of two-colour pyrometers, which temperature measurement is considered independent of surface emissivity and optical set-up transmittance. This is possible thanks to the measurements of two spectral specific radiances $M_{\lambda,1}(\lambda_1, T)$ and $M_{\lambda,2}(\lambda_2, T)$ at close wavelengths λ_1 and λ_2 , at which the emissivity can reasonably be assumed as a constant, i.e. the behaviour of the material surface can be approximated in the range λ_1 - λ_2 as a perfect grey body. The emissivity influence on the temperature estimation is hence eliminated through the relation between the two $M_{\lambda,1}(\lambda_1, T)$ and $M_{\lambda,2}(\lambda_2, T)$. Changeable transmittance characteristics in the measurement path are eliminated in the same way, see [100].

Local material emissivity can thus be estimated by the comparison of two-colour and spectral pyrometers measurements (see section 5.1.3).

The applied spectral pyrometers operate in a range between 0.83 and $1.03 \mu\text{m}$. There are five pyrometers available for optical measurements at the L3K

facility: two two-colour pyrometers, which are characterized by a temperature range between 900 and 3000 °C [101] and between 800 and 2000 °C [102], respectively, and three spectral pyrometers, which are characterized by a temperature range between 900 and 3000 °C [103], between 900 and 2000 °C [104] and between 550 and 3000 °C [105], respectively. The latter (“Minolta” pyrometer) undergoes rather frequent calibration [106] and can be used as reference for the other pyrometers, which measurements are corrected thanks to a calibration procedure described in section 3.2.4.

It is important to underline that their punctual measurement actually takes place on an approximately circular area with a diameter of ca. 6 mm.

3.2.2.2 Infrared cameras

Infrared cameras are very useful devices, since they provide bi-dimensional surface temperature distributions. Anyway, their records need two further post-processing steps in comparison with pyrometers.

The first step refers to the transformation from the pixel-oriented image coordinates (x_p, y_p) to the more useful model-fixed coordinate system (x, y, z) , since the employed camera can have in general an oblique view on the model. Having data in the model-fixed coordinate system helps the comparison with the numerical simulation results, which are related to this coordinate system. According to [107], the transformation needs six parameters, which describe a general transformation between two Cartesian coordinate systems, and at least a seventh parameter, which takes into account the optical projection of the camera. The transformation is typically accomplished by means of the coordinates of some positions on the body surface, which are always clearly distinguishable and hence known in both coordinate systems [32]. Once these parameters are available, each camera pixel can be associated to a corresponding area on the investigated surface, which dimension depends on the camera resolution.

The second step is due to the operational range of the infrared cameras, which is about 10 μm in the case of the L3K facility instrumentation. In this range, an inaccurate value of the emissivity determines an inadmissible error in the temperature, as depicted in figure 3.2.2.2.1 again for an uncertainty $\Delta\varepsilon_\lambda = \pm 0.05$ about a nominal emissivity $\varepsilon = 0.85$, according to Planck’s law [69].

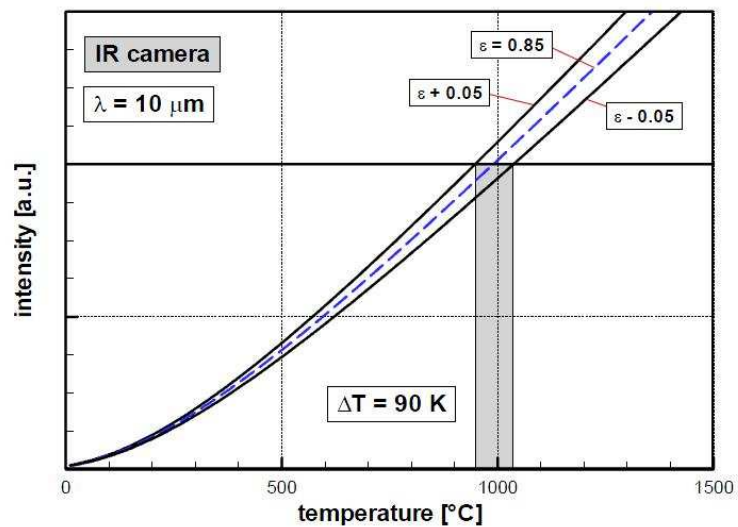


Figure 3.2.2.2.1. Temperature uncertainty at $\lambda=10\ \mu\text{m}$ (from ref. [32]).

The induced uncertainty at a temperature level of $1000\ \text{°C}$ is in this case $\pm 45\ \text{°C}$. As explained so far, surface emissivity is not accurately known for many cases, especially for ceramic materials at very high temperatures. Because of that, infrared camera records are corrected by means of pyrometers measurements (see section 5.1.3).

An extensive usage of infrared cameras would be expensive, because their hardware and software are quite complicated. It would be unnecessary as well. Therefore, only one infrared camera is employed in the experimental campaign. The chosen one, AGEMA THERMOVISION 570 S, offers many advantages, since it is characterized by a Focal Plain Array detector (FPA), consisting of a big amount of small perceptive elements, which contemporarily detect the surface radiance distribution [108]. Its resolution is 320×240 pixels, which corresponds to a surface resolution of ca. $1\ \text{mm}^2$, and can acquire images up to 50 Hz.

The camera is optimized in a spectral range between 7.5 and $13\ \mu\text{m}$ by means of a built-in atmospheric filter. Moreover, calibration is carried out for three temperature ranges, i.e. between -20 and $120\ \text{°C}$, between 80 and $500\ \text{°C}$ and between 350 and $2000\ \text{°C}$. Thus the camera can confidently cover a temperature range between -20 and $2000\ \text{°C}$.

3.2.3 Window transmittance calibration

The effects of a non-transparent window on the transmittance of the measurement path can be taken into account through a rather straightforward procedure. DLR has a black body simulator which works well for the necessary temperature range [109]. It is realized through a very small aperture compared to

the frontal area. The radiation enters the cavity and experiences many reflections before re-emergence. Once the inner wall temperature reaches uniformity, the black body behaviour is thus approximated, since the radiation is almost completely absorbed and the emission from the hole as well as the irradiation of interior surfaces are diffuse.

This simulator is used for the calibration of the set-up in question. The optical device is oriented towards the aperture and centered with respect to it. The distance between instrument and black body is ca. 1 m, which typically is the distance between optical access and tested model at the L3K facility. Figure 3.2.3.1 qualitatively represents the set-up of the calibration.

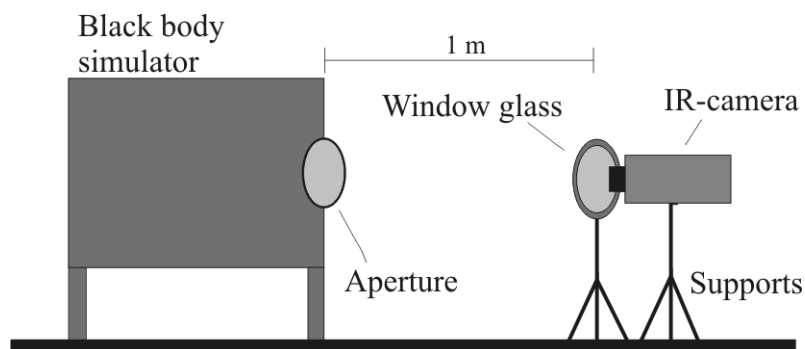


Figure 3.2.3.1. Sketch of the set-up for window transmittance calibration.

The data start to be acquired, and successively the investigated glass is positioned in front of the objective, in order to reproduce the test situation. The temperature difference between the two cases is then processed by means of equation (3.2.2.4), being the emissivity of a black body equal to 1 and knowing the temperature that should be measured, which is indicated by the black body simulator together with the reference pyrometer and is hence reliable. The procedure is repeated for the concerned temperature range, interpolating linearly between calibration spots. Since the employed spectral pyrometers work at wavelengths $\lambda=0.83\text{-}1.03\ \mu\text{m}$, it is possible to neglect the window transmittance effect on their records (see section 3.2.2), and the calibration is performed only for the IR-camera. Table 3.2.3.1 summarizes the calibration data for the more interesting temperature range.

Table 3.2.3.1. Transmittance calibration for the IR-camera.

τ	Main window	Small window
$T=800^{\circ}\text{C}$	0.83	0.75
$T=1000^{\circ}\text{C}$	0.84	0.77
$T=1200^{\circ}\text{C}$	0.83	0.76

It must be underlined that this transmittance value is a quantity estimated over all wavelengths of the IR-camera range, according to its instrumentation [108]. The transmittance is thus established and registered within the device software. Further variations are then treated together with the emissivity uncertainties through the pyrometers measurements.

The small window calibration data are not used in the following, since the IR-camera is placed at one of the main windows.

3.2.4 Pyrometers' calibration

The unique available pyrometer which offers rather confident measurements in the absence of emissivity and transmittance uncertainties is the Minolta pyrometer [105], in virtue of its frequent calibration. Moreover, the other pyrometers are characterized by a temperature measurement range which starts at 800 or 900°C, and their performances are expected to be not optimized in the inferior band of this range. Because of these reasons a correction is necessary. It is obtained thanks to an ulterior calibration procedure. The set-up is similar to section 3.2.3, i.e. the pyrometer under discussion is oriented perpendicular to the centre of the black body aperture and distanced by about 1 m from it. The black body source is heated up to different temperature levels, which are registered together with the Minolta pyrometer, and the investigated instrument measures a certain value. The procedure is performed for the estimated surface temperature range and repeated for all used pyrometers. Table 3.2.4.1 summarizes the results of this calibration.

Table 3.2.4.1. Pyrometers' calibration. Temperatures given in °C.

Black body	2C-3000	S-3000	2C-2000	S-2000	Minolta
1200	1158	1166	1186	1209	1199
1100	1063	1068	1087	1106	1097
1000	970	975	987	1004	997
910	-	-	900	905	908

The abbreviation “2C” refers to two-colour pyrometers, “S” to spectral, “3000” and “2000” to the maximal measurable temperature. The incapability in measuring the lowest calibration temperature by means of the pyrometers 2C-3000 and S-3000 must be noted in, although this temperature would be within their temperature range.

The temperature measured by the pyrometers in the experimental campaign is then corrected interpolating linearly between calibration spots.

3.2.5 Temperature measurement accuracy

Each temperature measuring instrument is affected by uncertainties. Some of these uncertainties and the relative grounds are already treated in the previous sections. The topic is completed in this section.

According to the works [30] and [31], a general formula for all devices (pyrometers, IR-camera and thermocouples) can be summarized as follows:

$$\Delta T_T = \sqrt{\sum_i \Delta T_i^2}, \quad (3.2.5.1)$$

where the “ ΔT_i ” are the uncertainties affecting the instrument in question and due to different uncertainty sources. They are listed below.

- ΔT_{in} refers to the measurement accuracy of the instrument, which is provided by the producer. See references [94], [101]-[105] and [108].
- ΔT_{re} accounts for the reproducibility error of the instrument, which is also provided by the producer. See references [94], [101]-[105] and [108] once again.
- ΔT_{di} is related to the inability of discriminating between two close temperature values. It includes the discrimination inability not only of the sensing element, but of the whole measurement chain. It is evaluated in the post-processing of the records through the maximal signal fluctuation when it has already reached the steady-state.
- ΔT_{ca} relates to uncertainties implicit in the calibration processes described in the previous sections. For the Minolta pyrometer it is reported in [106], for the remaining pyrometers it is estimated as the composition of their reproducibility error and the Minolta’s calibration uncertainty, while for the IR-camera as the composition of its reproducibility error and the pyrometers’ calibration uncertainty,
- ΔT_{IR} comprehends errors solely related to the infrared camera. They are basically due to the limited camera resolution capability, i.e. the camera is not able to accurately discriminate two neighbouring pixels. Because of the nature of the detector, the local temperature distribution for a considered spot is hence treated as Gaussian [108], so that the spot temperature is the mean value and the uncertainty $\Delta T_{IR} = \pm 2\sigma$, where σ is the standard deviation of the distribution.

The amounts of the uncertainties for the used devices are summarized in table 3.2.5.1.

Table 3.2.5.1. Summary of the uncertainties. The abbreviations “mv” and “rg” indicate if the value is referred to the measured value (in °C) or to the measurement range, respectively.

Uncertainty	2C3000/S3000	2C2000/S2000	Minolta	IR-Camera	TC
ΔT_{in}	$\pm 0.5\% \text{ mv } \pm 1^\circ\text{C}$	$\pm 1\% \text{ rg}$	$\pm 0.5\% \text{ mv}$	$\pm 2 \text{ K}$	$\pm 0.75\% \text{ mv}$
ΔT_{re}	$\pm 0.1\% \text{ mv } \pm 1^\circ\text{C}$	$\pm 0.3\% \text{ mv}$	$\pm 0.15\% \text{ mv}$	$\pm 1\% \text{ mv}$	$\pm 0.3\% \text{ mv}$
ΔT_{di}	$\pm 0.5\text{K}$	$\pm 1\text{K}$	$\pm 2\text{K}$	$\pm 3\text{K}$	$\pm 1\text{K}$
ΔT_{ca}	calibration process	calibration process	$\pm 2.5\text{K up to } 1000\text{K}$ $\pm 3\text{K for } 1000\text{-}1200\text{K}$	calibration process	- -
ΔT_{IR}	-	-	-	$\pm 2\sigma$ (Gaussian)	-

It is important to emphasize that the temperature measurement system consists of complementary devices. Thus a detailed post-processing permits to significantly increase the reliability of the acquired data, since suitable data can be used for correcting the other ones, e.g. tuning the emissivity and transmittance of the IR-camera thanks to the measurements of the pyrometers.

Chapter 4

Preliminary numerical investigations

This chapter deals with numerical simulations conducted for the double purpose of setting-up the coupling environment discussed in chapter 2 and inspecting the impact on the results of some physical phenomena, which can occur at an arc-heated facility like L3K.

The available geometry is a bi-dimensional model very close to the one, which is then actually investigated (see chapter 5).

As depicted in figure 4.1, the model concerned in this section consists of:

- a nose, characterized by a radius of 10 mm and made of copper. It is assumed to be maintained at a temperature of 500 K;
- two ceramic flat plates, made of C/C-SiC and 3 mm thick. The horizontal one is 262.47 mm long and is the main focus of the investigations. The vertical plate is positioned on the rear side and is 55 mm long;
- a base support, made of stainless steel and 10 mm thick. It is assumed to be kept at 300 K;
- infilling insulating material KAPYROK. This material is composed of aluminum oxide Al_2O_3 (91%) and of silicon dioxide SiO_2 (9%). Its properties can be referred to Schäfer [30] and are summarized in Appendix A. Thanks to its thermal conductivity much inferior to the values of C/C-SiC, copper and steel, it enables thermal separation between ceramics and components maintained at constant temperature.

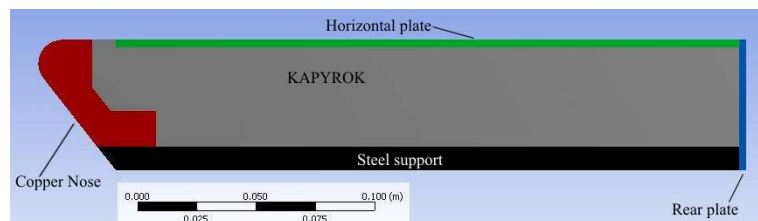


Figure 4.1. Bi-dimensional investigated model.

The geometrical data of the model are presented in more detail in Appendix C. The model is considered infinitely rigid and therefore neither deformations nor forces are taken into account. As already mentioned the running time of the L3K facility is rather long and allows reaching steady conditions on the surface. In view of the aim of the present investigations, the flow can hence be simulated as steady. Moreover, the structure analysis is reduced to a steady 2-D heat transfer problem.

The coupling interface between fluid and structure domains is limited for efficiency reasons to the upper surfaces of the vertical plate and the front isolating material as well as the horizontal plate, since the nose region and the base support are kept at nearly fixed temperature by cooling and the other surfaces do not give a significant contribution [31].

In consideration of the low Reynolds number (e.g. at the inflow $Re_\infty \sim 14000$), the flow is assessed to remain laminar throughout the whole field, see section 3.1.

The different components of the model are assumed to be in perfect thermal contact with each other.

The wall is treated as non-catalytic.

In order to study the effect of the angle of attack, the model is adjusted at 10° , 20° and 30° with respect to the flow centerline.

The set-up of flow and structure computations are described in sections 4.1 and 4.2. The first investigations (section 4.3) deal with frozen and uniform flow. They are fundamental for tuning the coupling procedure for all successive simulations and represent the reference results.

The influence of high-temperature gas effects and divergent flow are taken into account in sections 4.4, 4.5 and 4.6.

As already mentioned in section 1.3, the production process and the microstructure of the C/C-SiC are rather complex. Moreover, tolerances must be taken into account for the model manufacture. In view of that, deviations from the nominal values of geometry and structural properties must be considered. The work by Schäfer [30] deals with these issues. On the basis of an accurate sensitivity analysis, it is possible to assess that a variation of the plate thickness actually has no influence on the surface temperature and heat loads, while emissivity, heat conduction coefficients and nose radius require marked variations to have significant effects on the thermal quantities on the domains under investigation. For example, at the plate middle an uncertainty about 10% in the emissivity would yield to a variation of ca. 2% in the surface temperature, an uncertainty about 50% in the parallel and perpendicular heat conductivity to a variation of ca. 1% and 3%, respectively, and an uncertainty about 25% in the nose radius a variation of ca. 1%.

Also some facility flow parameters may present deviations and hence affect the results for the thermal quantities. This problem is similarly investigated by Mack on the same configuration [31]. In particular, the reservoir total enthalpy is estimated to undergo an uncertainty of $\pm 4.4\%$, which yields to a temperature variation on the plate surface of approx. $\pm 3\%$ and a heat flux difference up to $\pm 15\%$. Of course, the thermochemical modeling affects the results as well. The work [31] deals also with these issues, and allows sustaining that a diverse formulation of the reaction rates – as the one by Park [76] – even coupled with a

different thermochemical model – as the one by Esser [16] – determine a slight variation of the temperature (around 2%) but the corresponding difference in the heat flux can reach 10%.

The impact of these aspects must be taken into consideration when evaluating the results of the numerical simulations. However, no targeted analysis is performed in the current work for quantitatively estimating the amount of the uncertainties affecting these results.

4.1 Flow modeling

The flow is computed by means of the TAU code.

For efficiency reasons not the entire test chamber is simulated. The model support and the whole field below the model are neglected, as well as the complete field downstream of the vertical plate. This choice does not affect the focus of the investigations, according to [31]. Moreover, the assumption of uniform flow allows a further reduction of the domain to be computed in front and above the model. The fluid domain is thus simply rectangular.

The extension of the flowfield to be solved is plotted in figure 4.1.1.

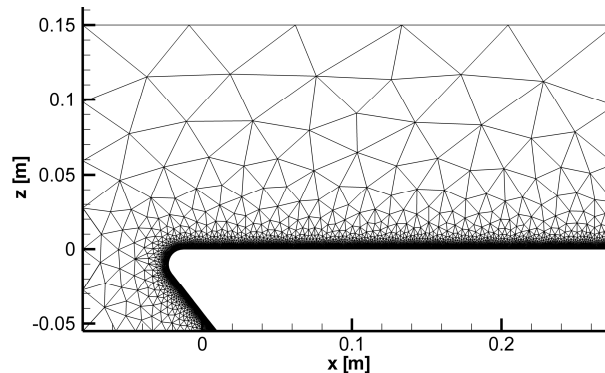


Figure 4.1.1. Fluid domain with initial mesh.

The hybrid mesh is generated by means of the software CENTAUR [110]. In proximity of the surface quadrangular elements are distributed in 28 layers in normal direction, with a minimal thickness of $3 \cdot 10^{-5}$ m close to the body and with a stretching ratio of 1.05 in normal direction. The rest of the flow domain is discretized by an unstructured grid made of triangles. In all, the initial number of elements amounts to approx. $6 \cdot 10^3$ and $5 \cdot 10^3$ for the unstructured and structured mesh, respectively. The mesh is adapted many times within the startup solution of the flow problem, especially in vicinity of the shock. The grid is then kept unaltered for the successive coupling iterations. The final grid for the 20° configuration is plotted in figure 4.1.2 as an example. The total number of elements of the conclusive grid adds up to ca. 10^5 and ca. $2 \cdot 10^4$ for the

unstructured and structured mesh, respectively, which is satisfactory according to [31]. The surface points on the coupling interface are around 300.

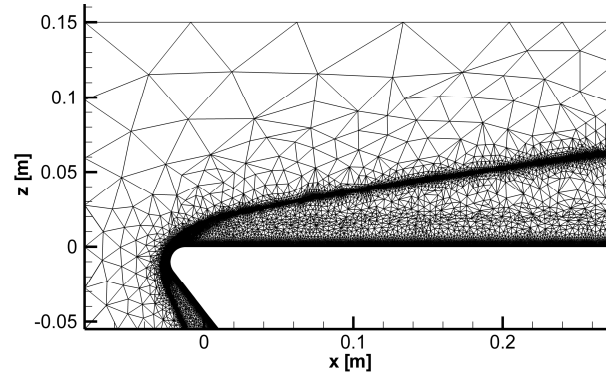


Figure 4.1.2. Final mesh for the flowfield (20° configuration).

The inflow conditions are imposed at the left boundary, while the right boundary is the outflow and the upper and lower boundary the far field. The initial grid is the same for all configurations: the different problem is then easily obtained by changing the stream orientation in the inflow and the far field.

The model surface completes the flowfield boundary. The contours of the nose region and base support provide uniform boundary temperatures of 500 K and 300 K, respectively. The temperature distribution over the coupling interface is determined at each inter-field coupling iteration by the structure solution. This is of course unavailable at the first flow solution step; therefore the coupling interface is initially modeled at radiative equilibrium, namely neglecting the structural feedback. The emissivity has hence the suitable values of 0.95 for the isolation material and 0.9 for the horizontal and vertical plates. It must be underlined that the TAU-code assumes a background temperature of 0 K for surface radiation. The radiation of nose and base support are neglected in view of both, their low temperature and emissivity.

Starting from the first inter-field iteration, the radiation is naturally integrated in the structure problem, and the temperature distribution is imposed at the whole model surface as boundary condition for the flow solver.

The multi-grid scheme chosen for the flow solution is of type “3v”, with upwind discretization AUSMDV and Van Leer preferred for the fine and coarse meshes, respectively.

4.2 Structure modeling

The solution of the thermal problem is obtained from the ANSYS code. All important components of the considered model are comprehended in the structure simulation, which means the horizontal plate, the vertical plate, the

isolating part in front of the horizontal plate as well as the isolation which fills the inner space between plate and base, see figure 4.2.1. The nose region and the base are dispensed from simulation, since they are maintained at fixed temperatures. They are simply taken into account as boundary conditions, i.e. $T=500\text{ K}$ and $T=300\text{ K}$ at the contact interfaces with the nose region and with the base, respectively.

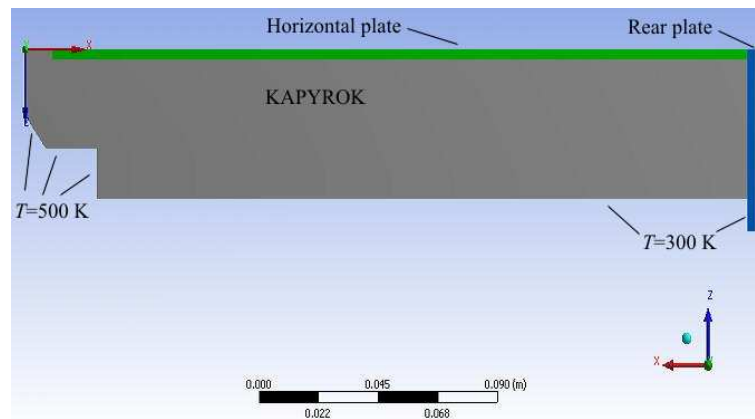


Figure 4.2.1. Solved structure field and relative coordinate system.

The non-linear temperature-dependent properties of the employed materials and the orthotropic behaviour of the ceramics are taken into consideration inside the structure modeling.

Since the calculation effort needed by the thermal problem is rather low, it is possible to generate a very fine mesh. The quasi-structured grid is composed by quadrangular elements with a temperature degree of freedom per node and with a side dimension of ca. $2.5 \cdot 10^{-4}\text{ m}$, as depicted in figure 4.2.2. The radiation towards the background (which is assumed at a suitable temperature value of 300 K) is taken into account by means of surface elements, which deal with the radiative cooling at the coupling interface. Moreover, the energy transfer inside the model between regions with different characteristics is managed by appropriate contact and target elements.

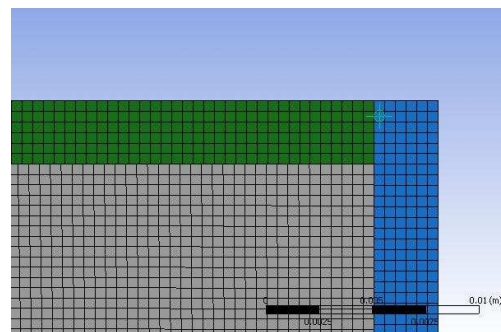


Figure 4.2.2. Quasi-structured mesh on the rear side.

The coupling quantity – the surface heat flux coming from the solution of the fluid problem – is interpolated at each inter-field iteration step on the nodes of all elements, which lie on the interface. The nodal heat flux distribution acts then as load for the thermal problem. The structural answer in terms of surface temperature is afterwards interpolated on the coupling interface nodes of the fluid grid. It determines the updated boundary condition for the flow domain in terms of surface temperature.

The interpolation process is qualitatively sketched in figure 4.2.3. The heat load to be applied on the considered structure node (in black) is interpolated from the flow grid neighbouring nodes (in grey) which are closer to it. The operation is accomplished for each structure node. The interpolation of the temperature from the structure onto the flow grid is analogously performed.

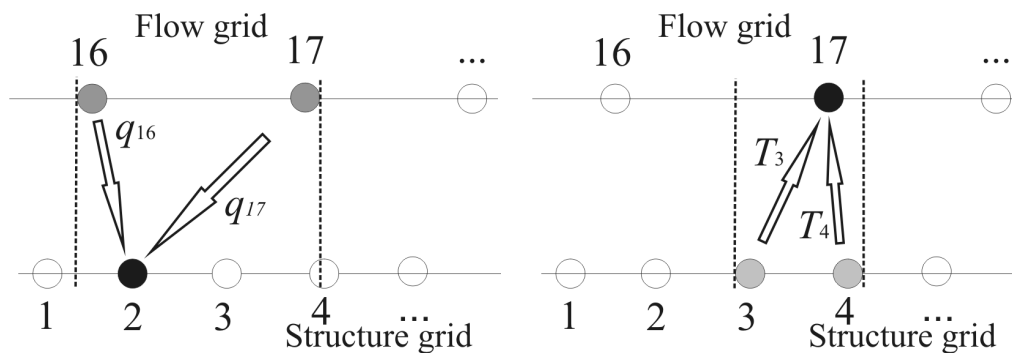


Figure 4.2.3. Sketch of the thermal load interpolation onto the structure nodes (left) and of the temperature b.c. interpolation onto the flow nodes (right).

4.3 Perfect gas computations

The flow conditions refer to Mack [31], with inflow conditions obtained from numerical simulations of the whole wind tunnel at chemical non-equilibrium (and thermodynamic equilibrium) with the chemical reactions model of air suggested by Gupta [77]. The investigated flow in the concerned domain is then modeled as a perfect gas with suitable gas properties, following the procedure expounded in section 2.2. Emphasis must be put on the chemical composition of the high-enthalpy gas: because of the very high reservoir temperature, oxygen is almost completely dissociated, while an amount of NO is present and only a very small percentage of nitrogen is dissociated. The considered reservoir and inflow conditions are presented in table 4.3.1, whereas the adapted perfect gas properties are summarized in table 4.3.2.

Table 4.3.1. Reservoir and inflow conditions in L3K facility (from ref. [31]).

T_0 [K]	5400
p_0 [Pa]	$4.55 \cdot 10^5$
h_0 [MJ/kg]	10.82
Ma_∞	7.62
T_∞ [K]	463.7
p_∞ [Pa]	51.95
ρ_∞ [kg/m ³]	$3.32 \cdot 10^{-4}$
V_∞ [m/s]	3678
α (N ₂)	0.763
α (O ₂)	$3.93 \cdot 10^{-3}$
α (NO)	$9.30 \cdot 10^{-3}$
α (N)	$2.24 \cdot 10^{-6}$
α (O)	0.224
Mass flow rate [kg/s]	0.142

Table 4.3.2. Perfect gas properties (from ref. [31]).

R [J/(kg K)]	346.0
γ	1.462
Pr	0.72
Sutherland's T_{ref} [K]	273
Sutherland's μ_{ref} [Pa s]	$1.716 \cdot 10^{-5}$

The results at the coupling surface for the radiative equilibrium case are available after the adaptation cycle for the startup solution. The temperature and Mach number fields for the three configurations are depicted in figures 4.3.1 to 4.3.3.

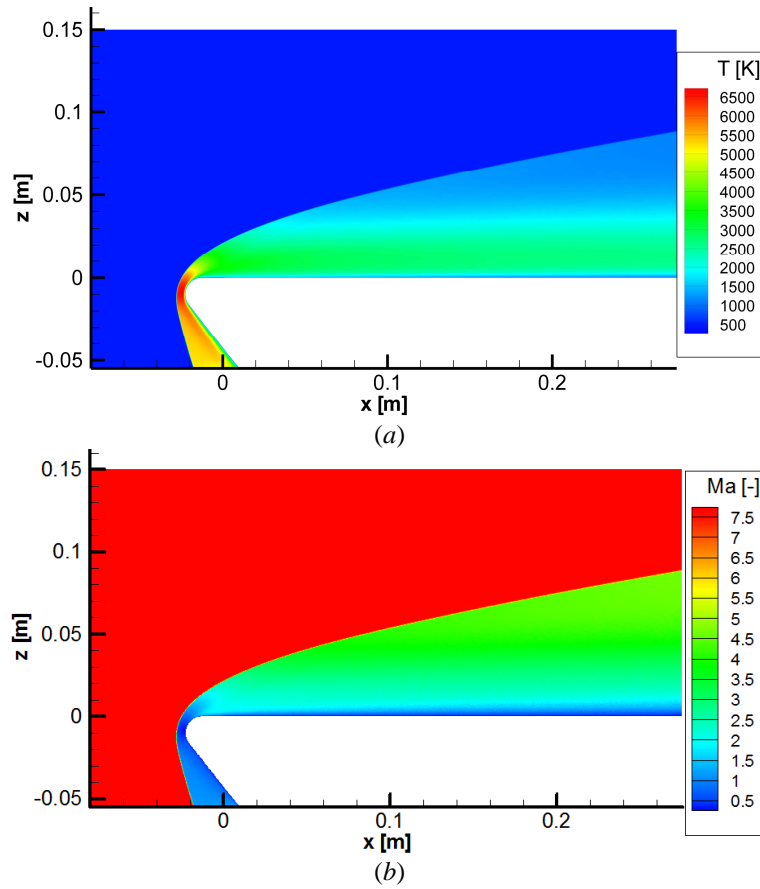


Figure 4.3.1. Distribution of temperature (a) and Mach number (b) in the flowfield. Perfect gas modeling. $\alpha=10^\circ$.

It is possible to notice the very good resolution of the bow shock. The maximal temperature in the fluid domain is reached after the shock in front of the nose region, in proximity of the stagnation point. It amounts to ca. 6630 K for all configurations.

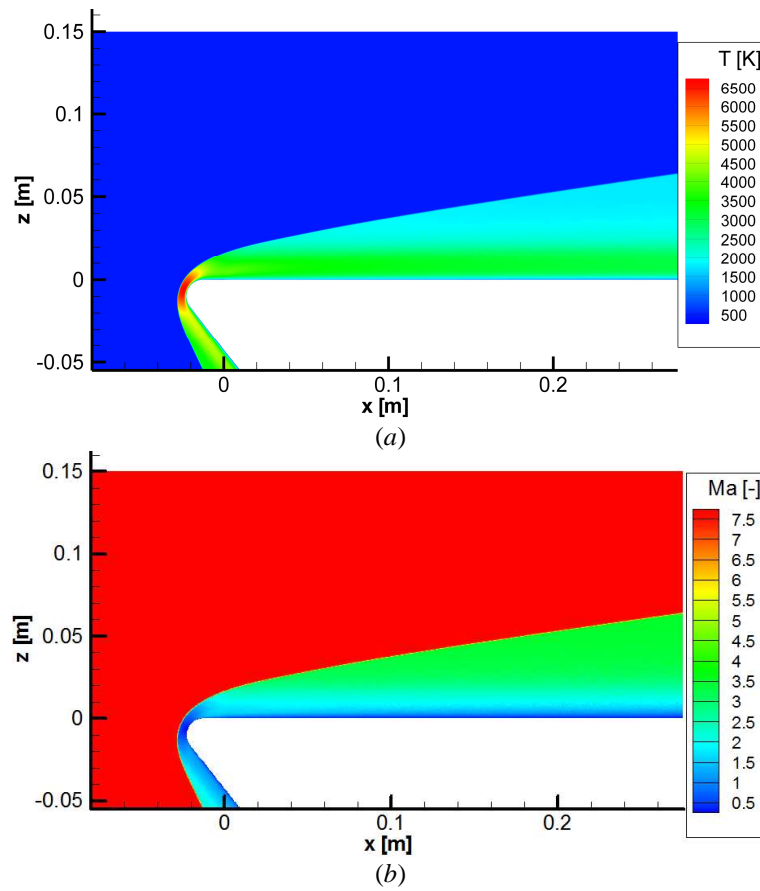


Figure 4.3.2. Distribution of temperature (a) and Mach number (b) in the flowfield. Perfect gas modeling. $\alpha=20^\circ$.

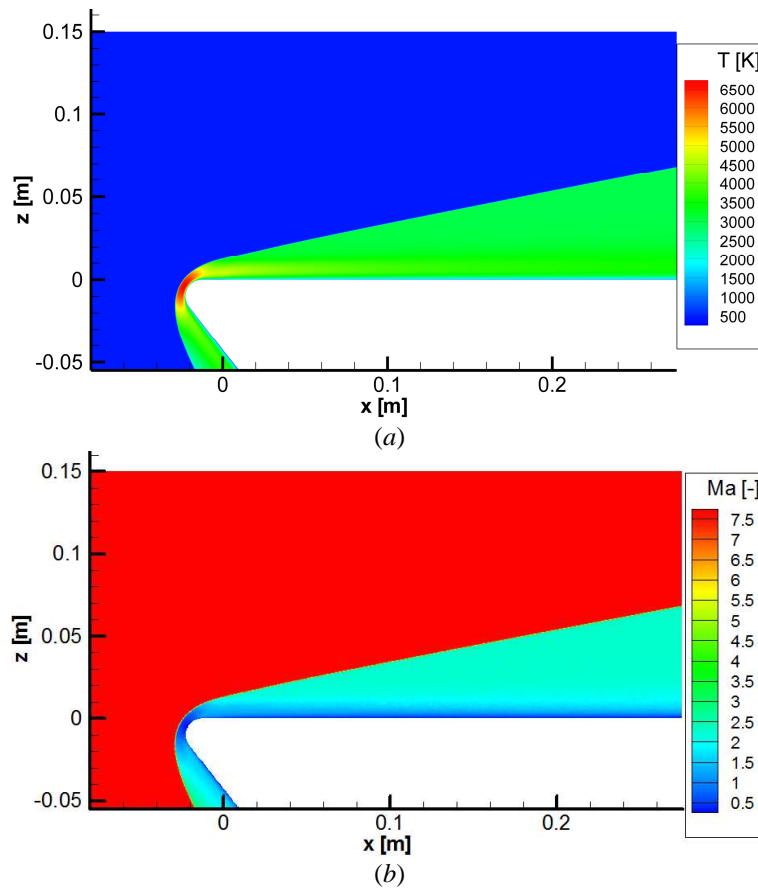


Figure 4.3.3. Distribution of temperature (a) and Mach number (b) in the flowfield. Perfect gas modeling. $\alpha=30^\circ$.

The temperature trend at radiative equilibrium on the horizontal and rear plate surfaces is depicted in figure 4.3.4. The surface distributions of the thermal quantities are plotted in this work in correspondence of the flow mesh nodes at the wall for both, the uncoupled and coupled solutions.

The temperature distribution on the surface shows a slight negative gradient downwards. The closeness of the shock and hence the very high thermal load, together with the boundary condition of $T=500$ K on the nose domain, determines a remarkable temperature jump on the surface of the isolation material in front of the horizontal plate. It has been preferred not to introduce an intensive refinement on this region, since the interest is concentrated on the horizontal plate. The resolution of the positive gradient is therefore rather low. This is common also for all subsequent simulations.

Because of the difference in the emissivity between KAPYROK and C/C-SiC, the latter has a weaker cooling performance by radiation, and consequently the maximum in the surface temperature distribution arises on the horizontal plate in vicinity of the connection zone (which is at $x=10$ mm). The maximum amounts

to 1192 K, 1259 K and 1340 K for the 10°, 20° and 30° configuration, respectively, and occurs for the former two at $x=12$ mm and for the latter at $x=14$ mm.

The effect of the higher angle of attack must be emphasized, since at 30° the surface temperatures reach higher values of about 140-150 K and 80-90 K in comparison with the 10° and 20° configuration, respectively.

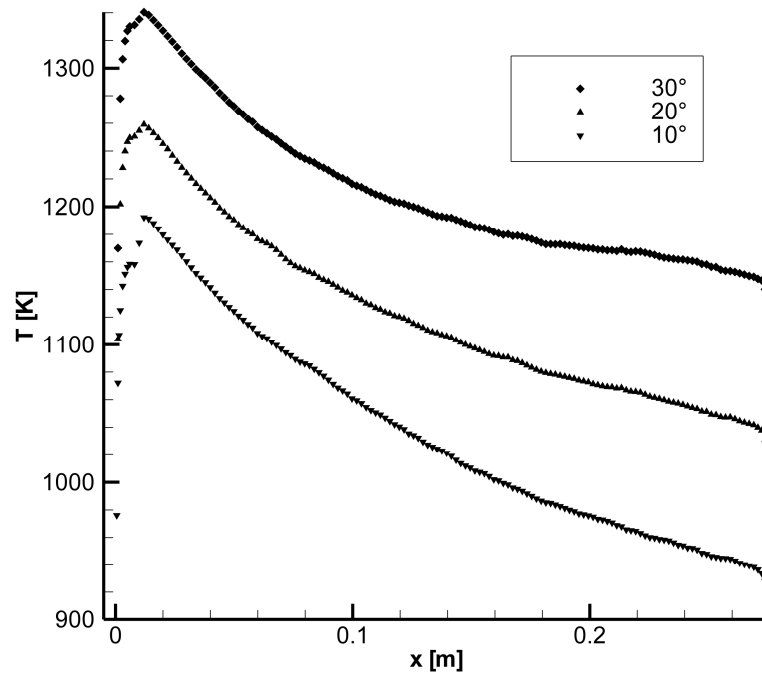


Figure 4.3.4. Temperature distribution on the coupling surface. Perfect gas modeling with radiative equilibrium boundary condition.

The heat flux distribution for radiative equilibrium is shown in figure 4.3.5 and is obviously similar to the temperature trend. After the peak on the front, the load decreases along with the longitudinal coordinate from a maximal value of ca. 95, 130 and 170 kW/m² to a minimum of ca. 35, 60 and 85 kW/m² for the 10°, 20° and 30° configuration, respectively.

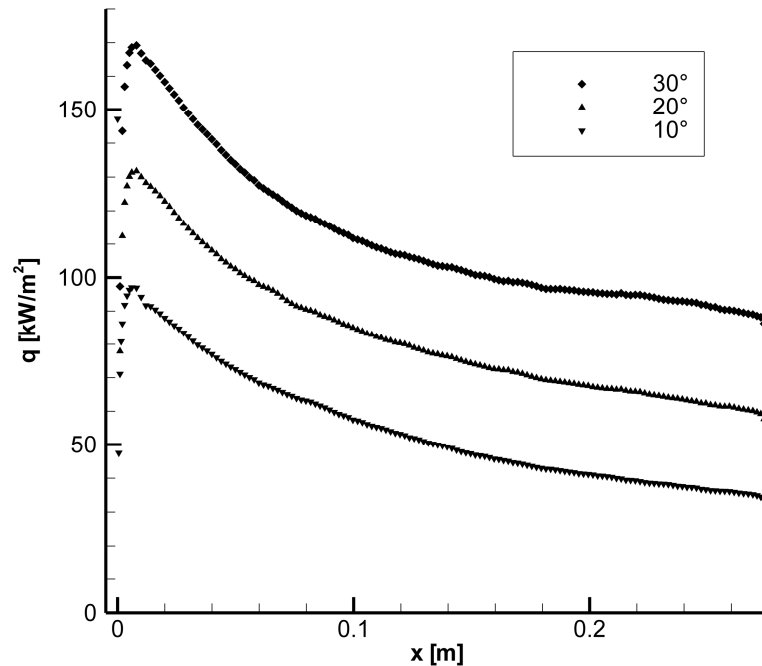


Figure 4.3.5. Heat flux distribution on the coupling surface. Perfect gas modeling with radiative equilibrium boundary condition.

The initial surface heat flux evaluated by the radiative equilibrium solution allows starting the structure computation.

The structure has an evident influence on the investigated problem. Figure 4.3.6 displays the temperature distribution inside the model, whereas figures 4.3.7 and 4.3.8 deal with the heat flux distribution. They are all taken from the first coupled simulation of the 30° configuration.

The heat conduction inside the model determines a heat flow from hot to cold regions. Although the heat conduction in z -direction between the hot surface and the cold base represents a component of the thermal response, there is a very interesting in-plane heat transfer inside the horizontal plate, see figure 4.3.7 (a). This is accentuated by the presence of the isolating block under the 3 mm plate, the heat conductivity of which is around two orders of magnitude less than the ceramics' one. Also due to the orthotropic properties of the C/C-SiC, which are characterized by the heat conductivity parallel to the fibers being nearly double than the perpendicular one, part of the load “prefers” being transported along the plate to the back of the model instead of being transported in z -direction.

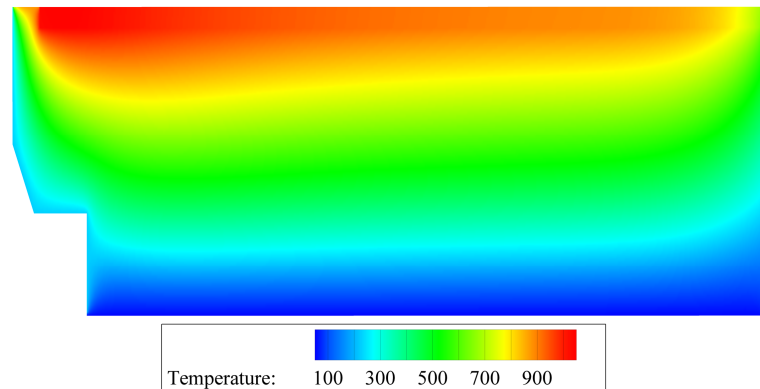
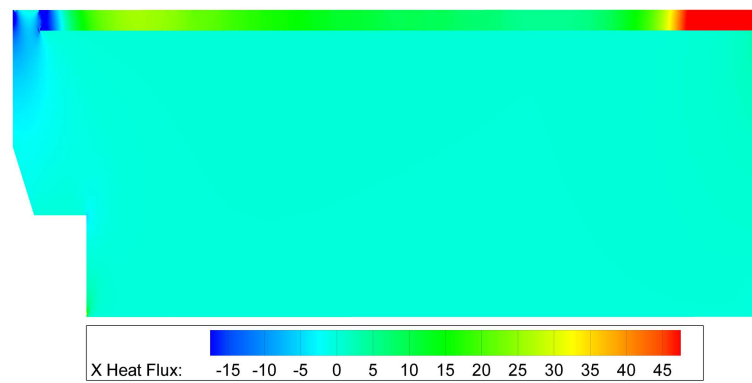
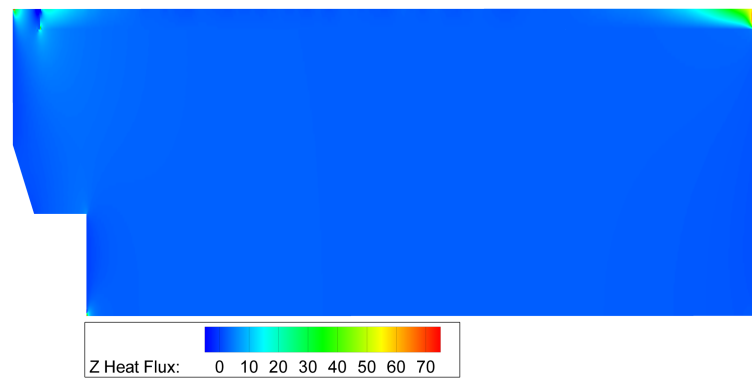


Figure 4.3.6. Temperature distribution inside the structure (30° case). Temperature in °C.



(a)



(b)

Figure 4.3.7. Distribution of the x - (a) and z - (b) components of the heat flux inside the structure (30° case). Data in kW/m^2 .

Emphasis must be placed on the nearly uniformity of this in-plane heat transfer on a large portion of the horizontal plate. In fact, the not-emitted heat flux splits up in the fore region in a longitudinal component, which transfers either forwards or backwards, and in a perpendicular component, which enters the

insulation. Figure 4.3.8 (a) helps pointing out this occurrence. The longitudinal gradient of the in-plane component on the horizontal plate is rather slight. Its contribution to the local heat transfer problem described in section 2.1 is thus almost insignificant.

At the rear side, the heat flux is either emitted or transferred downwards through the vertical plate, see figures 4.3.7 (b) and 4.3.8 (b). The latter has indeed fibers oriented in z -direction and the heat conduction effect of dragging the thermal load from the hot region to the cold base is manifest.

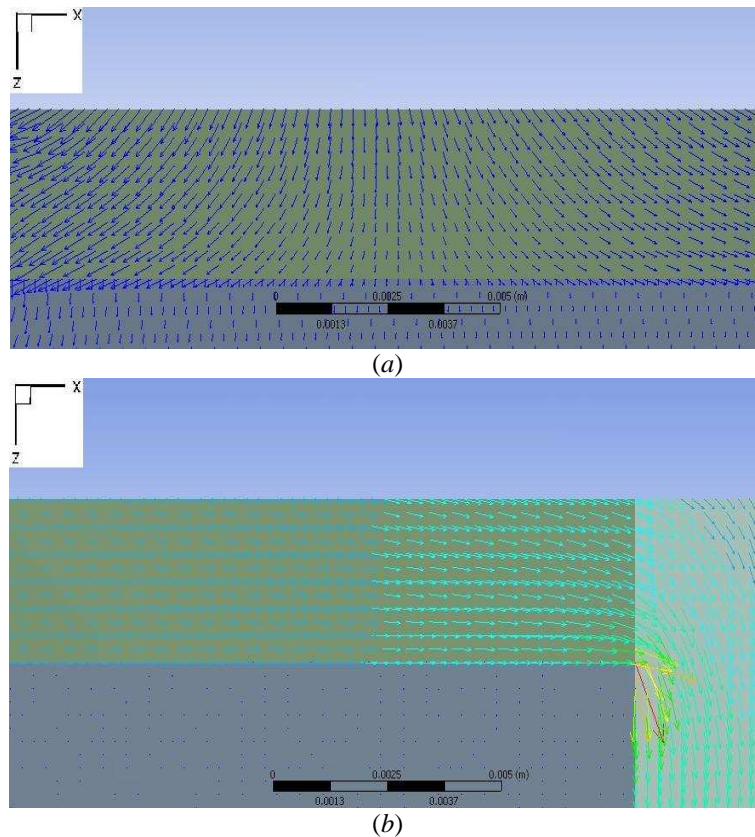


Figure 4.3.8. Qualitative heat flux vector distribution in the structure (30° case). (a): between 15 and 30 mm (front). (b): between 260 and 275 mm (back).

Because of its very low heat conductivity, the isolating component in front of the horizontal plate keeps to realize surface cooling by means of almost pure radiation towards the background. In view of that, it is understandable that the pronounced positive temperature gradient on the surface of this KAPYROK piece from the boundary condition of 500 K remains similar to the startup solution. On the contrary, the temperature peak at the crossing region between the front isolation and the horizontal plate is smoothed thanks to the heat conduction influence. The temperature evolution on the interface is plotted in

figure 4.3.9. The maximal surface temperature amounts this time to 1114, 1214 and 1299 K, and it arises at $x=20$ mm, $x=16$ mm and $x=18$ mm for the 10° , 20° and 30° configuration, respectively. The highest values correspond in general no longer to a peak but to a plateau, which extends to a width of ca. 15-20 mm with a few degrees difference.

Moreover, the drag-effect of the rear plate determines a clear impact on the temperature distribution on the back. There is no longer a slight but a significant negative gradient on the coupling surfaces of both, the horizontal and vertical plate.

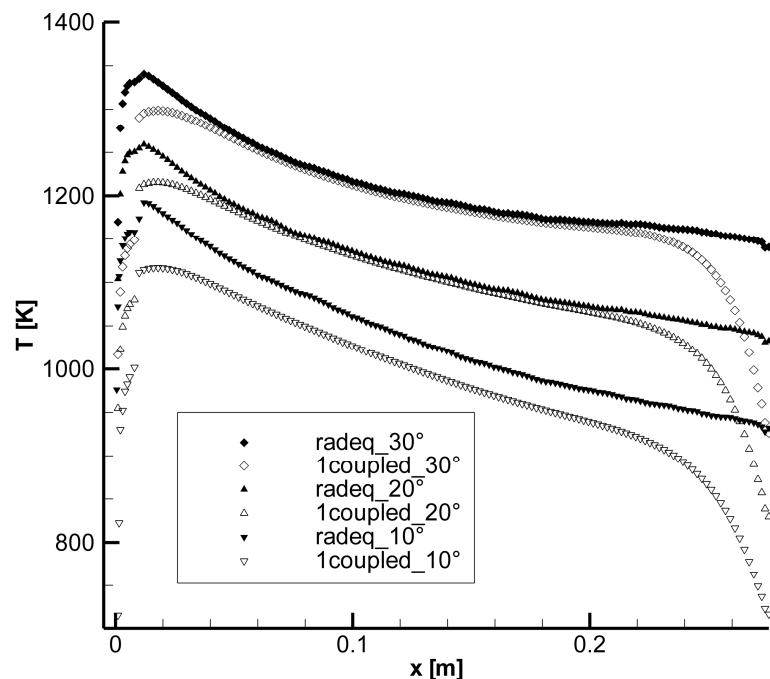


Figure 4.3.9. Temperature distribution on the coupling surface. Perfect gas modeling with fluid-structure interaction (1st coupling) and comparison with the uncoupled results.

The temperature decrease between startup and first coupled solution in the central part of the coupling surface is nearly uniform and it is less than 40 K, even less than 10 K for the higher angles of attack. On the other hand, the influence of the structure in alleviating the surface temperature level on both, the front and the back, is impressive, with a decrease by even 420 K on the former and 250 K on the latter. In general, the capability of the structure in reducing the surface temperature is demonstrated.

Since the surface temperature distribution is different, also the heat flux loading the surface varies after the first coupling iteration, see figure 4.3.10. Of course, the more important differences keep in pace with the temperature variation, and

hence occur on the front and rear coupling surfaces. The loading heat flux is in fact predicted satisfactory on the central surface assuming radiative equilibrium conditions: the difference with the first coupling solution is less than 2 kW/m^2 . The most remarkable variations arise where the temperature decrease is noteworthy and hence where the radiative cooling becomes lower and the thermal gradient in the boundary layer becomes more pronounced. The load increase on the fore and rear surfaces can reach ca. 80 kW/m^2 (10° configuration) and 15 kW/m^2 (30° configuration), respectively. It is remarkable that on the back side the heat flux undergoes a flat region and behind that encounters even a positive gradient.

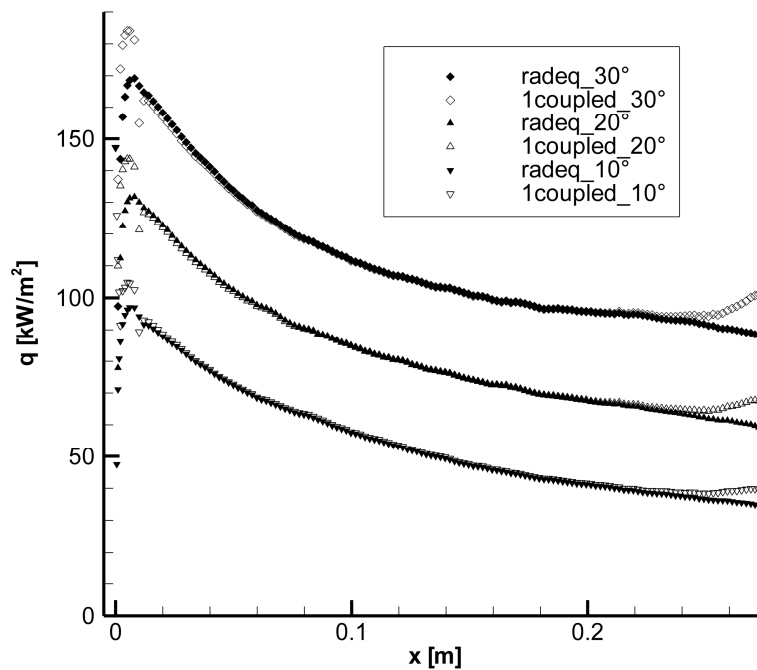


Figure 4.3.10. Heat flux distribution on the coupling surface. Perfect gas modeling with fluid-structure interaction (1st coupling) and comparison with the uncoupled results.

The temperature field shows no particular differences with the radiative equilibrium and its depiction is dispensed. This is common for all further inter-field iterations and for all successive investigations.

After the first coupling, the successive inter-field iterations focus on convergence, the results do not considerably differ from the ones above. Figures 4.3.11 and 4.3.12 help pointing out this fact.

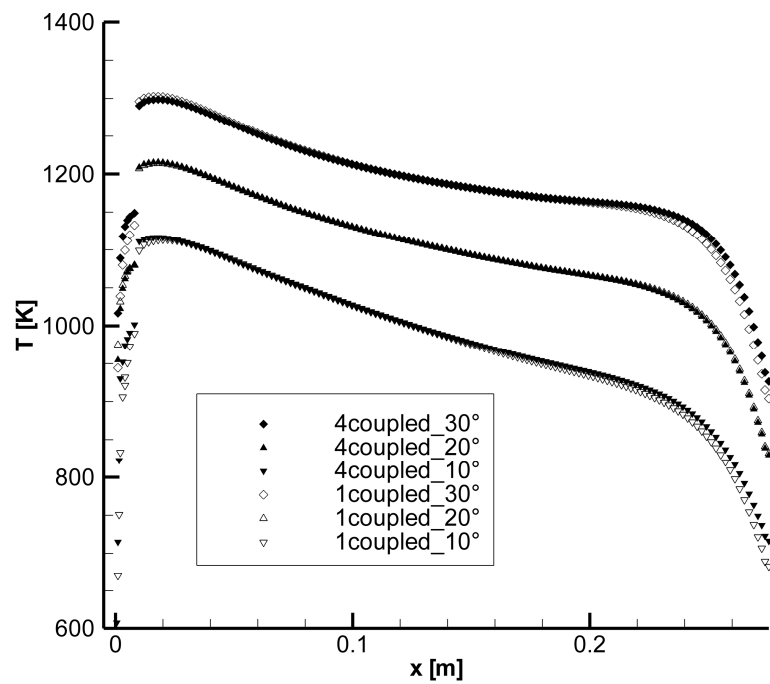


Figure 4.3.11. Temperature distribution on the coupling surface. Perfect gas modeling with fluid-structure interaction. Comparison between 1st and 4th coupling results.

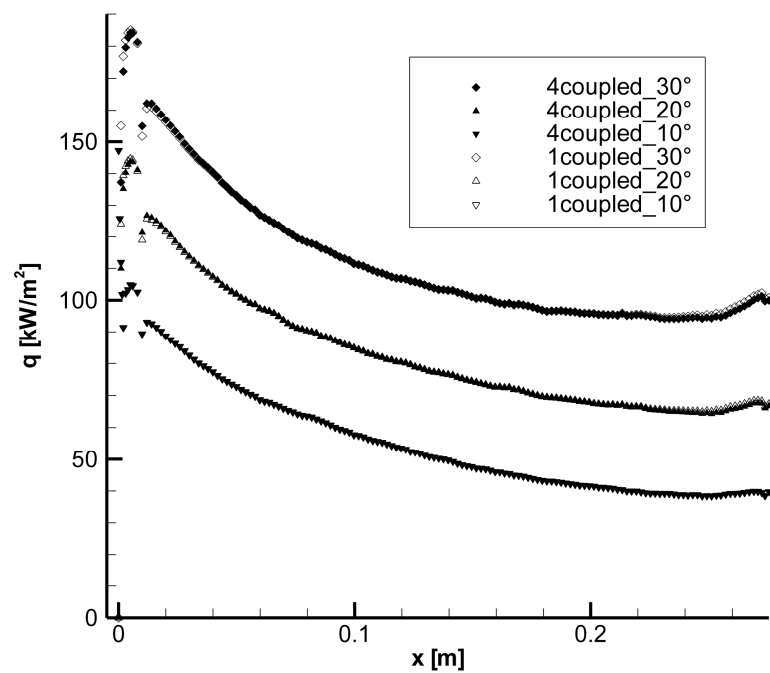


Figure 4.3.12. Heat flux distribution on the coupling surface. Perfect gas modeling with fluid-structure interaction. Comparison between 1st and 4th coupling results.

Convergence is reached after 4 coupling iterations and there is no need of the relaxation parameter Φ introduced in (2.3.2), since the convergence is stable (i.e. Φ is set equal to 1). The display of the temperature evolution inside the structure is therefore dispensed, while the comparison of the thermal quantities distributions between 1st and 4th iteration is plotted only in this section.

Tables 4.3.3 to 4.3.5 summarize the convergence of surface temperature and heat flux with respect to the inter-field iterations.

Table 4.3.3. Convergence of the thermal quantities. Perfect gas modeling. $\alpha=10^\circ$.

Iteration	ΔT_{\max}	$\Delta T_{x=0.14\text{m}}$	Δq_{\max}	$\Delta q_{x=0.14\text{m}}$
uncoupled - 1	-4.18E+02	-3.52E+01	7.84E+04	3.74E+02
1 - 2	-1.98E+02	-2.55E-01	-5.78E+04	1.18E+02
2 - 3	1.38E+02	-6.62E-01	3.39E+04	-1.12E+02
3 - 4	-3.67E+01	-3.17E-02	-1.71E+04	-1.08E+01

Table 4.3.4. Convergence of the thermal quantities. Perfect gas modeling. $\alpha=20^\circ$.

Iteration	ΔT_{\max}	$\Delta T_{x=0.14\text{m}}$	Δq_{\max}	$\Delta q_{x=0.14\text{m}}$
uncoupled - 1	-2.01E+02	-5.68E+00	4.63E+04	1.31E+02
1 - 2	3.00E+01	1.70E-01	1.84E+04	6.61E+01
2 - 3	-9.71E+00	-4.00E-02	-6.13E+03	-1.03E+01
3 - 4	3.22E+00	2.00E-02	1.95E+03	1.42E+00

Table 4.3.5. Convergence of the thermal quantities. Perfect gas modeling. $\alpha=30^\circ$.

Iteration	ΔT_{\max}	$\Delta T_{x=0.14\text{m}}$	Δq_{\max}	$\Delta q_{x=0.14\text{m}}$
uncoupled - 1	-2.39E+02	-5.26E+00	5.77E+04	-3.44E+01
1 - 2	-9.43E+01	3.26E-01	2.31E+04	-2.18E+01
2 - 3	3.30E+01	-9.00E-02	-7.84E+03	5.80E+00
3 - 4	-1.10E+01	-7.01E-02	2.52E+03	6.73E-01

It is important to understand the quantitative relationship between the acting load and the heat fluxes which either are emitted by the surface or go inside the structure. Figure 4.3.13, taken from the horizontal plate at 10° angle of attack as an example, is helpful for this purpose. The heat load at the surface q_w comes from the flow solution of the converged coupled simulations, whereas the radiative and convective heat fluxes q_r and q_c are evaluated from the surface elements of the converged structure computations.

It is evident that the radiation towards the background contributes with more than 90% - in the middle up to 97% - to the cooling of the surface in its central region, confirming the very good cooling performance of the C/C-SiC material introduced in section 1.3. The heat flow transferred inside the model by conduction is here nearly uniform and rather low, while the radiative heat flux has clearly a behaviour close to the one of the thermal load. The situation

changes on the front and back surface, where the proved heat conduction effects account for several percentage points of the total heat flux. The phenomenon is particularly impressive on the rear, where the heat flux transferred by conduction gets to the point of exceeding the radiative cooling contribution.

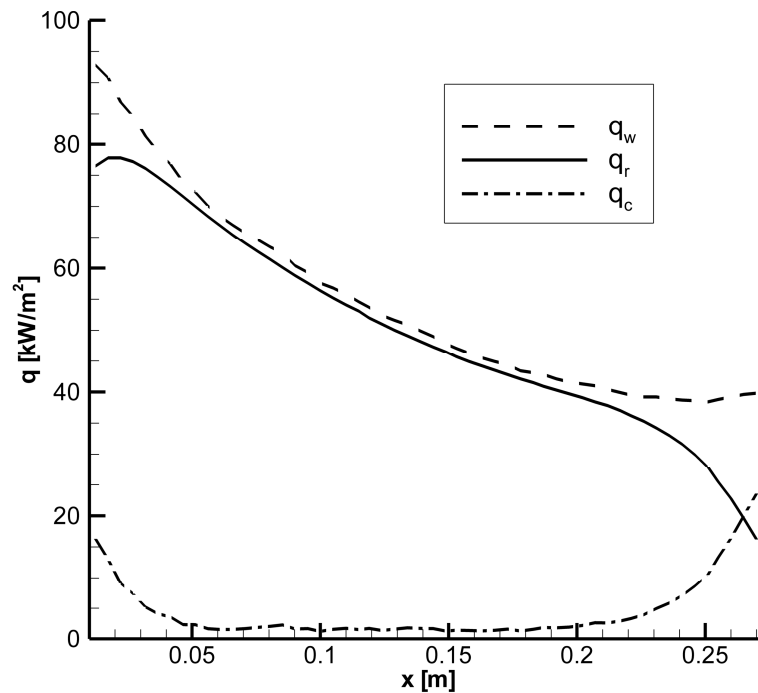


Figure 4.3.13. Heat flux distribution on the coupling surface. Relationship between components of the heat flux and comparison with the acting load.

4.4 Model flow in thermochemical non-equilibrium

Although the gas is practically frozen in the test chamber, the TAU code offers the possibility of performing non-equilibrium computations in order to assess which influence on the model the thermochemical phenomena may have. The set-up of the simulations in thermal and chemical non-equilibrium is the same as before, see sections 4.1 and 4.2. The grid fineness for the flow solver after adaptation is comparable with the previous computations, while the structural model is the same. The chemistry is modeled by means of the 17-reactions model for the 5 species air mixture [77], with the same inflow mass fractions as for the perfect gas simulations (see section 4.3). The reaction model is reported in Appendix B. Since the mass fractions of O₂ and NO are very low at these wind-tunnel conditions, the vibrational degree of freedom must be taken into account for N₂ only. Its vibrational temperature at the inflow amounts to 4375 K [111], as presented in table 4.4.1 together with the other concerned inflow quantities.

Table 4.4.1. Inflow conditions for thermochemical non-equilibrium modeling in test chamber.

Ma_∞	7.62
T_∞ [K]	463.7
p_∞ [Pa]	51.95
ρ_∞ [kg/m ³]	$3.32 \cdot 10^{-4}$
V_∞ [m/s]	3678
$\alpha(\text{N}_2)$	0.763
$\alpha(\text{O}_2)$	$3.93 \cdot 10^{-3}$
$\alpha(\text{NO})$	$9.30 \cdot 10^{-3}$
$\alpha(\text{N})$	$2.24 \cdot 10^{-6}$
$\alpha(\text{O})$	0.224
T_{vib} [K]	4375.0

Because of the increased complexity of the flow solution, its computational time grows up.

It must be underlined that the inflow conditions obtained from [31] are based on calculations conducted with chemical non-equilibrium, but at thermodynamic equilibrium, since at that time there was no thermochemistry accounting for vibrational relaxation available in the TAU code. The effects of thermal non-equilibrium will be taken into account in section 4.6.

Moreover, for the sake of efficiency only the configurations at 10° and 20° angle of attack are simulated in the present investigations. The computations are, anyway, satisfactory for examining the influence of thermochemistry.

The results of the startup simulations allow pointing out the first differences from the perfect gas modeling. The thermochemical processes determine some variations on the temperature field, which is shown in figures 4.4.1 and 4.4.2. Although the shock shape remains similar as found with perfect gas modeling, the shock line is closer to the body, consequence of dissociation phenomena across it [18].

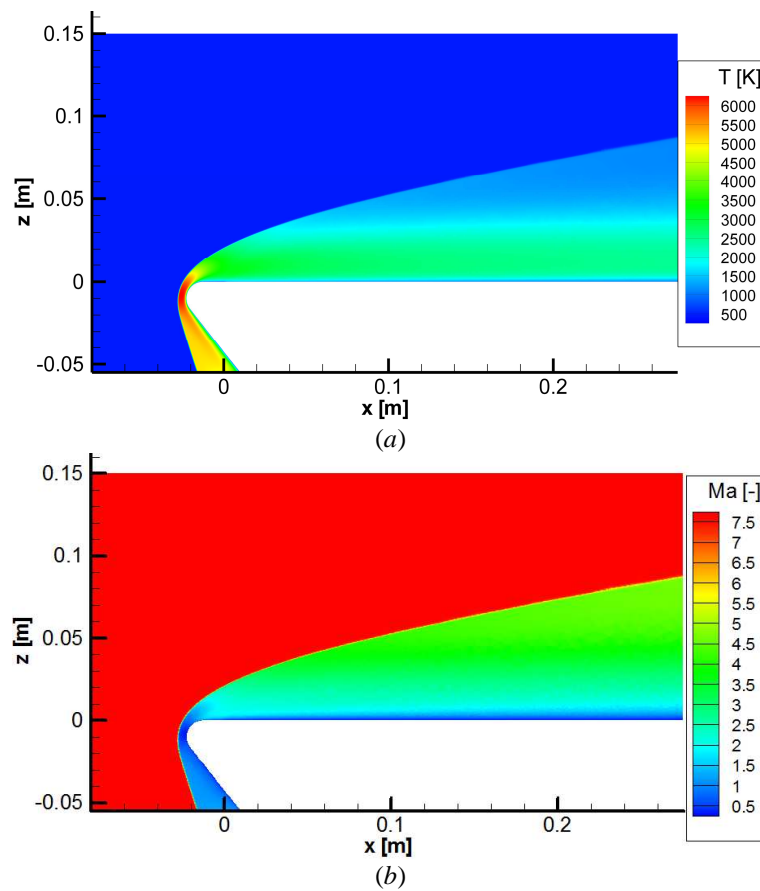


Figure 4.4.1. Distribution of temperature (a) and Mach number (b) in the flowfield. Model flow in thermochemical non-equilibrium. $\alpha=10^\circ$.

The increased closeness of the shock is more pronounced in the flowfield, both far above the model and in front of nose and base region. The topologic variation for the 20° configuration is, however, less remarkable.

The temperature level in the fluid domain is inferior, with a maximal temperature of about 6420 K, more than 200 K inferior to the results of section 4.3.

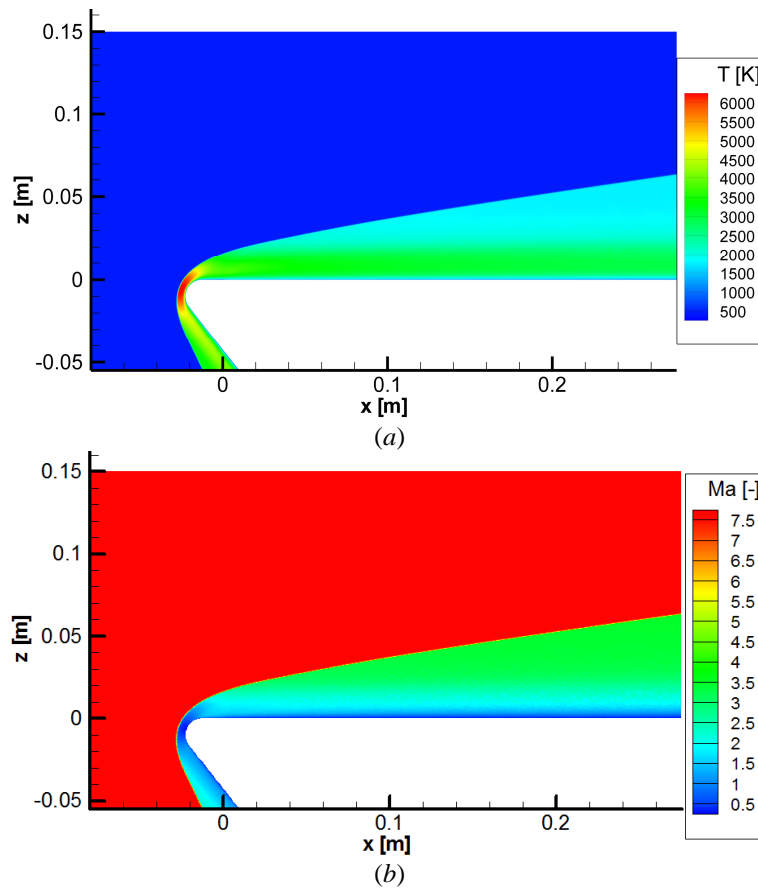


Figure 4.4.2. Distribution of temperature (a) and Mach number (b) in the flowfield. Model flow in thermochemical non-equilibrium. $\alpha=20^\circ$.

A few sections in the temperature field perpendicularly to the surface help emphasizing the mitigation of the temperature profile in z -direction and the closeness of the shock to the surface. Figure 4.4.3, taken from the results for the lower angle of attack, serves as an example.

Anyway, it is important to underline that at the surface and in its vicinity the situation is mostly inverted.

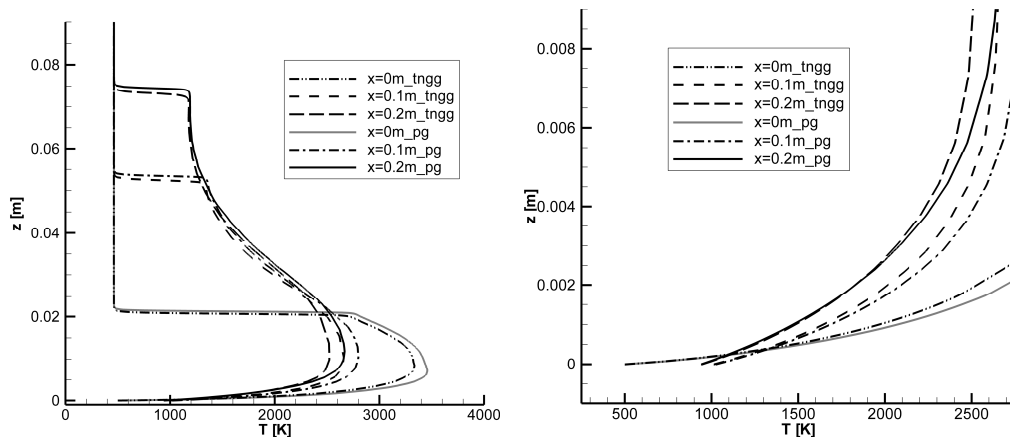


Figure 4.4.3. Comparison of the temperature profiles in perpendicular direction (left) and zoom in proximity of the surface (right). 10° configuration.

As depicted in figure 4.4.4, the surface temperature at radiative equilibrium is indeed everywhere higher than for the perfect gas model, and this occurs for both, 10° and 20° configuration. Moreover, the temperature gradient at the wall is in general less pronounced than for the ideal gas case. The heat flux loading the model is thus generally lower, see figure 4.4.5. The abbreviation “pg” indicates the simulations with frozen flow, while “tngg” the modeling with thermochemical non-equilibrium.

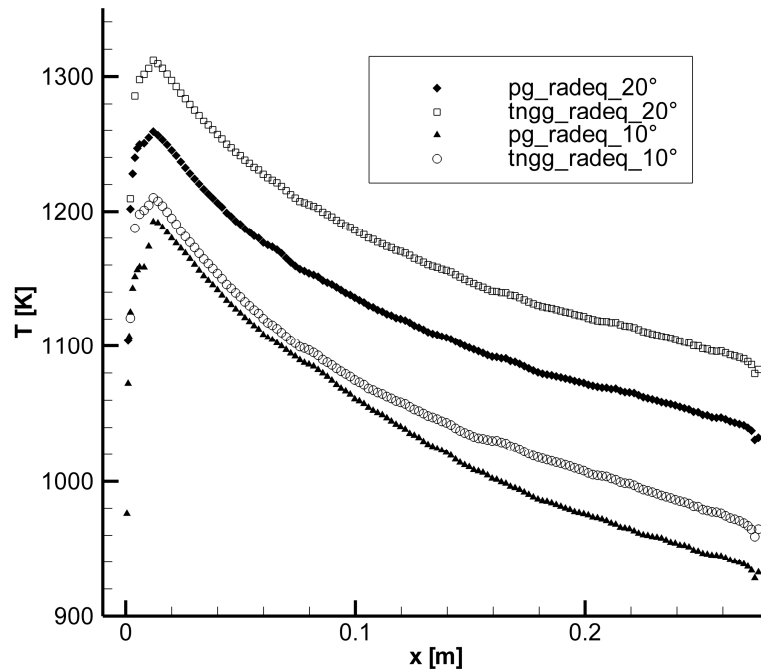


Figure 4.4.4. Temperature distribution on the coupling surface. Gas in thermochemical non-equilibrium with radiative equilibrium b.c. and comparison with perfect gas modeling.

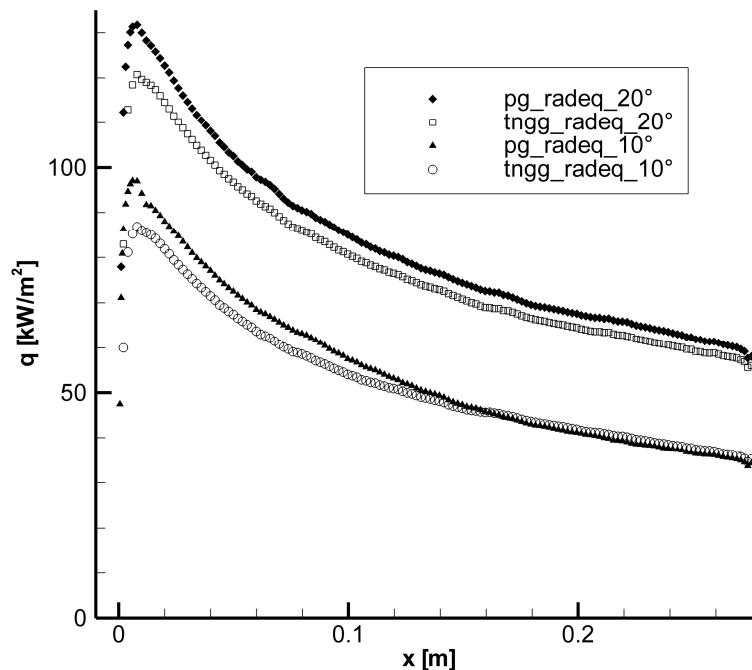


Figure 4.4.5. Heat flux distribution on the coupling surface. Gas in thermochemical non-equilibrium with radiative equilibrium b.c. and comparison with perfect gas modeling.

The temperature and heat flux distributions on the surface have very similar trends in comparison with the perfect gas case. Anyway, there is an interesting aspect concerning the results for the lower angle of attack, which needs a particular attention. Whereas the temperature increase for the 20° configuration is almost uniform and equal to ca. 50 K (corresponding to an increase by approx. 4%), in the 10° case it grows up with the longitudinal coordinate from a minimum about 15 K on the front (increase by approx. 1.5%) to a maximum of ca. 30 K on the rear side (increase by approx. 3%). These relative variations have been normalized to the local value of the thermal quantity computed in section 4.3; the procedure is applied in the following, too.

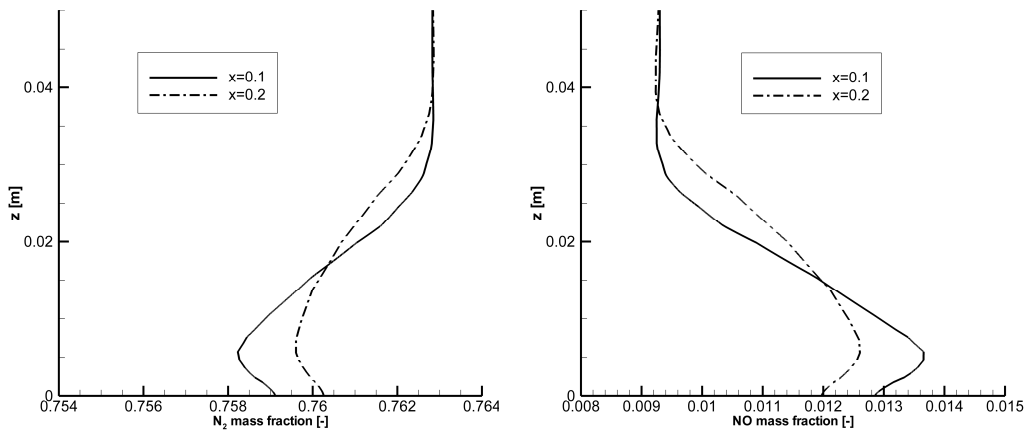
The heat flux keeps decreasing with x , but its gradient becomes less negative, such that at $x \sim 0.15$ m the loads evaluated with the perfect gas and thermochemical modeling are equal, and backwards the latter is even higher than the former. This is explainable considering again the layer in proximity of the wall. Taking two perpendicular sections of the temperature field at $x=0.1$ m and $x=0.2$ m, it points out that at the second position the local temperature gradient normal to the surface is more accentuated than in the perfect gas case, while it remains less pronounced for the first spot. The comparison of heat flux and thermal gradient at the wall is reported in table 4.4.2 for the two longitudinal positions.

Table 4.4.2. Heat flux and thermal gradient at the wall at $x=0.1$ m and $x=0.2$ m. 10° configuration with radiative equilibrium boundary condition

10° - uncoupled	tngg	pg
$q_{w,x=0.1m}$ [W/m ²]	5.40E+04	5.74E+04
$q_{w,x=0.2m}$ [W/m ²]	4.18E+04	4.11E+04
$(\partial T/\partial n)_{w,x=0.1m}$ [K/m]	7.51E+05	7.89E+05
$(\partial T/\partial n)_{w,x=0.2m}$ [K/m]	6.18E+05	6.07E+05

The thermal gradient at the wall has the main influence on the heat flux, although there is another interesting effect due to the thermochemistry, and it shows up by examining the mass fractions distributions at the same longitudinal positions, which are displayed in figures 4.4.6 to 4.4.8.

The ideal gas simulations consider a uniform chemical composition of the gas throughout the whole flowfield, in particular in the boundary layer. On the contrary, the mixture composition in non-equilibrium computations is allowed to change, as a result of the chemical reactions. Mainly close to the model surface, the mixture composition is indeed somewhat different than at the inflow. Molecular nitrogen partially dissociates after the shock, while nitric oxide forms, see figure 4.4.6. A slight formation of molecular oxygen occurs after the shock, but this behaviour is reversed in wall direction, as depicted in figure 4.4.7 (left). Thus, the N_2 and O_2 mass fractions diminish in comparison with the inflow values, even though the percentage decrease of the former is rather low; this occurs also for atomic oxygen. On the other hand, NO and N remarkably increase, since their inflow mass fractions are very low; in particular, atomic nitrogen is up by three orders of magnitude, see figure 4.4.8 (left).


 Figure 4.4.6. N_2 (left) and NO (right) mass fraction profiles with respect to z -coordinate. Gas in thermochemical non-equilibrium with radiative equilibrium b.c. – 10° configuration.

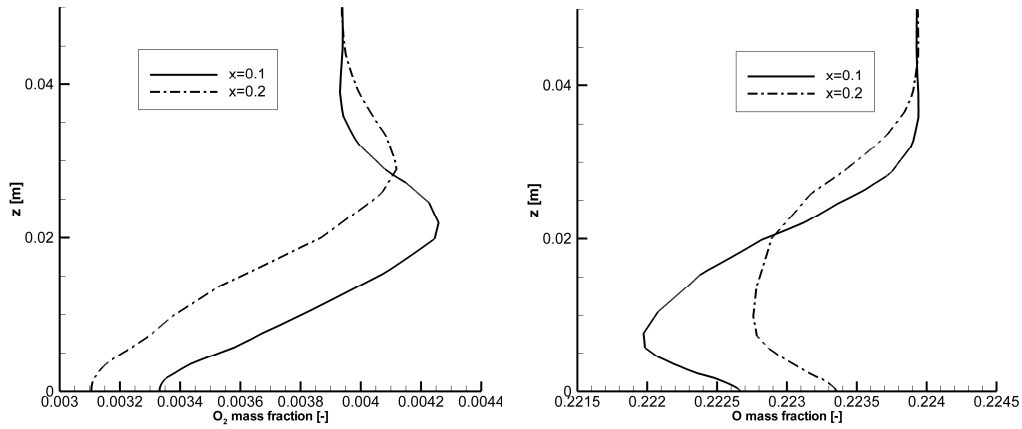


Figure 4.4.7. O_2 (left) and O (right) mass fraction profiles with respect to z -coordinate. Gas in thermochemical non-equilibrium with radiative equilibrium b.c. – 10° configuration.

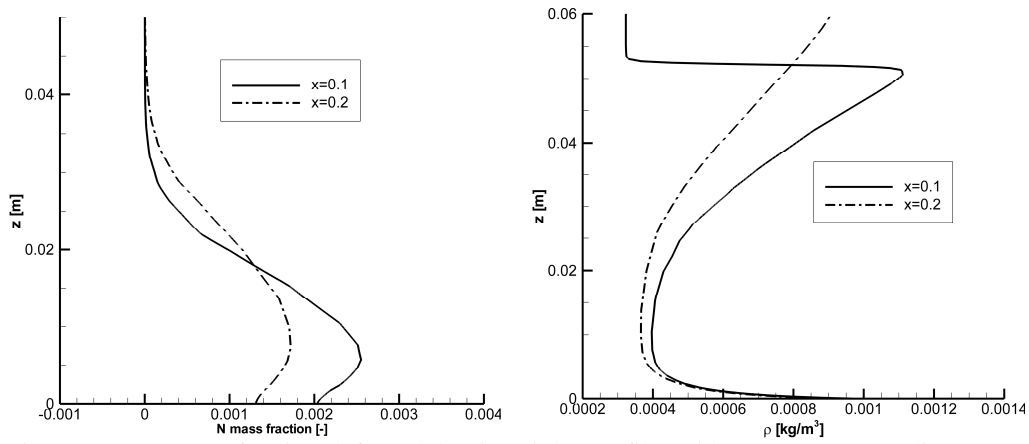


Figure 4.4.8. N mass fraction (left) and density (right) profiles with respect to z -coordinate. Gas in thermochemical non-equilibrium with radiative equilibrium b.c. – 10° configuration.

The trend in proximity of the wall is partly reversed, as a result of the density increase in this domain, which is depicted in figure 4.4.8 (right). Anyway, the variations described above still maintain at the surface.

The situation is similar downstream ($x=0.2$ m), although the quantity profiles are smoother, see again figures 4.4.6 to 4.4.8. The mass fractions at the surface are here generally closer to the inflow values, except for atomic oxygen.

The mass fractions data for both longitudinal sections are summarized in table 4.4.3, where they are also compared with the inflow amounts.

Table 4.4.3. Mass fractions at the wall at $x=0.1$ m and $x=0.2$ m in comparison with the inflow values. 10° configuration with radiative equilibrium boundary condition.

10° -uncoupled	inflow	$x=0.1$ m	$x=0.2$ m	Δ 0.2-0.1	Δ 0.1-inflow	Δ 0.2-inflow
N ₂	7.63E-01	7.59E-01	7.60E-01	0.15%	-0.47%	-0.32%
O ₂	3.93E-03	3.33E-03	3.11E-03	-7.27%	-15.23%	-20.98%
NO	9.30E-03	1.29E-02	1.20E-02	-7.36%	38.25%	28.77%
N	2.24E-06	2.04E-03	1.31E-03	-55.35%	900 times	585 times
O	2.24E-01	2.23E-01	2.23E-01	0.31%	-0.55%	-0.24%

The different temperature, density and chemical composition play together to lead to a different local heat conductivity of the gas, according to the procedure described in section 2.2. The heat conductivity at $x=0.1$ m is therefore lower than in the ideal gas case, but the variation is around 1%, as shown in table 4.4.4. Downstream the decrease is in practice negligible (approx. 0.2%).

Table 4.4.4. Heat conductivity at the wall at $x=0.1$ m and $x=0.2$ m in comparison with the perfect gas modeling. 10° configuration with radiative equilibrium boundary condition.

10° - uncoupled	tngg	pg
$\kappa_{w,x=0.1m}$ [W/(m K)]	7.19E-02	7.28E-02
$\kappa_{w,x=0.2m}$ [W/(m K)]	6.76E-02	6.77E-02

The influence of the different heat conductivity on the local heat flux is hence inferior to the effect due to the thermal gradient.

Coming back to the heat flux distribution plotted in figure 4.4.5, it is noticed that the heat flux decrease varies on the whole interface for the 20° configuration, with a maximum variation of about 15 kW/m² at the frontal edge of the coupling surface (approx. 13% less) and a minimum variation of ca. 2 kW/m² (approx. 4% less) close to the downstream end. On the other side, the thermal load at the lower angle of attack presents this “crossing” behaviour with respect to the longitudinal coordinate, with a maximal decrease upstream by ca. 13 kW/m² (approx. 14% less) and a maximal increase downstream by ca. 1 kW/m² (approx. 3% more).

The integration of the structural response has again a fundamental role in the problem under discussion. The temperature and heat flux distributions inside the model are not displayed, since they do not present significant differences from the investigations described in the preceding section, particularly from figures 4.3.6 to 4.3.8. This is common also for all subsequent investigations.

The heat conduction inside the model remarkably lowers the temperature of the surface. Once convergence after 4 inter-field iterations is reached, the temperature and heat flux distributions get very close to the ones related to the

perfect gas modeling. In the present case, the temperature mitigation is even more evident, since the temperature level for radiative equilibrium is higher. Compared to radiative equilibrium calculations, the temperature decrease in the central part of the coupling surface is again nearly uniform and it is about 70 K. On both, the front and the back surface, the decrease reaches almost 300 K thanks to the heat conduction effects.

Furthermore, it is confirmed that the heat fluxes are fairly well predicted by the radiative equilibrium solution in the domains where the conduction effects are low. Apart from the model extremities, where the temperature drops occur and the load undergoes variations up to 40 kW/m² (approx. 25%), the increase amounts to ca. 1 kW/m² (approx. 1-2%).

Tables 4.4.5 and 4.4.6 summarize the convergence of the thermal quantities with respect to the inter-field iteration.

Table 4.4.5. Convergence of the thermal quantities. Thermochemical non-equilibrium. $\alpha=10^\circ$.

Iteration	ΔT_{\max}	$\Delta T_{x=0.14\text{m}}$	Δq_{\max}	$\Delta q_{x=0.14\text{m}}$
uncoupled - 1	-2.70E+02	-6.45E+01	3.19E+04	6.18E+02
1 - 2	-7.89E+01	-3.11E+00	9.52E+03	1.99E+01
2 - 3	2.06E+01	1.20E-01	2.48E+03	-9.59E+00
3 - 4	-5.27E+00	-6.23E-03	-2.92E+02	-2.89E-01

Table 4.4.6. Convergence of the thermal quantities. Thermochemical non-equilibrium. $\alpha=20^\circ$.

Iteration	ΔT_{\max}	$\Delta T_{x=0.14\text{m}}$	Δq_{\max}	$\Delta q_{x=0.14\text{m}}$
uncoupled - 1	-2.87E+02	-6.93E+01	4.19E+04	1.13E+03
1 - 2	-8.45E+01	-4.04E+00	1.26E+04	6.14E+01
2 - 3	2.32E+01	2.30E-01	-3.39E+03	-5.51E+00
3 - 4	-7.09E+00	-1.65E-02	1.02E+03	-3.85E+00

The temperature and heat flux trends on the surface are rather similar to the converged coupled perfect gas solution, as displayed in figures 4.4.9 and 4.4.10. In virtue of the structural influence, the temperature peaks are notably smoothed and a considerable part of the thermal load is transferred inside the model. The heat conduction effects are still noteworthy on the rear, where the temperature reduction is evident and consequently the heat flux presents even a reversal of its gradient.

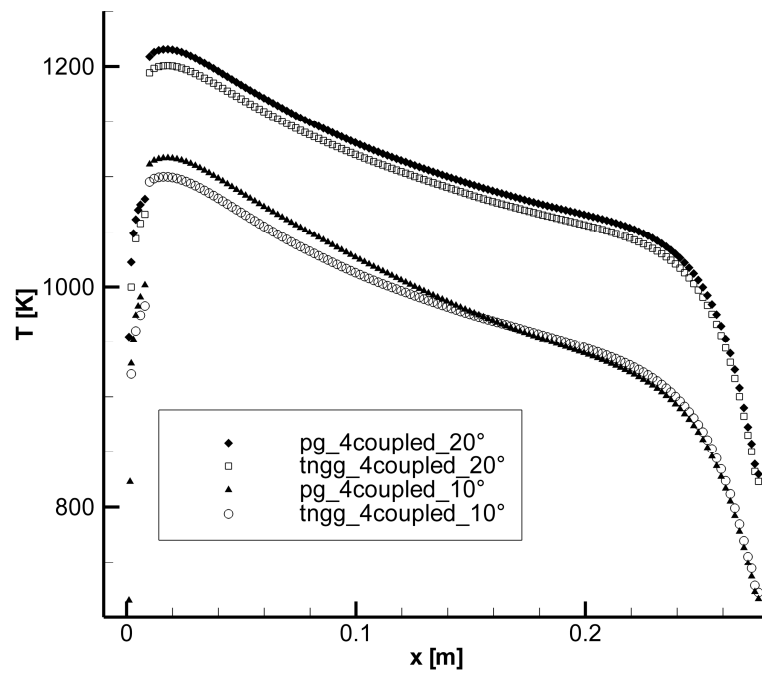


Figure 4.4.9. Temperature distribution on the coupling surface. Gas in thermochemical non-equilibrium with fluid-structure interaction and comparison with perfect gas modeling.

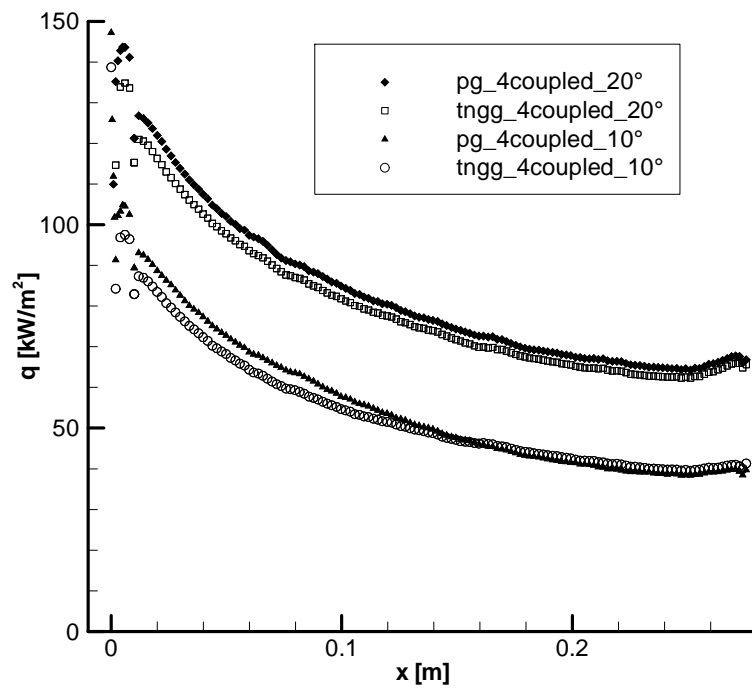


Figure 4.4.10. Heat flux distribution on the coupling surface. Gas in thermochemical non-equilibrium with fluid-structure interaction and comparison with perfect gas modeling.

It is important to quantify the influence of the different flow modeling, once the coupling is taken into account. As highlighted so far, the thermal response of the structure has a significant impact, since it attenuates the disagreement in the results between the two models. The temperature in case of thermochemical modeling is generally reduced in comparison with the ideal gas coupled simulations, with a maximal decrease on the front by about 19 and 24 K (corresponding to a decrease of ca. 2%) for the 10° and 20° configuration, respectively. Besides this domain, the set-up at higher angle of attack shows a difference of ca. 10 K (approx. 1% less) in the middle and a minimal reduction of ca. 6 K (approx. 0.8% less) on the back. It is confirmed how influential the structure in the whole problem is: aside from the gas modeling, the results of the coupling are almost the same, especially where the structural effects are predominant. An analogous behaviour for the same angle of attack is shown by the surface load: besides the forebody drop of ca. 9 kW/m² (approx. 6% less), the decrease settles down to ca. 3 kW/m² (approx. 4% less), with a minimal reduction on the rear which amounts to about 1 kW/m² (approx. 1.5% less). Anyway, it is necessary to underline that the thermochemistry effects at the surface previously described for the radiative equilibrium case still remain in the coupled solution. They are rather evident for the lower angle of attack configuration, but they help to explain also why the temperature difference along the longitudinal coordinate for the 20° case diminishes. Considering again two perpendicular sections at $x=0.1$ m and $x=0.2$ m, table 4.4.7 points out that the thermal gradient at the wall for the latter position accounting for thermochemical modeling is more accentuated than for the ideal gas case, although the situation is inverted for the former spot.

Table 4.4.7. Heat flux and thermal gradient at the wall at $x=0.1$ m and $x=0.2$ m. 10° configuration with fluid-structure interaction.

10° - 4coupled	tngg	pg
$q_{w,x=0.1m}$ [W/m ²]	5.45E+04	5.76E+04
$q_{w,x=0.2m}$ [W/m ²]	4.24E+04	4.14E+04
$(\partial T/\partial n)_{w,x=0.1m}$ [K/m]	6.17E+05	6.46E+05
$(\partial T/\partial n)_{w,x=0.2m}$ [K/m]	6.60E+05	6.21E+05

The heat flow distributions keep thus this “crossing” trend for the 10° configuration, with a load decrease on the front by about 6 kW/m² (approx. 6% less) and an opposite increase on the back by about 1.5 kW/m² (approx. 4% more). Furthermore, the temperature evolution itself assumes a similar behaviour, with the mentioned drop of 19 K at the forebody and a growth up to 7 K (approx. 1% more) on the rear. It can be noticed that the radiative equilibrium solution presents an analogous trend, i.e. the temperature decrease

for the thermochemical modeling along the surface is less than for the perfect gas case.

The mass fraction distribution agrees with the radiative equilibrium formulation, with just small differences in the values, see table 4.4.8. Only atomic oxygen shows a different behaviour at the more downstream position, but this variation is negligible if compared with the nominal values.

Table 4.4.8. Mass fractions at the wall at $x=0.1$ m and $x=0.2$ m in comparison with the inflow values. 10° configuration with fluid-structure interaction.

10° -4coupled	inflow	$x=0.1$ m	$x=0.2$ m	Δ 0.2-0.1	Δ 0.1-inflow	Δ 0.2-inflow
N ₂	7.63E-01	7.59E-01	7.62E-01	0.42%	-0.54%	-0.12%
O ₂	3.93E-03	3.54E-03	2.83E-03	-25.23%	-9.80%	-27.97%
NO	9.30E-03	1.32E-02	1.10E-02	-20.32%	41.75%	17.81%
N	2.24E-06	2.45E-03	3.73E-04	7 times less	1095 times	165 times
O	2.24E-01	2.22E-01	2.24E-01	0.81%	-0.73%	0.08%

The heat conduction remains inferior to the ideal gas one, although in this case the higher difference is at $x=0.2$ m, as reported in table 4.4.9. However, it is confirmed that the heat conduction does not represent the most important impact on the local thermal load.

Table 4.4.9. Heat conductivity at the wall at $x=0.1$ m and $x=0.2$ m in comparison with the perfect gas modeling. 10° configuration with fluid-structure interaction.

10° - 4coupled	tngg	pg	$\Delta\kappa$ tngg-pg
$\kappa_{w,x=0.1m}$ [W/(m K)]	8.83E-02	8.92E-02	-0.92%
$\kappa_{w,x=0.2m}$ [W/(m K)]	6.43E-02	6.66E-02	-3.47%

The coupled solution reflects therefore what with the radiative equilibrium boundary condition occurs, although the structural response substantially influences the problem and remarkably reduces the differences.

In conclusion, it is proved that the impact of the thermochemical modeling on the coupled solution is minimal, in particular on the horizontal plate.

4.5 Divergent flow

Up to now, the inflow conditions for the model flow have been assumed as uniform. Strictly speaking, the flow in the L3K test chamber is, however, slightly divergent, owing to the used conical nozzle. In order to understand which influence the divergent flow downstream of the nozzle on the surface quantities can have, the inflow conditions are here taken from a nozzle flow

solution. The flow quantities are then linearly interpolated on the boundary of the usual flow domain for the numerical computations, namely on the inflow and on the far field. They constitute thus the boundary condition for the flow solution, and the interpolation procedure is repeated for each adaptation step when calculating the startup solution.

Similarly to the previous section, only the 10° and 20° configurations are computed.

The flow in the considered L3K facility components is simulated in the absence of the model. The flow is treated as steady and axisymmetric and it is assumed to be laminar [93]. After the investigations by Mack [31], it can be assessed that at the considered flow conditions the shear layer coming off from the nozzle evolves nearly parallel to the symmetry axis and that no characteristic can strike the region, where the model surface will be positioned. The total enthalpy remains practically unchanged in the flow domain, which will subsequently involve the model.

The reservoir conditions are the same as reported in section 4.3. The nozzle exit diameter is set to 300 mm. The facility walls are modeled at a uniform temperature of 500 K, since they are water-cooled. The facility internal fluid domain is discretized by means of a hybrid mesh, see figure 4.5.1: the region in proximity of the wall is discretized through a structured mesh which amounts to ca. $9 \cdot 10^3$ elements in all, distributed on 30 layers in normal direction, while the rest is discretized with an unstructured mesh composed of ca. $2.5 \cdot 10^4$ elements.

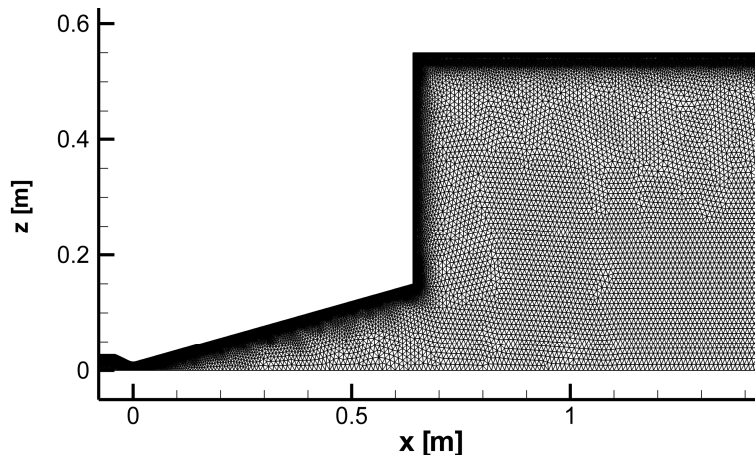


Figure 4.5.1. Considered flow domain inside the L3K facility and its discretization.

The gas is modeled for efficiency reasons at chemical non-equilibrium and thermodynamic equilibrium, since in the present case the aim is the investigation of the effects of the divergent flow and not directly concerning the

complete non-equilibrium thermochemistry inside the facility. The influence on the surface quantities of the thermochemical modeling of the flowfield surrounding the model has been already discussed in section 4.4, while the non-equilibrium thermochemistry in the nozzle flow will be treated in the next section.

Figure 4.5.2 displays the Mach number distribution taken from the solution of the facility flow. It is possible to notice the continuous expansion along the nozzle and the further expansion at the nozzle exit due to the slightly lower pressure in the test chamber background in comparison with the core flow.

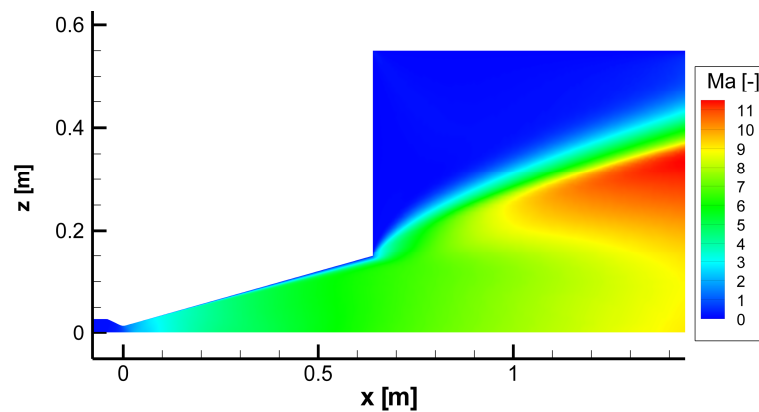


Figure 4.5.2. Mach number distribution in the solved domain. Gas in chemical non-equilibrium and thermodynamic equilibrium.

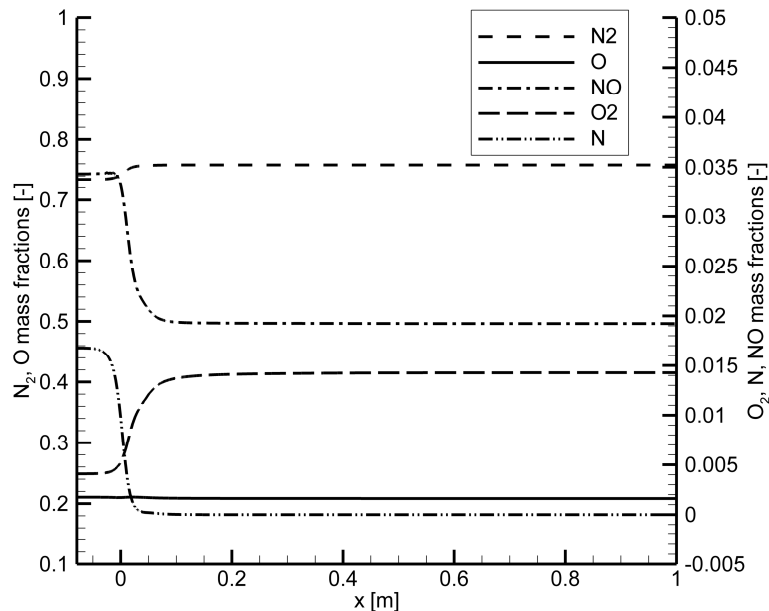


Figure 4.5.3. Mass fractions distribution in the facility along the central streamline. Gas in chemical non-equilibrium and thermodynamic equilibrium.

Moreover, figure 4.5.3 offers a confirmation that the chemistry “freezes” downstream of the nozzle throat and that the mass fractions keep practically unchanged for the rest of the fluid domain.

Once the solution of this flow is available, the properties at the inflow boundary of the model fluid domain can be obtained. For that, the nozzle flow is rotated by the desired angle of attack and the model is introduced at a distance of 939 mm from the nozzle throat section (300 mm from the nozzle exit). This procedure can easily be understood considering figure 4.5.4. The flow quantities are then interpolated on the contour of the model grid, and the solution of the flowfield surrounding the model can start.

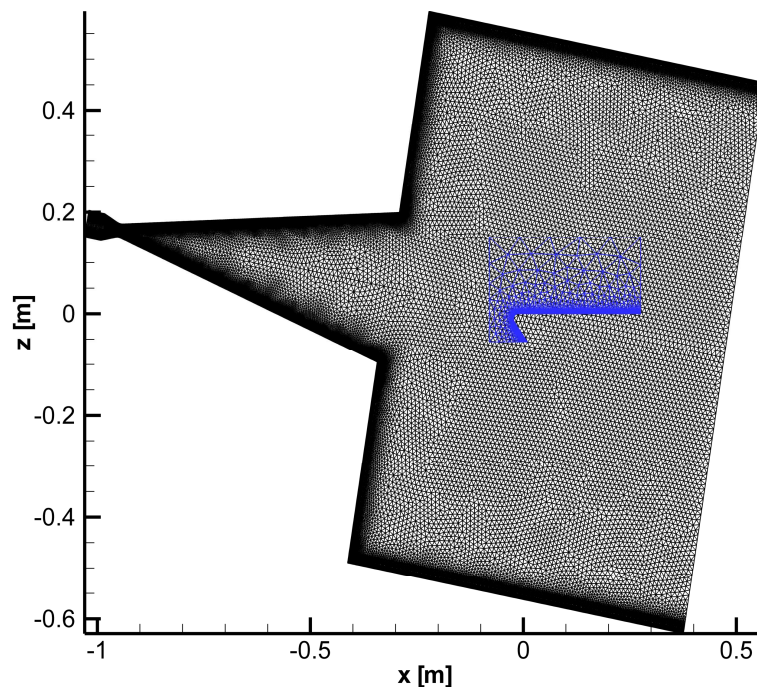


Figure 4.5.4. Facility mesh (black) and model mesh (blue) set up for first interpolation – 10° configuration.

The subsequent procedure is very similar to the one conducted for the perfect gas computations. For efficiency reasons the gas is then modeled again as ideal, since the differences on the surface thermal quantities with thermochemical non-equilibrium modeling inside the chamber are shown to be not significant. The perfect gas properties must be appropriate and are referred to the inflow conditions in front of the nose, which are reported in the table 4.5.1.

Table 4.5.1. Inflow conditions and perfect gas properties for divergent flow referred to the symmetry axis at $x=0.939$ m.

Ma_∞	7.55
T_∞ [K]	490.64
p_∞ [Pa]	52.43
ρ_∞ [kg/m ³]	$3.122 \cdot 10^{-4}$
V_∞ [m/s]	3724
α (N ₂)	0.758
α (O ₂)	0.0143
α (NO)	0.0192
α (N)	$4.63 \cdot 10^{-9}$
α (O)	0.208
R [J/(kg K)]	342.3
γ	1.449

The remaining quantities have the same values as in section 4.3. The majority of the quantities above do not remarkably vary in comparison with the results obtained by Mack [31], but it is noticeable that the inflow reference temperature is somewhat higher. Although the temperature on the streamlines approaching the model keeps decreasing as far as they undergo the shock, this represents an important effect on the following results. The variations with the reference values are likely to be due to the use of a newer version of the TAU code, which has been developed after the work [31] was completed.

Once the iteration cycle for the startup solution with radiative equilibrium boundary condition has converged, it comes out that, as a result of the stream divergence, the flowfield is a little different, see figures 4.5.5 and 4.5.6. The shock line in the flow domain in front of the nose and base regions is closer to the body, whereas above the model it is less attached. Moreover, the Mach number in the diverging stream reaches higher values.

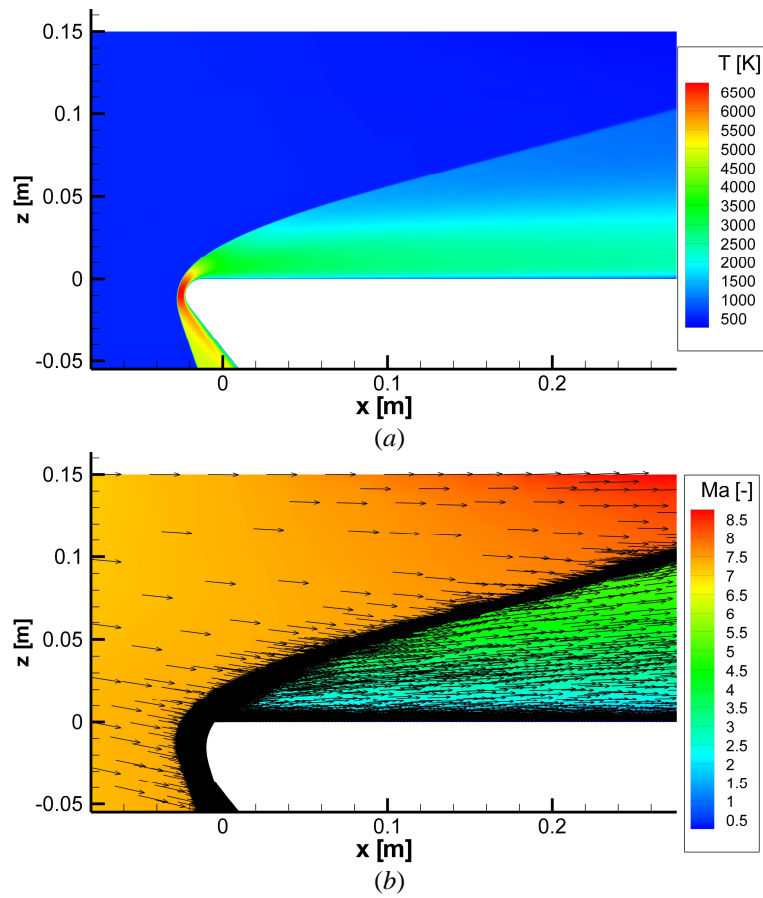


Figure 4.5.5. Distribution of temperature (a) and Mach number together with the velocity vectors (b) in the flowfield. Divergent flow. $\alpha=10^\circ$.

In virtue of the diverse flow conditions, the maximal field temperature is around 6760 K, i.e. more than 100 K higher than in the reference computations of section 4.3. The thermal quantities at the coupling surface differ, however, only slightly.

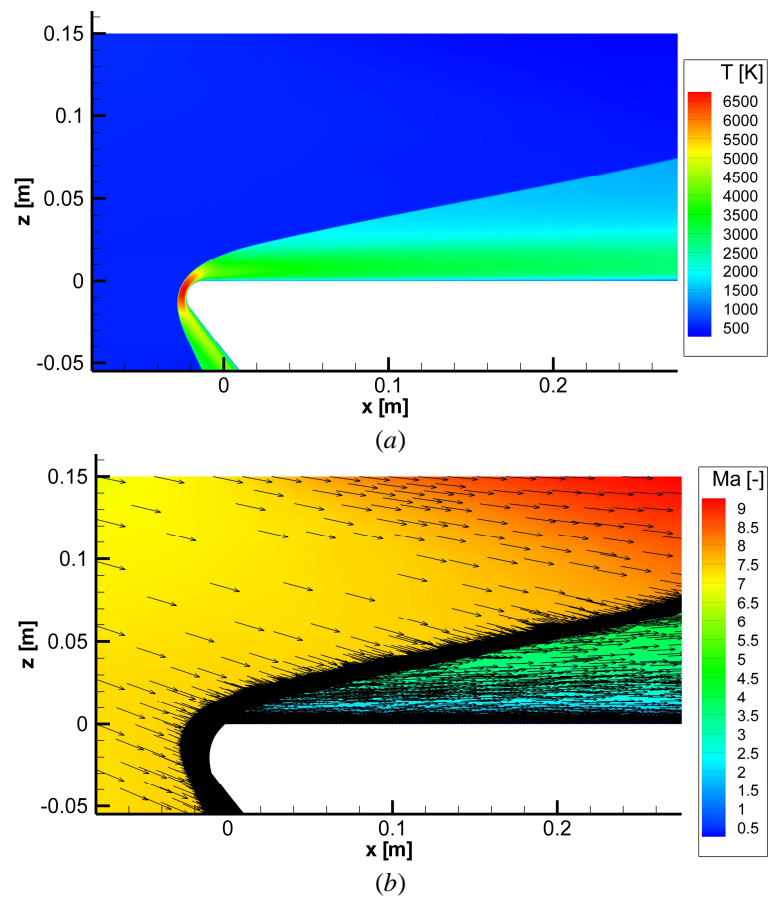


Figure 4.5.6. Distribution of temperature (a) and Mach number together with the velocity vectors (b) in the flowfield. Divergent flow. $\alpha=20^\circ$.

At the inferior angle of attack, the surface temperature on the plates is approx. 20-25 K lower than for the uniform stream case, but in closer proximity to the shock the situation is reversed and the temperature increases by about 10 K, as shown in figure 4.5.7. This is more marked for the 20° configuration, where the surface temperature is ca. 10 K higher for a considerable part of the interface, before the trend inverts at $x \sim 60$ mm and temperatures are reached which are even 30 K lower than in the uniform stream case.

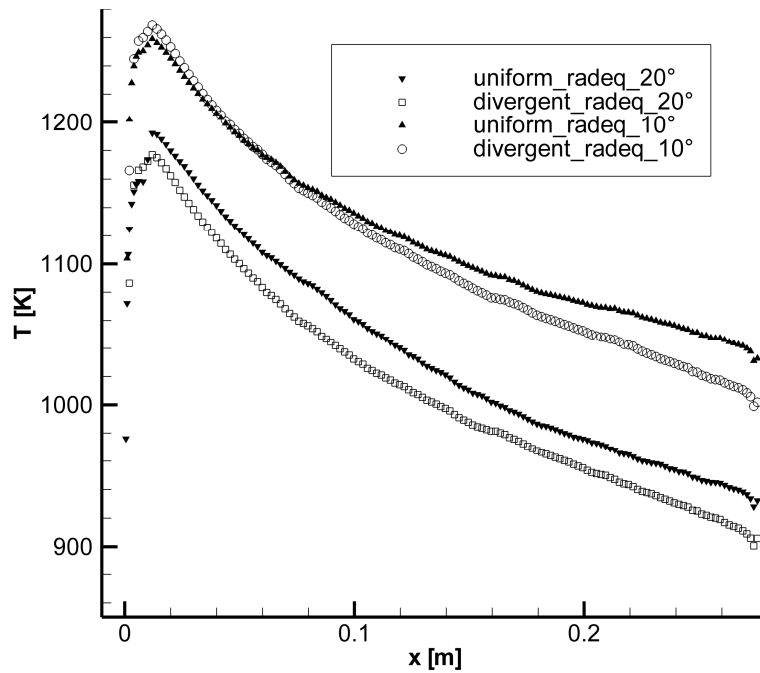


Figure 4.5.7. Temperature distribution on the coupling surface. Divergent flow with radiative equilibrium b.c. and comparison with uniform flow.

The temperature in the fluid domain close to the body is in effect higher on the fore region, but downstream it evolves decreasing, as plotted in figure 4.5.8.

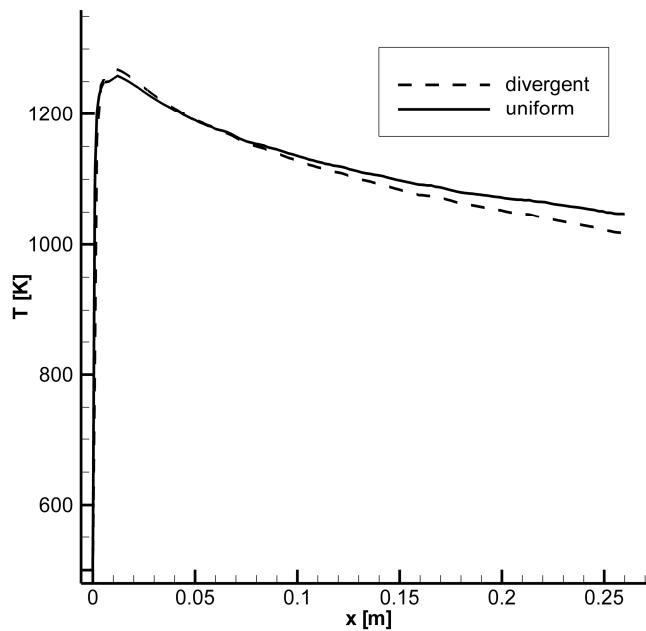


Figure 4.5.8. Temperature distribution along the flow domain in correspondence to $z=0.001$ m. Comparison between divergent and uniform stream. 20° configuration.

The thermal load keeps in pace with the behaviour of the surface temperature, see figure 4.5.9. The difference is about 10 kW/m^2 on the front for both configurations and decreases downwards, although at $x > 60 \text{ mm}$ there is almost no difference for the lower angle of attack, while the heat flux decrease for the 20° configuration is such that on the back end it amounts to ca. 10 kW/m^2 less than with uniform flow.

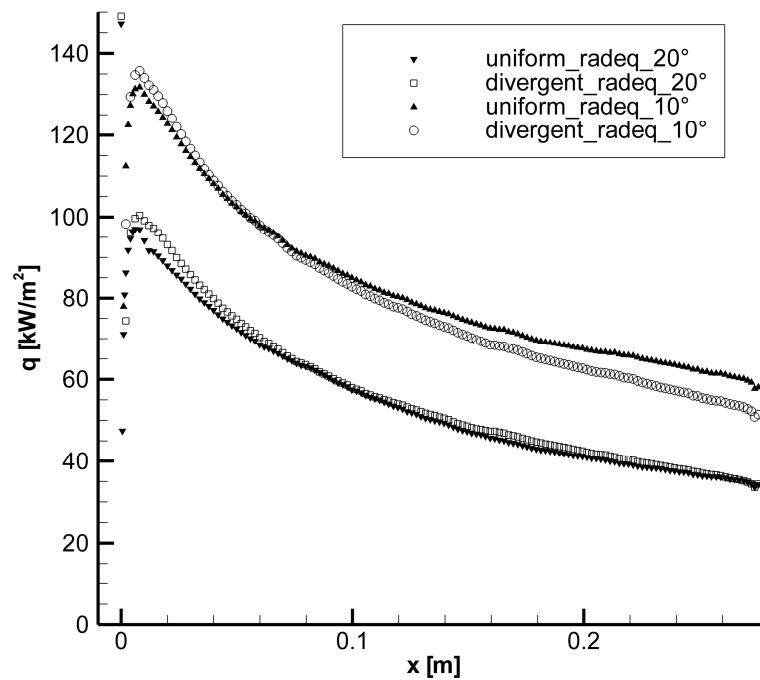


Figure 4.5.9. Heat flux distribution on the coupling surface. Divergent flow with radiative equilibrium b.c. and comparison with uniform flow.

After the coupling is performed, the effect of the structure is again noteworthy. The temperature mitigation on the extremes reaches $200\text{-}220 \text{ K}$, with a consequent increase of the heat flux up to $25\text{-}35 \text{ kW/m}^2$. The thermal quantities are, however, very good predicted by the radiative equilibrium solution on the central region and the convergence is rather fast, as shown in tables 4.5.2 and 4.5.3.

Table 4.5.2. Convergence of the thermal quantities. Divergent flow. $\alpha=10^\circ$.

Iteration	ΔT_{\max}	$\Delta T_{x=0.14\text{m}}$	Δq_{\max}	$\Delta q_{x=0.14\text{m}}$
uncoupled - 1	-2.04E+02	-6.38E+00	2.51E+04	2.11E+01
1 - 2	-5.70E+01	-9.95E-02	7.62E+03	5.83E+00
2 - 3	1.54E+01	3.00E-02	-2.09E+03	-2.91E+00
3 - 4	-4.24E+00	-1.00E-02	5.74E+02	1.64E-01

Table 4.5.3. Convergence of the thermal quantities. Divergent flow. $\alpha=20^\circ$.

Iteration	ΔT_{\max}	$\Delta T_{x=0.14\text{m}}$	Δq_{\max}	$\Delta q_{x=0.14\text{m}}$
uncoupled - 1	-2.17E+02	-5.67E+00	3.35E+04	5.05E+01
1 - 2	-6.33E+01	-1.20E-01	1.03E+04	9.15E+00
2 - 3	1.68E+01	6.35E-02	-2.67E+03	-4.98E+00
3 - 4	-3.19E+00	-3.34E-02	6.99E+02	5.20E-01

The structural response determines also a reduction of the differences with respect to the coupled uniform stream computations and the trends get in general very close, even though the behaviour mentioned above remains, see figures 4.5.10 and 4.5.11. The temperature and heat flux for the higher angle of attack evolve from an increase on the fore surface by about 8 K (ca. 0.7% more than for perfect gas modeling) and 4.5 kW/m² (approx. 5% more) to a decrease on the rear by about 30 K (ca. 3% less) and 8 kW/m² (approx. 10% less), while the difference for the 10° configuration varies from ca. 15 K (corresponding to ca. 1.5% more) to around -1.5 K (ca. 0.15% less) and from about 6 kW/m² (approx. 11% more) to ca. -800 W/m² (approx. 1% less) for the surface temperature and thermal load, respectively.

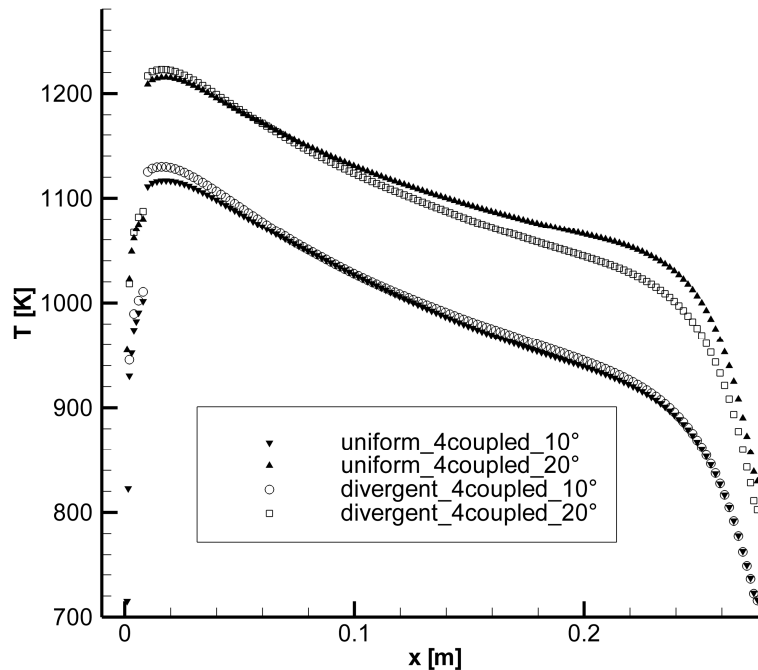


Figure 4.5.10. Temperature distribution on the coupling surface. Divergent flow with fluid-structure interaction and comparison with uniform flow.

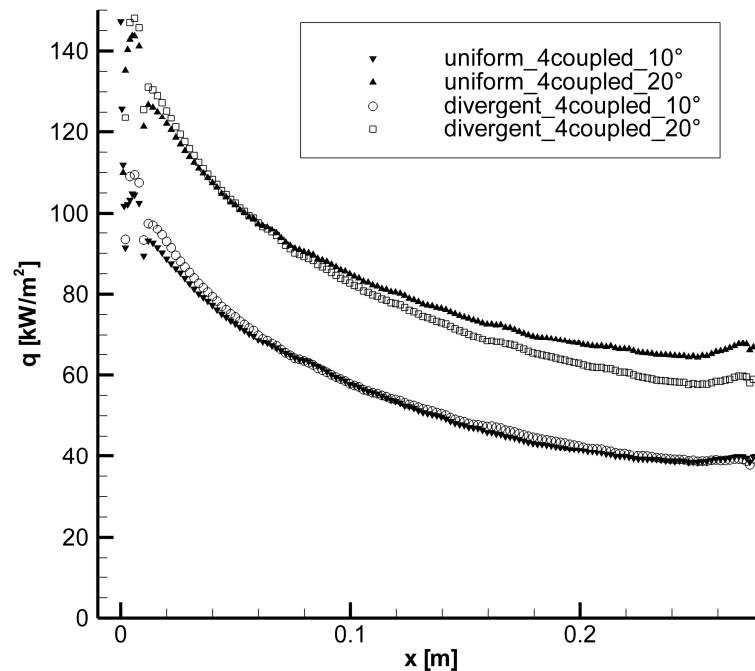


Figure 4.5.11. Heat flux distribution on the coupling surface. Divergent flow with fluid-structure interaction and comparison with uniform flow.

The thermal quantities at the surface are thus very close to the results of the simulations performed with uniform stream.

4.6 Nozzle flow in thermochemical non-equilibrium

The computation of the nozzle together with the test chamber offers another interesting possibility if coupled with thermochemical non-equilibrium conditions. The facility flow is simulated in the absence of the model similarly to section 4.5, but this time accounting for thermochemical non-equilibrium according with the same modeling as in section 4.4.

The distributions of the mass fractions of the gas mixture components and of the vibrational temperature of molecular nitrogen have already been shown in section 3.1 (figures 3.1.2 and 3.1.3). Figure 4.6.1 displays the Mach number distribution in the solved facility domain. Comparing the plot with figure 4.5.2, it is noticed that the values are in general higher than in the simulations of the preceding section, as a result of the gas modeling at thermodynamic non-equilibrium. Because of the freezing of the vibrational energy, the temperature along the streamlines decreases indeed more markedly than with the thermodynamic equilibrium formulation. Therefore, the speed of sound is inferior and the Mach number consequently reaches higher values, since the stream velocity is in effect comparable. This remark is confirmed by the data contained in table 4.6.1.

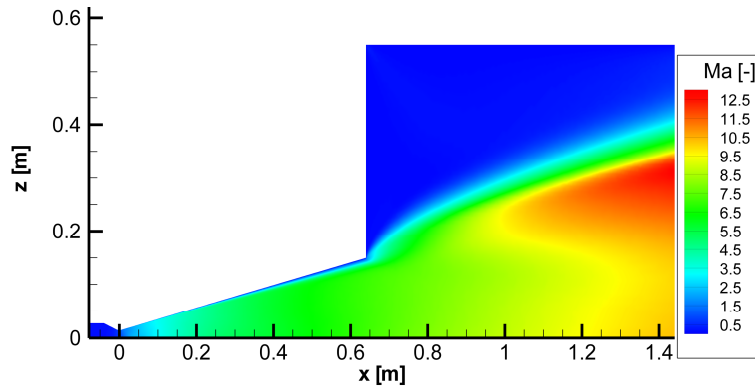


Figure 4.6.1. Mach number distribution in the solved field. Gas in thermochemical non-equilibrium.

Once this solution is available, the flow quantities are interpolated on the grid contour for the subsequent problem involving the model. Since it has been proved that the divergent flow and the thermochemical modeling inside the test chamber have not a significant impact on the surface quantities, the flow is then simulated for efficiency reasons in the usual domain as uniform and as an ideal gas, but with adapted perfect gas properties and inflow conditions. These are hence obtained by the interpolation on the inflow contour in front of the model nose and are summarized in table 4.6.1, which presents also a comparison with the conditions of the simulations with nozzle flow in thermodynamic equilibrium and of the reference simulations of section 4.3. The abbreviations “tnggf” and “tggf” stay for nozzle flow in thermochemical non-equilibrium and chemical non-equilibrium, respectively, while “pg” for the reference data [31].

Table 4.6.1. Inflow conditions and perfect gas properties referred to the symmetry axis at $x=0.939$ m. Nozzle flow simulated in thermochemical non-equilibrium and comparison with data of sections 4.3 and 4.5.

	tnggf	tggf	pg
Ma_{∞}	8.55	7.55	7.62
T_{∞} [K]	354.16	490.64	463.7
p_{∞} [Pa]	40.65	52.43	51.95
ρ_{∞} [kg/m ³]	$3.357 \cdot 10^{-4}$	$3.122 \cdot 10^{-4}$	$3.320 \cdot 10^{-4}$
V_{∞} [m/s]	3592	3724	3678
$\alpha(\text{N}_2)$	0.756	0.758	0.763
$\alpha(\text{O}_2)$	0.0128	0.0143	$3.93 \cdot 10^{-3}$
$\alpha(\text{NO})$	0.0249	0.0192	$9.30 \cdot 10^{-3}$
$\alpha(\text{N})$	$2.17 \cdot 10^{-9}$	$4.63 \cdot 10^{-9}$	$2.24 \cdot 10^{-6}$
$\alpha(\text{O})$	0.207	0.208	0.224
R [J/(kg K)]	342.0	342.3	346.0
γ	1.457	1.449	1.462

Compared to the reference values [31], the inflow Mach number is thus almost one unity greater, the inflow temperature more than 100 K inferior, the inflow pressure slightly higher and the inflow velocity ca. 100 m/s lower. Moreover, the mass fractions of the particles composing the mixture are different; in particular, atomic oxygen decreases.

The ideal gas properties are consequently different. Similar considerations can be drawn when comparing the values with the results of the nozzle flow in thermodynamic equilibrium. It is important to remark the significant relative decrease of the temperature, which determines the higher Mach number, whereas the other quantities do not undergo pronounced variations.

The quantities not listed in the table remain as in section 4.3.

All three configurations (10° , 20° and 30° angles of attack) are computed in this investigation.

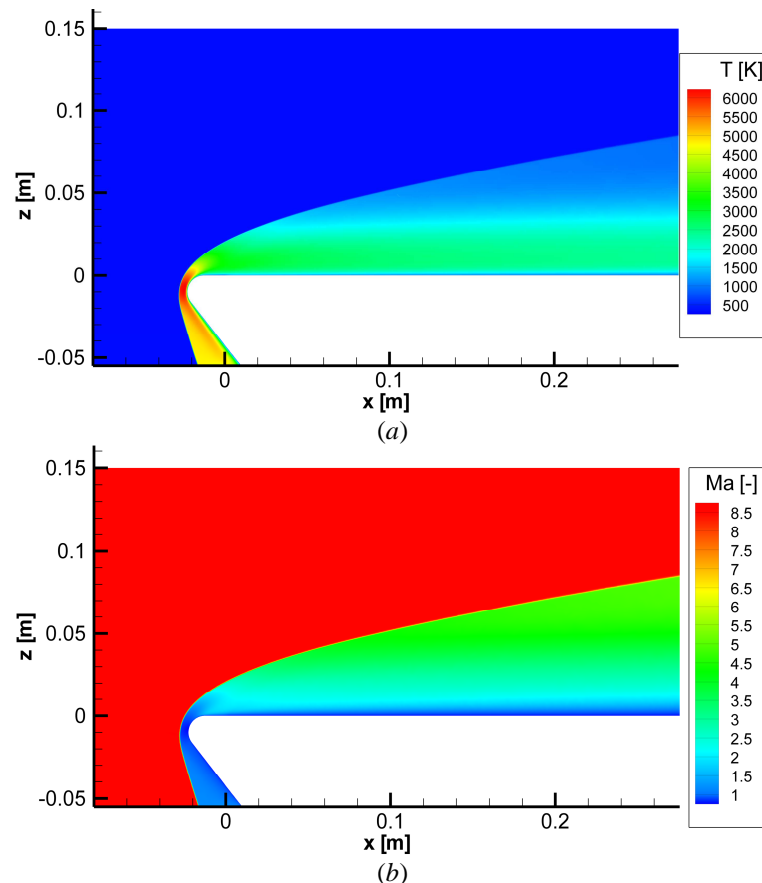


Figure 4.6.2. Distribution of temperature (a) and Mach number (b) in the flowfield. Nozzle flow in thermochemical non-equilibrium. $\alpha=10^\circ$.

Because of the unlike stream conditions, the converged startup solution with radiative equilibrium boundary condition presents a general reduction of the thermal load on the surface in comparison with the perfect gas investigations. As depicted in figures 4.6.2 to 4.6.4, the shock line is closer to the body, although the shock shape remains similar. The temperature level in the fluid domain is lower than for the simulations of section 4.3. The maximal field temperature is about 6220 K, approx. 400 K less than in the reference investigations, in accordance with the lower inflow temperature.

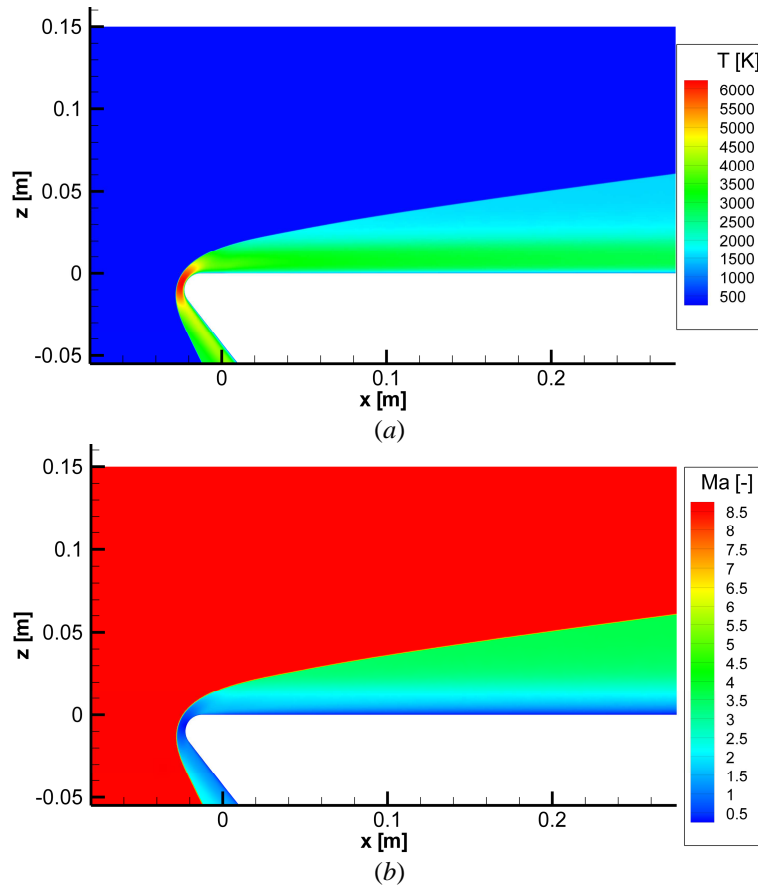


Figure 4.6.3. Distribution of temperature (a) and Mach number (b) in the flowfield. Nozzle flow in thermochemical non-equilibrium. $\alpha=20^\circ$.

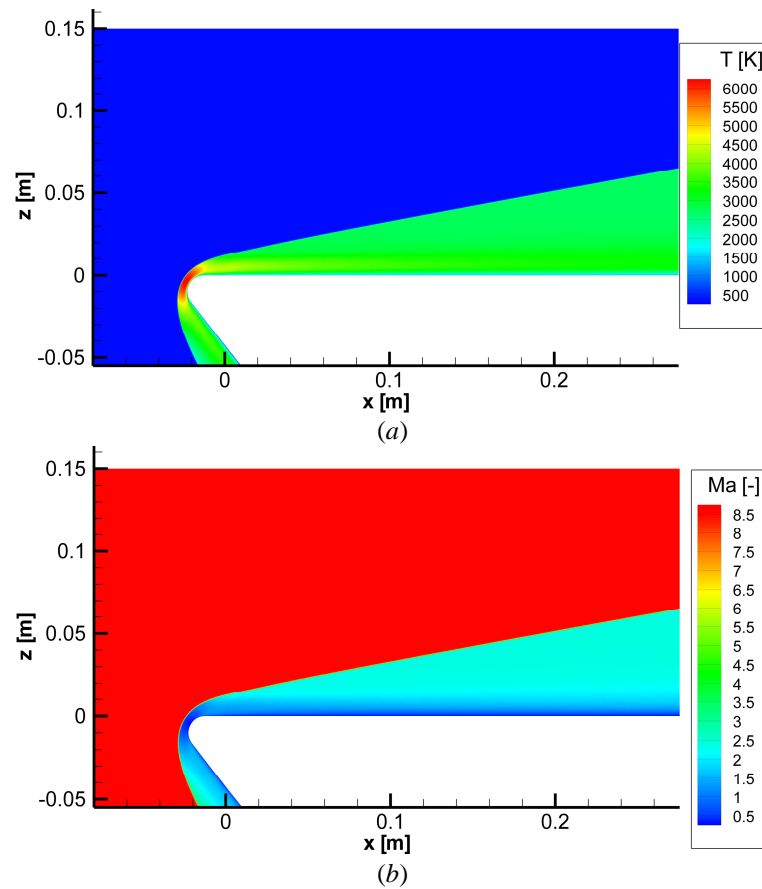


Figure 4.6.4. Distribution of temperature (a) and Mach number (b) in the flowfield. Nozzle flow in thermochemical non-equilibrium. $\alpha=30^\circ$.

The temperature at the surface reflects this behaviour, see figure 4.6.5. There is a difference of several degrees on the whole interface between the present computations and the ones conducted in section 4.3, with a maximal decrease on the front and a lower decrease on the rear for all configurations. The reduction is more accentuated for the lower angle of attack, going from approx. 50 K on the fore surface to approx. 30 K on the back, while these amount for both other two configurations to ca. 30 K and ca. 20 K.

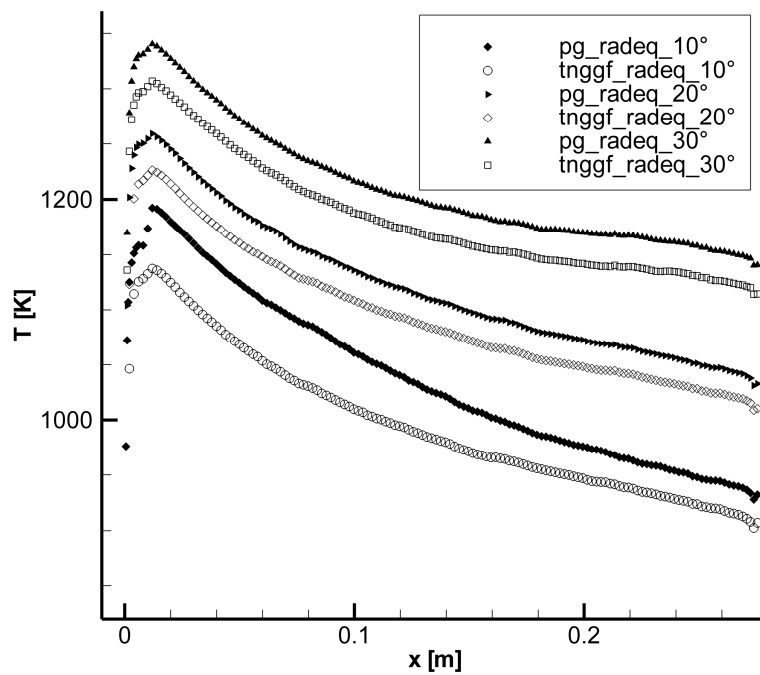


Figure 4.6.5. Temperature distribution on the coupling surface. Nozzle flow in thermochemical non-equilibrium with radiative equilibrium b.c. and comparison with perfect gas modeling.

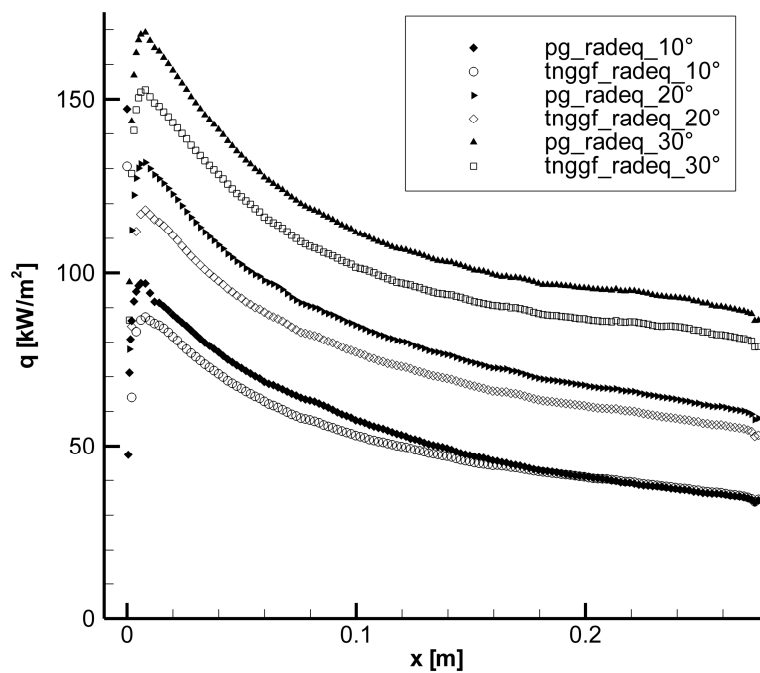


Figure 4.6.6. Heat flux distribution on the coupling surface. Nozzle flow in thermochemical non-equilibrium with radiative equilibrium b.c. and comparison with perfect gas modeling.

As shown in figure 4.6.6, the heat flux trend for these two configurations is very similar. The decrease evolves from about 15 and 12 kW/m² on the front to ca. 8 and 5 kW/m² on the rear for the 30° and 20° angles of attack, respectively. On the other side, the 10° configuration is characterized by a heat flux difference of around 7 kW/m² on the fore surface which diminishes along with the longitudinal coordinate, such that from $x \sim 190$ mm the results are practically coincident.

After integration of the structural response, the surface temperature is lowered once again. Thanks to the heat conduction effects, the temperature reduction in comparison with the startup solution can even reach 235 K (on the fore surface for the 30° angle of attack), although the most important influence is still limited on the external regions. On the central part the mitigation amounts to ca. 5-6 K. Analogously, the thermal load is principally increased on the external domains. The maximal growth arises on the front and reaches even 70 kW/m² (30° configuration), but on the centre the difference with the radiative equilibrium solution is nearly negligible, in virtue of the low conduction effects in this region.

The convergence of the thermal quantities is reported in tables 4.6.2 to 4.6.4 and is obtained once again after 4 coupling iterations.

Table 4.6.2. Convergence of the thermal quantities. Nozzle flow in thermochemical non-equilibrium. $\alpha=10^\circ$.

Iteration	ΔT_{\max}	$\Delta T_{x=0.14\text{m}}$	Δq_{\max}	$\Delta q_{x=0.14\text{m}}$
uncoupled - 1	-2.06E+02	-6.20E+00	2.31E+04	1.78E+01
1 - 2	-5.75E+01	-3.00E-02	7.35E+03	4.17E+00
2 - 3	1.66E+01	1.35E-02	-2.13E+03	-2.90E+00
3 - 4	-4.72E+00	-6.53E-03	5.92E+02	8.00E-01

Table 4.6.3. Convergence of the thermal quantities. Nozzle flow in thermochemical non-equilibrium. $\alpha=20^\circ$.

Iteration	ΔT_{\max}	$\Delta T_{x=0.14\text{m}}$	Δq_{\max}	$\Delta q_{x=0.14\text{m}}$
uncoupled - 1	-2.20E+02	-6.14E+00	3.09E+04	9.11E+01
1 - 2	-6.44E+01	-1.54E-01	1.02E+04	2.39E+00
2 - 3	2.02E+01	1.35E-02	-3.16E+03	-1.18E+00
3 - 4	-7.37E+00	-3.54E-03	1.13E+03	-3.98E-01

Table 4.6.4. Convergence of the thermal quantities. Nozzle flow in thermochemical non-equilibrium. $\alpha=30^\circ$.

Iteration	ΔT_{\max}	$\Delta T_{x=0.14\text{m}}$	Δq_{\max}	$\Delta q_{x=0.14\text{m}}$
uncoupled - 1	-2.34E+02	-5.26E+00	5.50E+04	-3.32E+01
1 - 2	-9.57E+01	2.70E-01	2.31E+04	-1.84E+01
2 - 3	3.55E+01	-1.99E-02	-8.32E+03	5.71E-01
3 - 4	1.35E+01	5.98E-03	3.07E+03	-3.09E-01

The differences with the reference computations previously pointed out generally persist also after the coupling, as plotted in figure 4.6.7. The coupled solutions for the 20° and 30° configurations show a maximal difference from the coupled ideal gas results of about 35 K (corresponding to ca. 3% less) on the fore surface, which diminishes along with the x -coordinate down to approx. 25 and 20 K for the higher and middle angles of attack, respectively, which correspond to a decrease by ca. 2% and 1.5%. The solution for the lower angle of attack agrees with the behaviour of the radiative equilibrium results, but the differences are mostly mitigated by the structural influence, so that they in practice disappear from $x \sim 210$ mm, even though they are still remarkable on the frontal domain, where the temperature difference amounts to approx. 25 K (around 2.5% less).

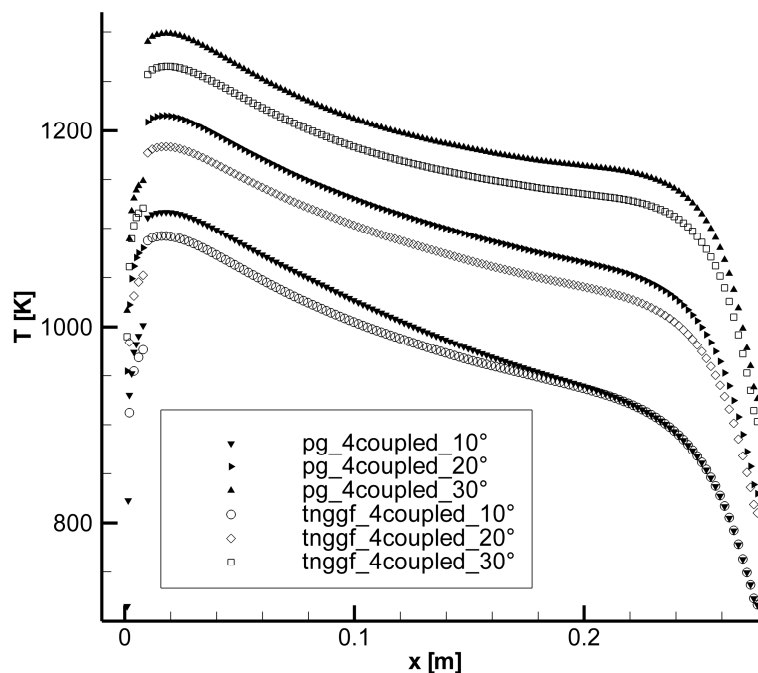


Figure 4.6.7. Temperature distribution on the coupling surface. Nozzle flow in thermochemical non-equilibrium with fluid-structure interaction and comparison with perfect gas modeling.

The heat flux distributions keep in pace with the temperature ones, see figure 4.6.8. The load increase in comparison with the coupled reference results is inferior and adds up to 20, 15 and 8 kW/m² on the fore surface for the 30°, 20° and 10° configurations, respectively. It corresponds to an increase by 19%, 18% and 15% each, but diminishes along with the longitudinal coordinate down to 8 and 5 kW/m² (7% and 6% more) for the higher and middle angles of attack, respectively. Moreover, it is confirmed that there is in effect no more difference for the lower angle of attack case starting from $x \sim 190$ mm.

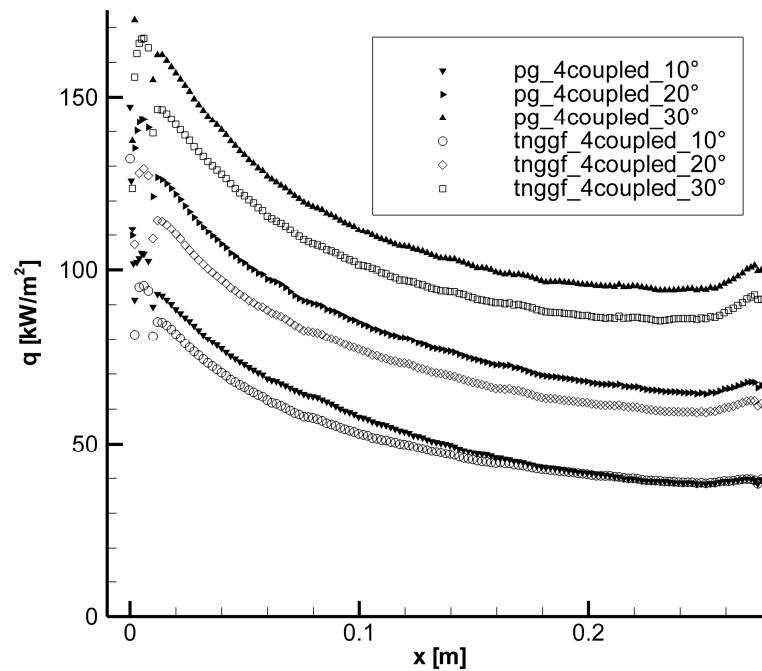


Figure 4.6.8. Heat flux distribution on the coupling surface. Nozzle flow in thermochemical non-equilibrium with fluid-structure interaction and comparison with perfect gas modeling.

The coupled solutions are thus rather close to the previous computations. Although the flow conditions vary, it must be emphasized that the reservoir values are the same. The total energetic content characterizing the flow is indeed unchanged, and this constitutes a fundamental impact on the thermal quantities at the interface.

4.7 Summary of the results

As pointed out so far, it is possible to deduce that the different phenomena here investigated have not a particular influence on the thermal quantities at the model surface. Although the uncoupled results can considerably differ, the integration of the thermal response of the model leads to comparable results. The distributions of the thermal quantities on the interface are in general very

close, in particular on the ceramic horizontal plate, which is the objective component. The perfect gas modeling of section 4.3 is thus reasonably sufficient for the successive numerical simulations, especially concerning the surface temperature values, which are the most interesting quantities in the current work, since they can directly be compared with measurements in the L3K facility.

Variations due to the flow modeling can then be taken into account according to tables 4.7.1 to 4.7.6. The values are computed as differences with respect to the perfect gas modeling if the simulation is performed with another model. The abbreviation “avg” is here intended as the averaged value of the difference. The position $x=140$ mm is chosen as indicative for the variations on the central part of the plate, since it is nearly at its middle.

It can be noticed that the influence of a different modeling is generally increased at higher angles of attack, determining larger relative variations of the thermal quantities.

Table 4.7.1. Relative temperature difference with thermochemical modeling inside the chamber. Uniform stream. Reference inflow data.

α	ΔT_{\max}	ΔT_{avg}	ΔT_{\min}	$\Delta T_{x=0.14\text{m}}$
10°	1.01%	-0.54%	-1.88%	-0.51%
20°	-0.81%	-0.98%	-2.34%	-0.89%

Table 4.7.2. Relative heat flux difference with thermochemical modeling inside the chamber. Uniform stream. Reference inflow data.

α	Δq_{\max}	Δq_{avg}	Δq_{\min}	$\Delta q_{x=0.14\text{m}}$
10°	3.99%	-2.96%	-5.92%	-1.77%
20°	-1.72%	-3.92%	-6.31%	-3.01%

Table 4.7.3. Relative temperature difference with divergent stream. Inflow quantities evaluated with nozzle in chemical non-equilibrium and thermodynamic equilibrium. Adapted perfect gas model inside the test chamber.

α	ΔT_{\max}	ΔT_{avg}	ΔT_{\min}	$\Delta T_{x=0.14\text{m}}$
10°	1.59%	0.47%	-0.15%	0.42%
20°	0.73%	-1.13%	-2.90%	-1.14%

Table 4.7.4. Relative heat flux difference with divergent stream. Inflow quantities evaluated with nozzle in chemical non-equilibrium and thermodynamic equilibrium. Adapted perfect gas model inside the test chamber.

α	Δq_{\max}	Δq_{avg}	Δq_{\min}	$\Delta q_{x=0.14\text{m}}$
10°	11.26%	1.93%	-1.35%	1.45%
20°	5.40%	-3.40%	-9.58%	-4.13%

Table 4.7.5. Relative temperature difference with inflow quantities evaluated with nozzle in thermochemical non-equilibrium. Uniform flow. Adapted perfect gas model inside the test chamber.

α	ΔT_{\max}	ΔT_{avg}	ΔT_{\min}	$\Delta T_{x=0.14\text{m}}$
10°	0.06%	-1.31%	-2.61%	-1.25%
20°	-1.78%	-2.44%	-3.45%	-2.39%
30°	-1.98%	-2.42%	-3.18%	-2.28%

Table 4.7.6. Relative heat flux difference with inflow quantities evaluated with nozzle in thermochemical non-equilibrium. Uniform flow. Adapted perfect gas model inside the test chamber.

α	Δq_{\max}	Δq_{avg}	Δq_{\min}	$\Delta q_{x=0.14\text{m}}$
10°	0.50%	-5.85%	-14.54%	-4.09%
20°	-6.08%	-9.27%	-17.52%	-8.06%
30°	-7.11%	-9.07%	-18.78%	-8.10%

Chapter 5

Investigations on the flat-plate model

The current chapter treats the actual comparison between numerical simulations and experiments and hence with the validation of the considered coupling environment. The experimental campaign and the tested model are introduced and the measurements and their post-processing are presented. Numerical simulations on the flat-plate model are conducted and the computations are then compared with the ground-based facility data. Further numerical investigations are subsequently performed in order to better understand some aspects which have emerged during the comparison.

5.1 Investigated model and experimental campaign

The investigated model is shown in figures 5.1.1 and 5.1.2.



Figure 5.1.1. Investigated model (disassembled). Copper nose, steel support and KAPYROK are visible. Side view (left) and global view (right, also with cooling system pipes)

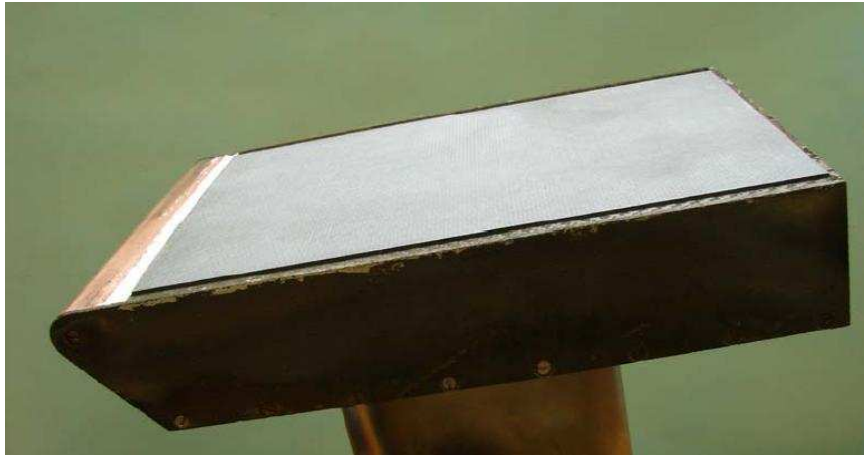


Figure 5.1.2. Investigated model (mounted). Horizontal and side plates are visible.

It consists of a ceramic flat plate, made of C/C-SiC, which is the focus of the investigations. Its in-plane dimensions are 251 mm (length)×188 mm (width) and its thickness is 3 mm. The plate is delimited by the isolating material KAPYROK in the front, by a perpendicular plate of the same C/C-SiC material in the back, by other two C/C-SiC plates at its sides and is screwed to a base support of stainless steel, which is maintained at a temperature of ca. 300 K through water-cooling. The inter-space between plate and support is wholly filled with KAPYROK. The rear and lateral plates are also 3 mm thick. The construction is furthermore completed by a copper water-cooled nose. The nose radius of 10 mm is designed in order to obtain sufficient cooling for the model within the complete working area of L3K.

As explained in chapter 4, the isolating material enables thermal separation between ceramic elements and components maintained at constant temperature, thanks to its thermal conductivity much inferior than the values of C/C-SiC, copper and steel. The rear and side plates allow preserving material continuity and offer a protection to possible damages.

The upper surface of the ceramic horizontal plate is coated through chemical vapor deposition (CVD) by a SiC layer, which improves the surface resistance to oxidation.

The geometrical details of the model can be examined in Appendix C.

In order to perform the requested thermal analysis, the plate is equipped with a measurement system for the acquisition of temperatures on its superior and inferior surfaces. The instrumentation consists of 14 thermocouples, 3 spectral pyrometers, 2 two-colour pyrometers and the IR camera. As discussed so far, the thermocouples are not suitable for the use on the upper surface, and are positioned on the bottom of the plate. This enables also investigating the evolution of the temperature in the model. The thermocouples are fixed at the

base and led to the desired spot through the insulating material, as shown in figure 5.1.3.



Figure 5.1.3. Positioning of the thermocouples. Installation on the base support (left) and positions after the integration of the KAPYROK (right).

Nine of them are distributed under the horizontal plate subdivided in 4 rows, at ca. 30, 85, 140 and 195 mm from the frontal edge of the horizontal plate, respectively. There are three thermocouples in the first row, one on the longitudinal symmetry axis and the other two mirror-like at a distance of ca. 40 mm from the symmetry axis. The other six thermocouples, two in each row, follow this symmetrical arrangement.

Four thermocouples are integrated on the symmetry axis in correspondence of each row but 20 mm deeper inside the insulating part beneath the plate, in order to capture also the temperature development in this component. The remaining thermocouple is installed on the base support with the aim of safety monitoring the evolution of its temperature.

After the placement of the thermocouples, the actual coordinates of their junction ends are measured. They are summarized in table 5.1.1 and figure 5.1.4 offers a sketch of their positions on the model.

Table 5.1.1. Positions of the thermocouples with respect to the frame placed on the symmetry axis at the frontal edge of the isolation piece.

Spot	x [mm]	y [mm]	z [mm]
1	37	-40	-3
2	39	0	-3
3	40	39	-3
4	95	-39	-3
5	95	40	-3
6	151	-40	-3
7	151	41	-3
8	205	40	-3
9	205	40	-3
10	40	0	-23
11	95	0	-23
12	150	0	-23
13	205	0	-23

The optical instrumentation is placed outside the test chamber and accesses the model via the windows. The spectral pyrometers point down to the surface in correspondence of the spots 2, 4 and 6, so that a straightforward comparison with the thermocouple measurements at these spots can be obtained. They are subdivided according to their sensitive temperature range, e.g. the S-3000 pyrometer on the spot ahead – where the temperature is expected to be higher – and so forth.

The two-colour pyrometers measure the same surface spots 2 and 4 as the spectral pyrometers (see table 5.1.2). Two-colour and spectral pyrometers give the fundamental references for quantitative temperature measurements with the IR-camera.

Table 5.1.2. Measurement positions of the pyrometers.

Pyrometer	2C-3000	S-3000	2C-2000	S-2000	MINOLTA
Position	Spot 2	Spot 2	Spot 4	Spot 4	Spot 6

A global view of the applied measurement system is given in figure 5.1.4.

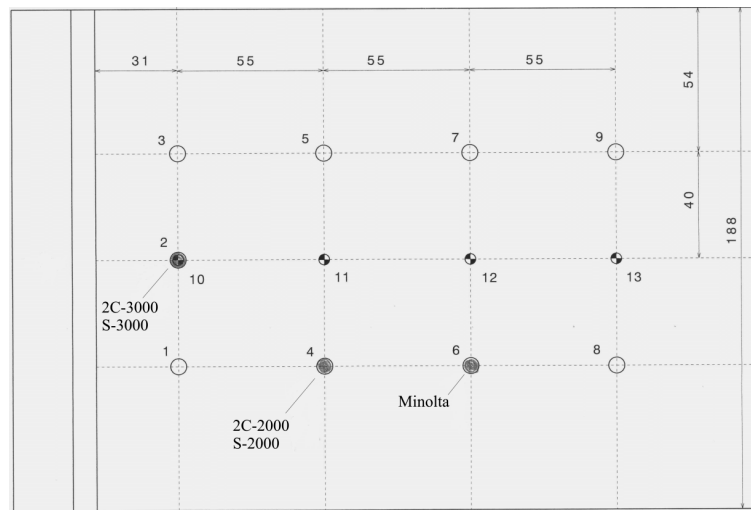


Figure 5.1.4. Sketch of the positions of thermocouples and pyrometers on the model. View from above. Stream coming from left.

The pyrometers are placed in correspondence of the small windows. The “3000” and “2000” pyrometers are placed in pairs at the windows to the side of the facility access door, while the Minolta pyrometer at the small window on top of the test chamber. The IR-camera is positioned at one of the two main windows, which the access door is provided with.

Moreover, there is a CCD video camera which allows monitoring the global situation inside the chamber during the test. It is mounted at the other main window of the access door.

The optical accesses to the model are shown in figure 5.1.5.



Figure 5.1.5. L3K test chamber. The small windows on the right provide the access to the pairs of pyrometers. The CCD-camera is visible at the access door.

All optical devices are adjusted at angles lower than $\pm 60^\circ$ with respect to the normal to the surface at the measured point, in order to avoid errors in the temperature measurement at large viewing angles [95]. The IR-camera is hence installed at ca. $+45^\circ$, the Minolta pyrometer at ca. -45° and the other pyrometers nearly perpendicular to the surface.

The model deformations occurring during the experimental campaign can be neglected, in virtue of the very high rigidity of the model.

The aerodynamic x -axis is directed downstream and the z -axis downwards as well as the body x -axis is directed to the model rear and the z -axis downwards. In the current work, the angle of attack is intended to be positive if the model nose points down.

The test procedure may be summarized as follows. In the beginning the model is outside the stream, and the arc heater is ignited. The model is already adjusted at the desired angle of attack. Once stationary flow conditions are obtained, the model is moved into the stream, and the actual test begins. An exposure to the stream of 3-5 minutes usually is considered sufficient to obtain suitable measurements. Then the model is moved outside the stream, the actual test period is finished and the arc heater is switched off. After that, the model is again shifted to the test position in order to get also records of the cooling phase. This in-and-out shifting procedure is performed for safety reasons, since the model could be damaged if left inside the stream during the switch-off of the arc heater.

It is important to mention that many tests are scheduled for the same ceramic material. In order to preserve its integrity, the model is therefore moved outwards when the signals of the more interesting quantities to be investigated have reached a steady value. It can mean that some other sensors have not reached the steady value yet, in particular the thermocouples of the last row backwards and inside the KAPYROK.

Figure 5.1.6 depicts the investigated model in the test chamber.



Figure 5.1.6. Model inside the L3K test chamber.

The operating conditions for the tests in L3K are summarized in table 5.1.3. The nozzle exit diameter is set to 300 mm.

Table 5.1.3. Reservoir conditions and mass flow rate in the L3K facility.

T_0 [K]	5400
p_0 [Pa]	$4.55 \cdot 10^5$
h_0 [MJ/kg]	10.82
Mass flow rate [kg/s]	0.142

A first test has revealed to be necessary to tune the facility parameters in order to get the desired reservoir conditions. Figure 5.1.7 displays how the reservoir pressure is too high in comparison to the desired value of 4.55 bar.

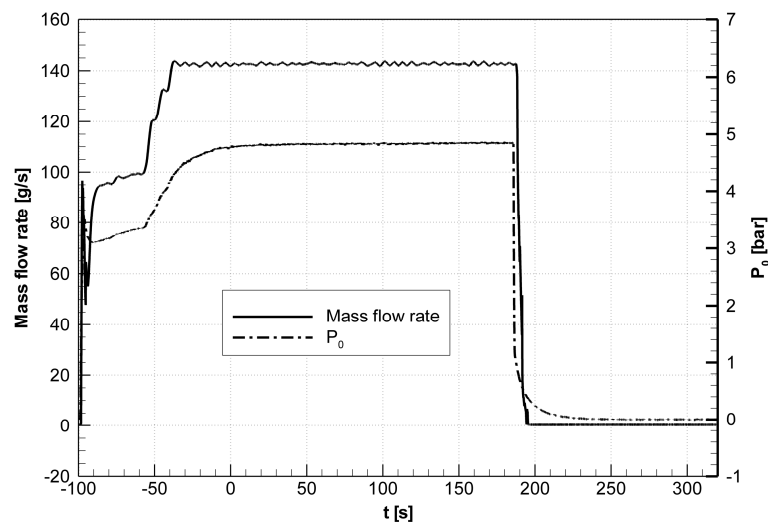


Figure 5.1.7. Mass flow rate and reservoir pressure time evolution. Desired mass flow rate (0.142 kg/s), but too high reservoir pressure (4.85 bar instead of 4.55). Preliminary test-001.

The tests results have shown to be in general very well reproducible. Two tests per angle of attack are hence considered satisfactory. Table 5.1.4 reports the test schedule with the relative exposure times: tests at the higher angle of attack are run for 3 minutes, while 4-5 minutes are necessary for the 10° and 20° configuration.

Table 5.1.4. Test cases.

Test	α [°]	Run time [s]
002	10	240
003	10	300
005	20	240
006	20	240
007	30	180
008	30	180

5.1.1 Experimental results

Figures 5.1.1.1 to 5.1.1.7 display the surface temperature measurements collected by the pyrometers. It is possible to notice that the surface temperatures need not longer than 150-180 s to reach a steady value, of course depending on the considered position and configuration. In order to make the comprehension of the figures easier, the testing time is marked by grey background colour. If tests with different run durations are presented in the same plot, red and yellow are used as well. After the model is moved outside the stream, the signals abruptly drop down to the initial values, since the visual contact is interrupted. If either the temperature level is sufficiently high or the measurement range minimum is sufficiently low, it is possible to obtain also the temperature evolution of the cooling phase. The spectral pyrometer at spot 4 is not capable to get any measurements for the tests at the lower angle of attack, since the temperature level is too low.

It is important to underline the general good agreement between temperatures measured by spectral and two-colour pyrometers at the same spot and the very good results reproducibility of tests run at the same angle of attack. The good concordance of the measurements of the two pyrometers types has been made possible by the correct setting of the spectral pyrometers emissivity, which has been arranged to $\varepsilon = 0.85$.

In the examination of the pyrometers records it must be remarked that they start to sense the temperature from different values because of their internal electronic. Thus, the “3000” and Minolta pyrometer signals start from the inferior temperature of the range, while those of the “2000” pyrometers from 0°C. Moreover, the two-colour pyrometers typically present an overshoot when they begin to measure, also due to the internal electronic.

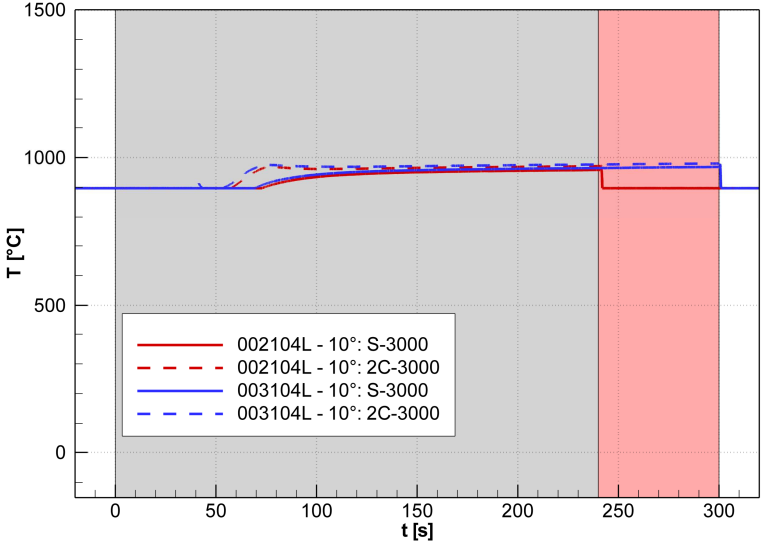


Figure 5.1.1.1. Pyrometers measurements. Spot 2. $\alpha=10^\circ$.

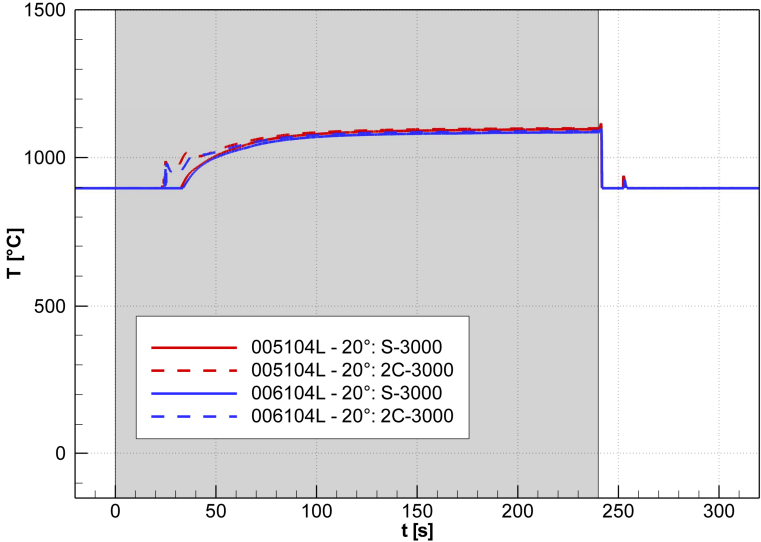


Figure 5.1.1.2. Pyrometers measurements. Spot 2. $\alpha=20^\circ$.

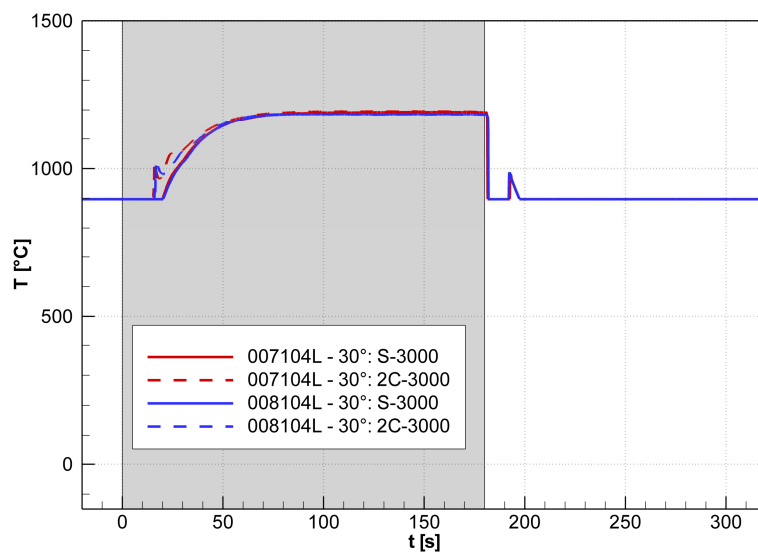


Figure 5.1.1.3. Pyrometers measurements. Spot 2. $\alpha=30^\circ$.

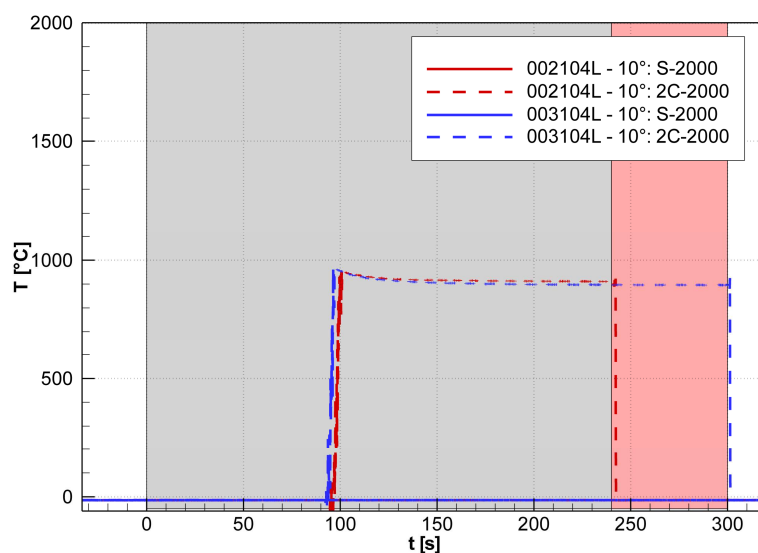
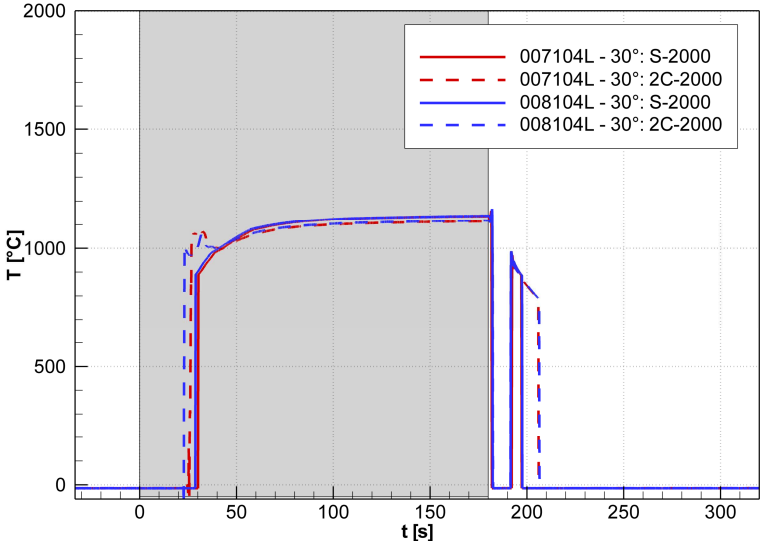
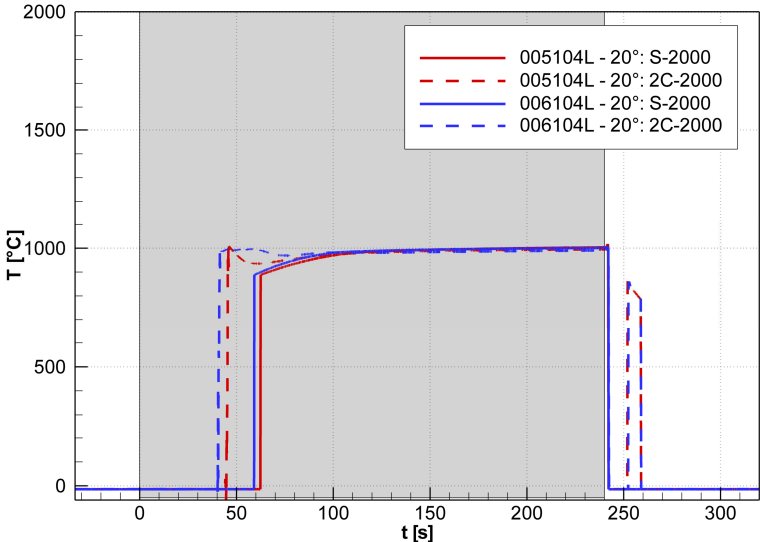


Figure 5.1.1.4. Pyrometers measurements. Spot 4. $\alpha=10^\circ$.



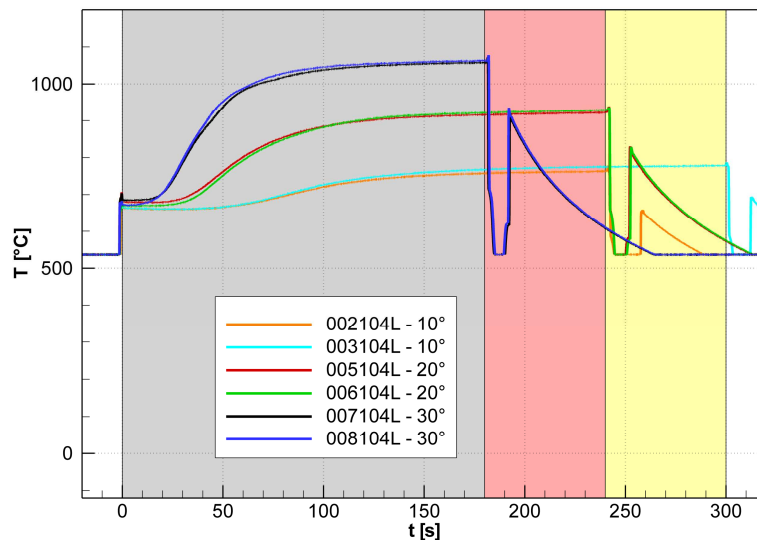


Figure 5.1.1.7. Pyrometers measurements. Spot 6.

The records of the thermocouples measurements are plotted in figures 5.1.1.8 to 5.1.1.19. Beneath the horizontal plate, steady conditions are more difficult to be reached, because of the rather high heat capacity of the C/C-SiC material. The signals of the thermocouples indeed take longer to achieve a steady value, and some of them do not reach it at all. The problem arises in particular for the tests with the 10° configuration and is more pronounced downstream. Furthermore, the perfect contact between junction end and inferior surface of the plate is not ensured. This occurrence can have an impact on both, the necessary time to reach the steady state and on the accuracy of the measured temperature.

It is possible to evince that the symmetry of the temperature measurements in lateral direction is in general rather satisfactory. This is especially emphasized at the lower angles of attack, for which less three-dimensional effects occur.

The reproducibility of the measurements obtained for tests with the same configuration is noteworthy also for the thermocouples.

Because of the rather high heat capacity of the model and the low heat conductivity of the KAPYROK, the necessary evolution time for the temperature inside the structure is really high. This is evident by the examination of the thermocouples measurements at the deeper positions (figure 5.1.1.20): for all cases, the test duration was too short to achieve steady-state temperature levels.

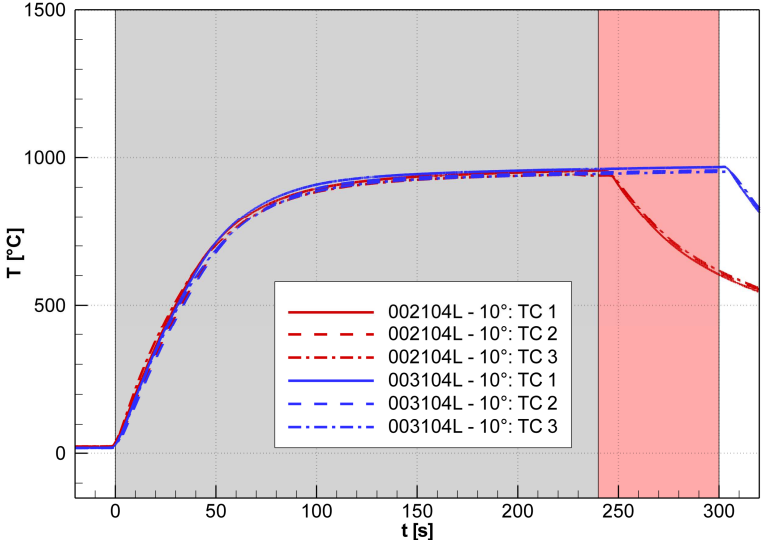


Figure 5.1.1.8. Thermocouples measurements. First row. $\alpha=10^\circ$.

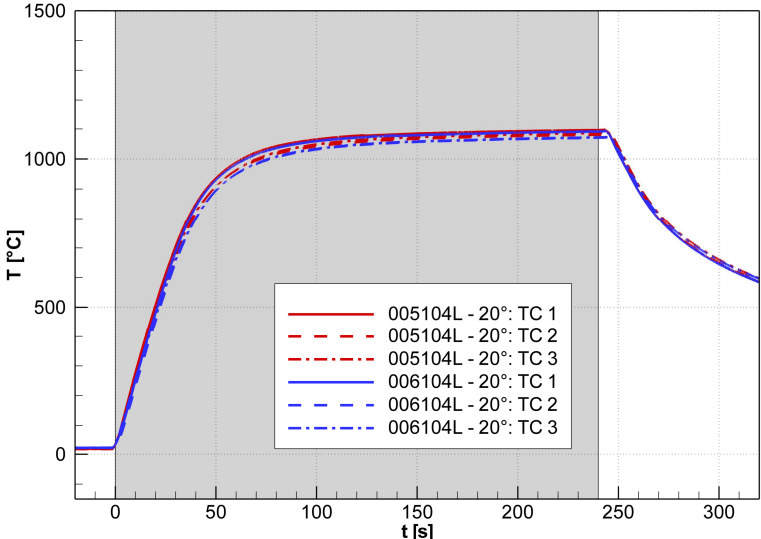


Figure 5.1.1.9. Thermocouples measurements. First row. $\alpha=20^\circ$.

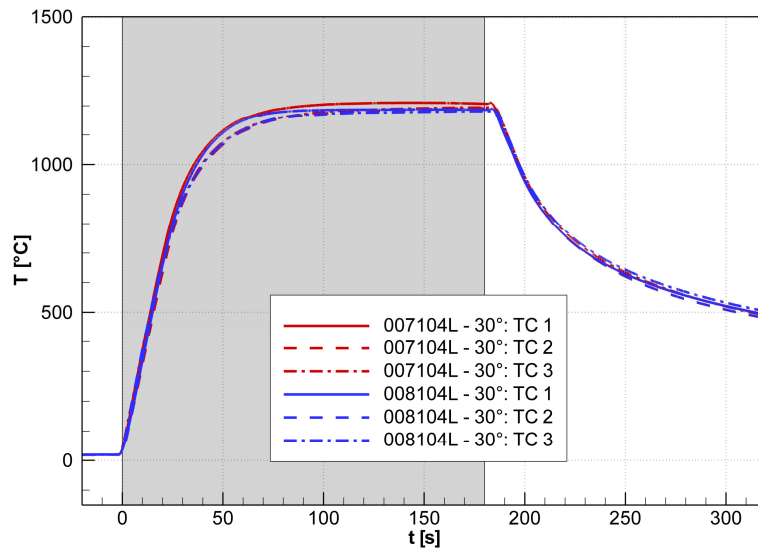


Figure 5.1.1.10. Thermocouples measurements. First row. $\alpha=30^\circ$.

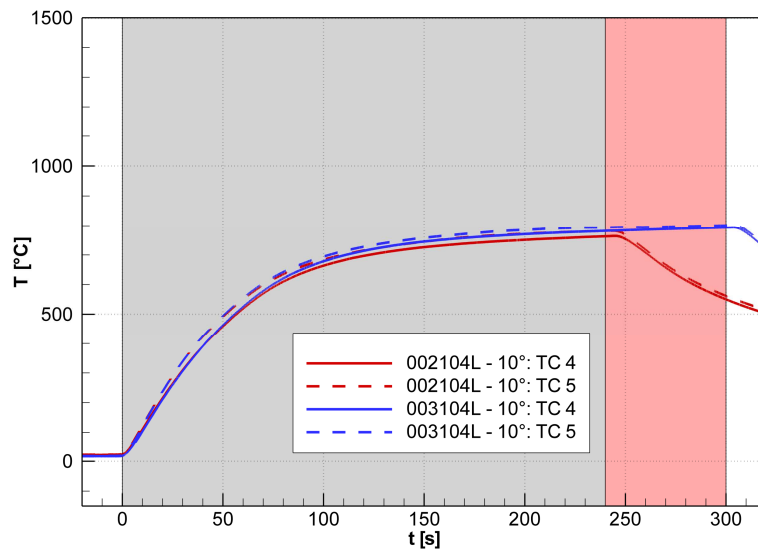


Figure 5.1.1.11. Thermocouples measurements. Second row. $\alpha=10^\circ$.

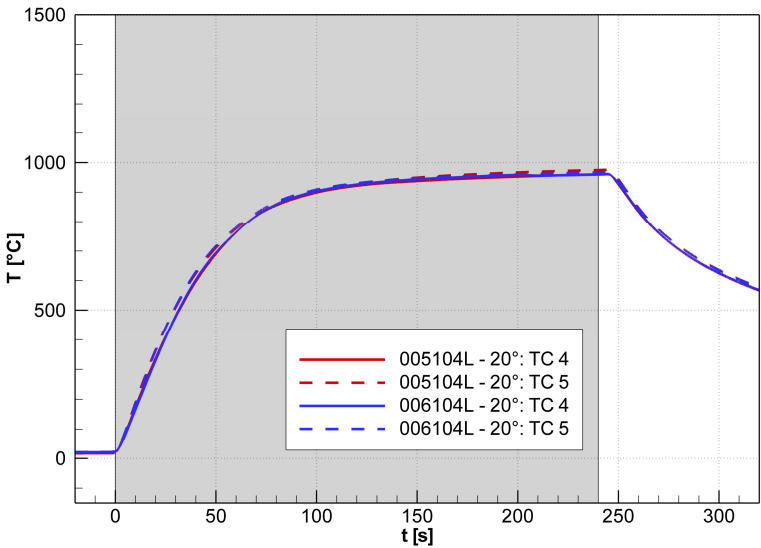


Figure 5.1.1.12. Thermocouples measurements. Second row. $\alpha=20^\circ$.

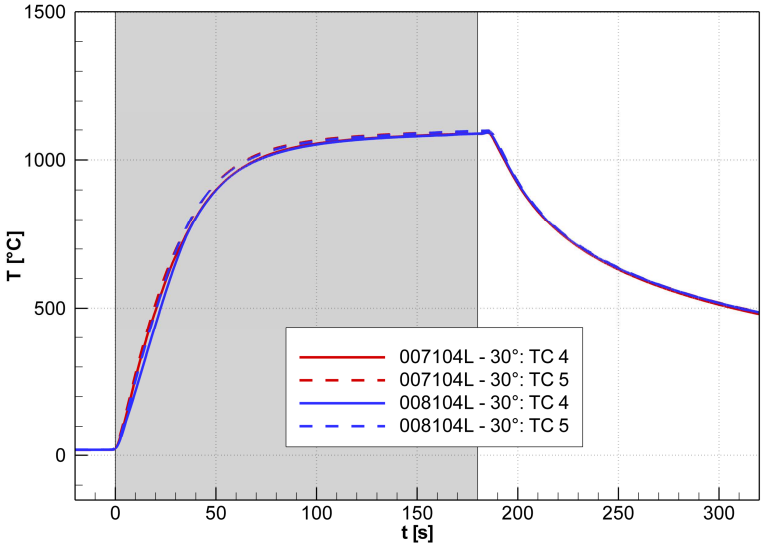


Figure 5.1.1.13. Thermocouples measurements. Second row. $\alpha=30^\circ$.

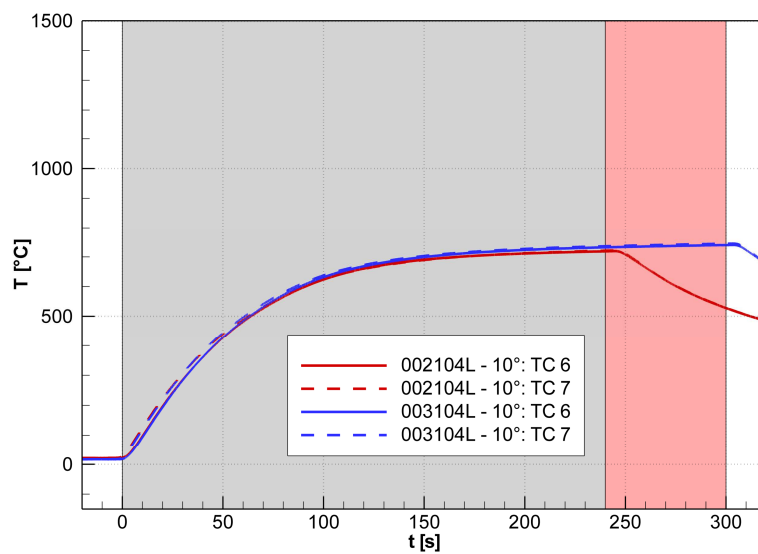


Figure 5.1.1.14. Thermocouples measurements. Third row. $\alpha=10^\circ$.

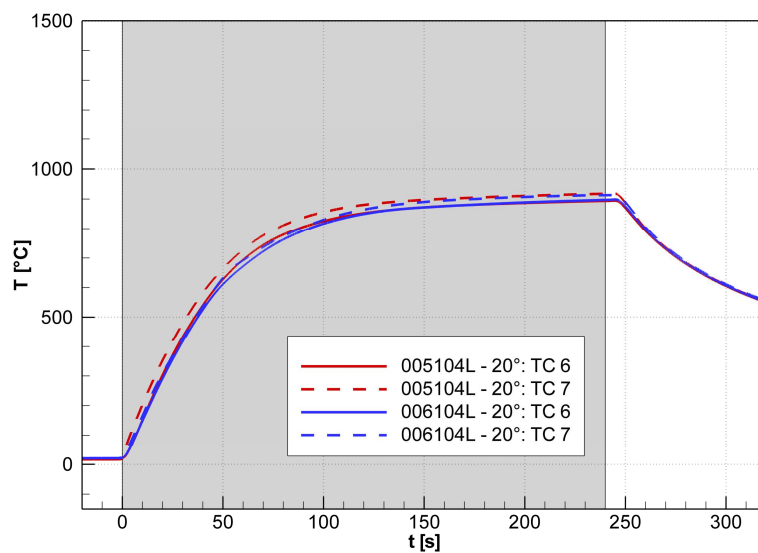


Figure 5.1.1.15. Thermocouples measurements. Third row. $\alpha=20^\circ$.

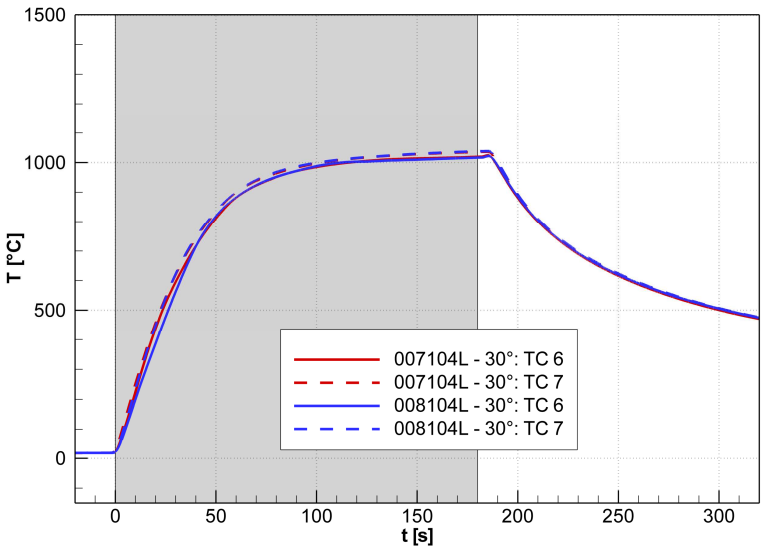


Figure 5.1.1.16. Thermocouples measurements. Third row. $\alpha=30^\circ$.

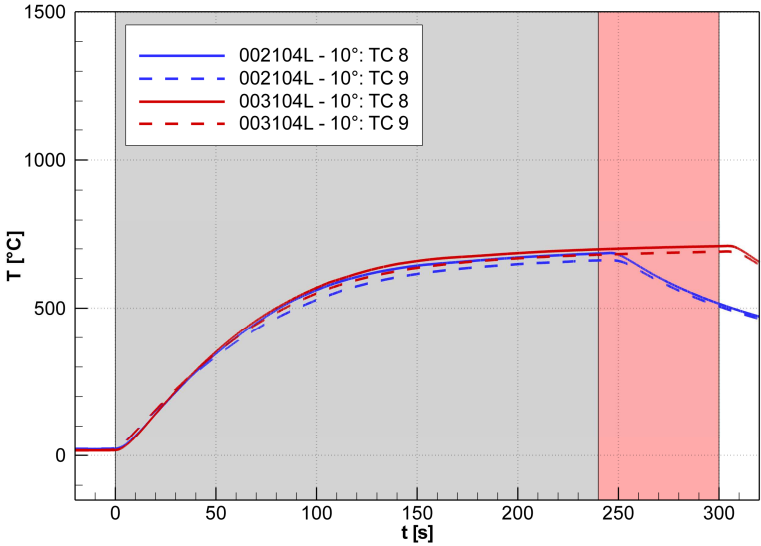


Figure 5.1.1.17. Thermocouples measurements. Fourth row. $\alpha=10^\circ$.

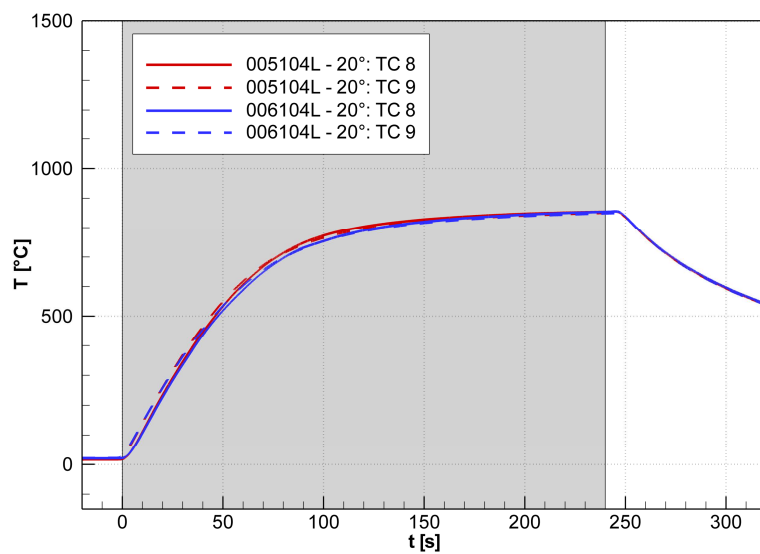


Figure 5.1.1.18. Thermocouples measurements. Fourth row. $\alpha=20^\circ$.

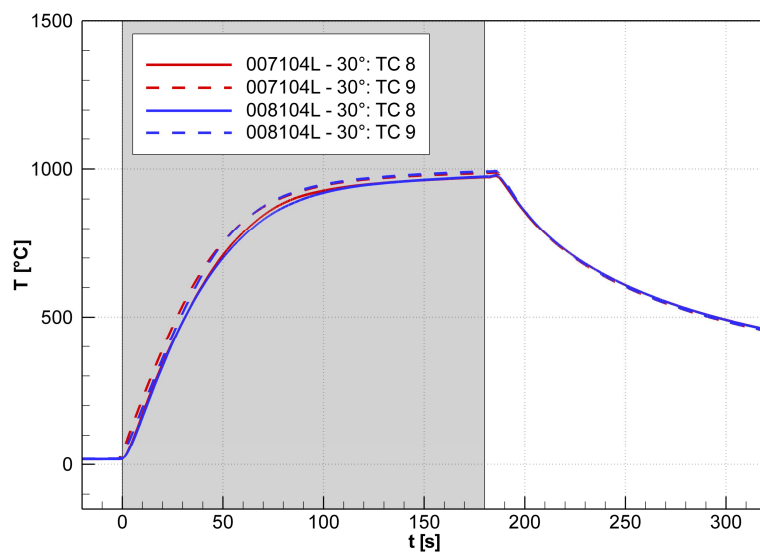


Figure 5.1.1.19. Thermocouples measurements. Fourth row. $\alpha=30^\circ$.

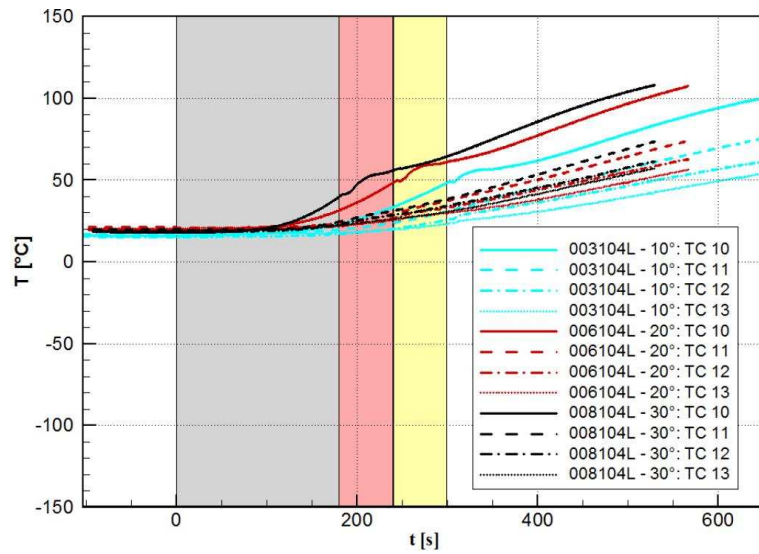


Figure 5.1.1.20. Thermocouples measurements. Second perpendicular position. Tests 003, 005 and 007.

The evolution of the IR-camera measurements agrees with the records of the other instruments. In particular, the surface temperature measured by this device generally shows to reach a steady state over the exposure time. Anyway, it is rather difficult to achieve a steady condition for the tests at the lowest angle of attack, also owing to the IR-camera manufacture. Figure 5.1.1.21, taken from the second test with the 10° configuration, helps pointing out these facts.

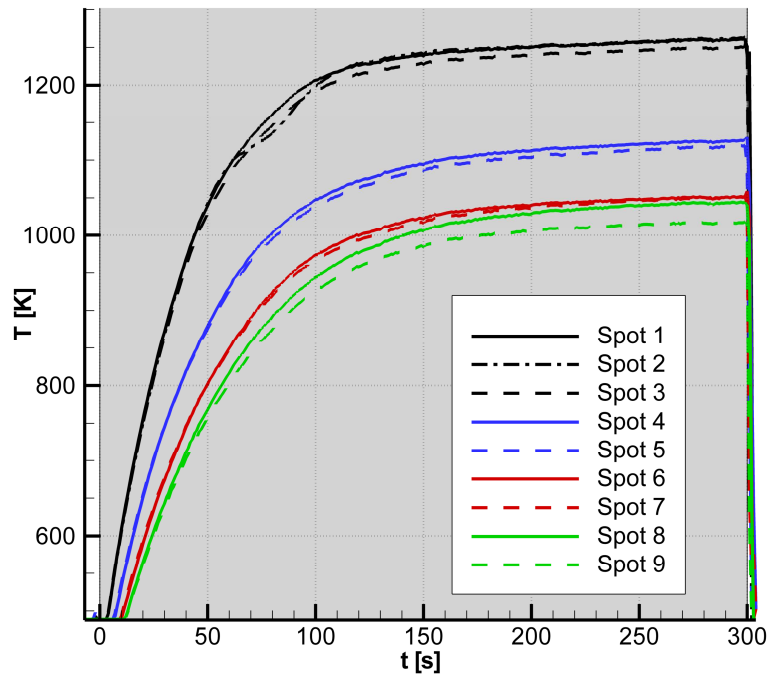


Figure 5.1.1.21. IR-camera measurements. $\epsilon=0.83$. Test-003, $\alpha=10^\circ$.

The temperature distribution in lateral direction is confirmed to be rather uniform, as depicted in figure 5.1.1.22. In this case, the data of only one test per configuration are displayed, in view of the good reproducibility of the results. This is common also for other plots in the following.

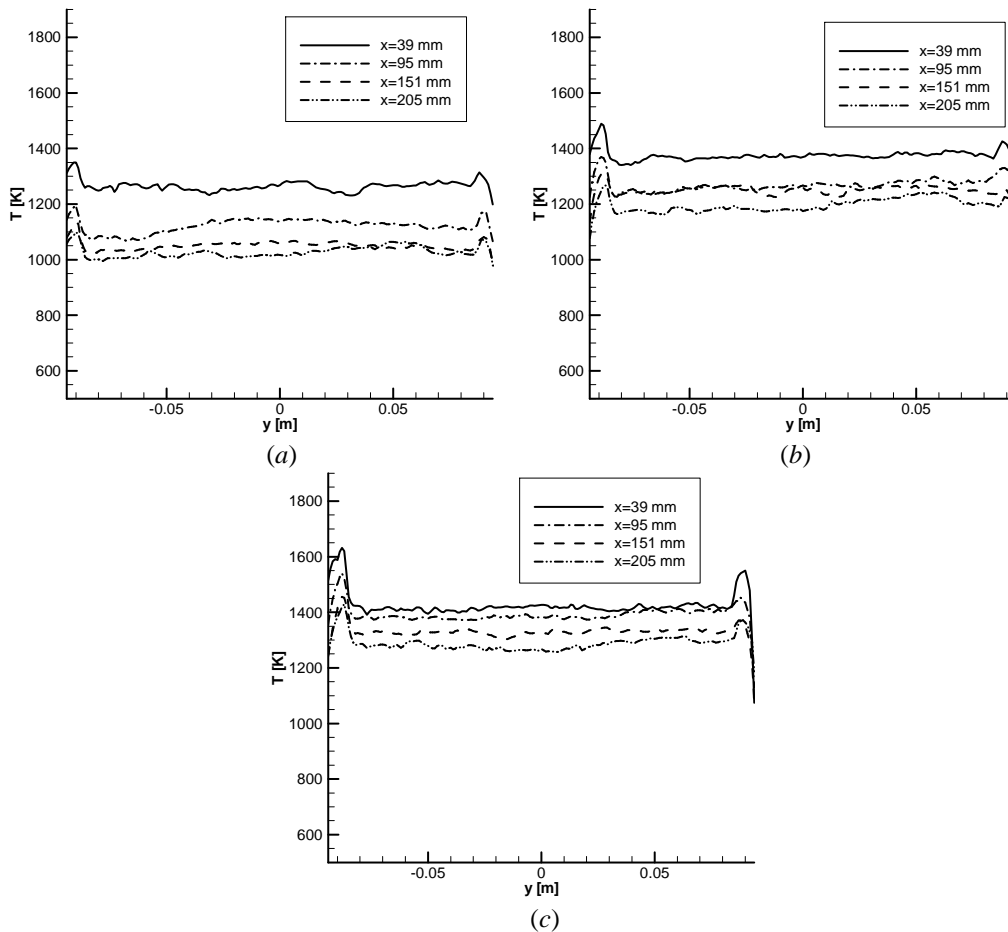


Figure 5.1.1.22. IR-camera measurements in lateral direction. $\varepsilon=0.83$. (a): test-003, $\alpha=10^\circ$; (b): test-006, $\alpha=20^\circ$; (c): test-008, $\alpha=30^\circ$.

The peaks on the extreme lateral positions are mainly due to two reasons [30]. Firstly, the difficulty for the IR-camera in discriminating the temperature discontinuities, since the image resolution is not capable to properly capture large temperature gradients. This is particularly emphasized at the lateral edge, which borders on the background in the camera image (i.e. at $y=-94$ mm). The temperature variation is here even a step: the peak is thus more pronounced than at the other lateral edge, where the lateral plate is present in the image and the temperature discontinuity is consequently less marked. The second reason is the occurrence of three-dimensional effects at the model edges, which can enhance

the acting thermal load. Moreover, minor effects can be due to a possible imperfect thermal contact between lateral and horizontal plates.

The following pictures, taken also from test 003 at specified times, show the temperature evolution on the plate surface during the test (figure 5.1.1.23). The flow comes from the right. The model is moved into the stream and is initially cold, see image (a). The model is then heated up and the surface temperature increases rather rapidly, as shown in images (b) and (c) and confirmed also by the examination of figure 5.1.1.21. The highest temperatures are reached on the upstream end. In the second part of the test, the temperature raises less markedly, as depicted in image (d). The temperature gradient with respect to the testing time is in effect less pronounced, see again figure 5.1.1.21.

The temperature on the isolation is not physical: the emissivity value indeed differs with the one specified in the IR-camera software for the ceramic components. Correspondingly, the temperatures indicated for this part are too high.

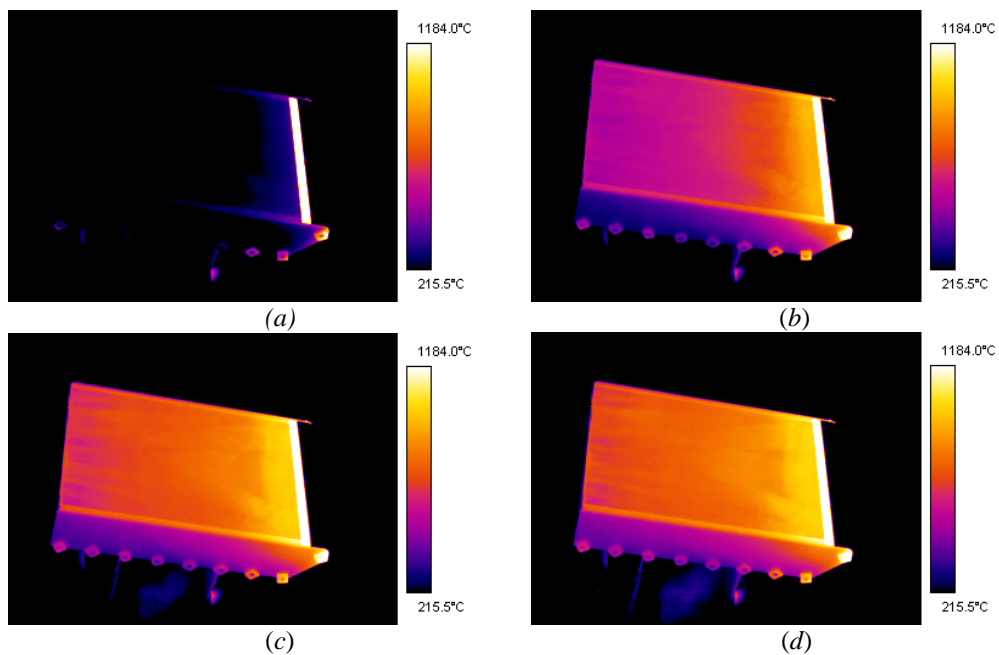


Figure 5.1.1.23. IR-camera records. $\varepsilon=0.83$. Test-003, $\alpha=10^\circ$. Stream from the right. (a): $t=5$ s; (b) $t=60$ s; (c): $t=120$ s; (d): $t=180$ s.

5.1.2 Post-processing of the experimental data

For a detailed analysis of the experimental results, the measurements of all instruments are considered at the time just before the movement of the model outside the stream.

The thermocouples records are taken at exactly this time, although it has been shown that some of them do not fully reach a steady state.

The pyrometer data are corrected by means of the calibration procedure introduced in section 3.2.4. These corrected data are fundamental for the subsequent post-processing of the IR-camera records. After the correction, the data achieved at the same spot by spectral and two-colour pyrometers get really close, such that they are in general almost overlapped. This allows having certain reliability in the local temperature measurements. Reliability is also improved by the lower temperature level of the thermocouples data measured below the plate in comparison with the pyrometers measurements at the same spots, which indicates a good reproduction of the local heat transfer.

As already discussed in section 3.2.2.2, the first post-processing step allows obtaining data in the model-fixed coordinate system. The transformation to this frame needs at least seven parameters. In the present work the four plate corners and the two inferior corners of the base support are chosen, and the transformation parameters are obtained by least-squares approximation, analogously to the procedure described in [32]. The used marker points are displayed in figure 5.1.2.1, taken from the tests with the 10° configuration.

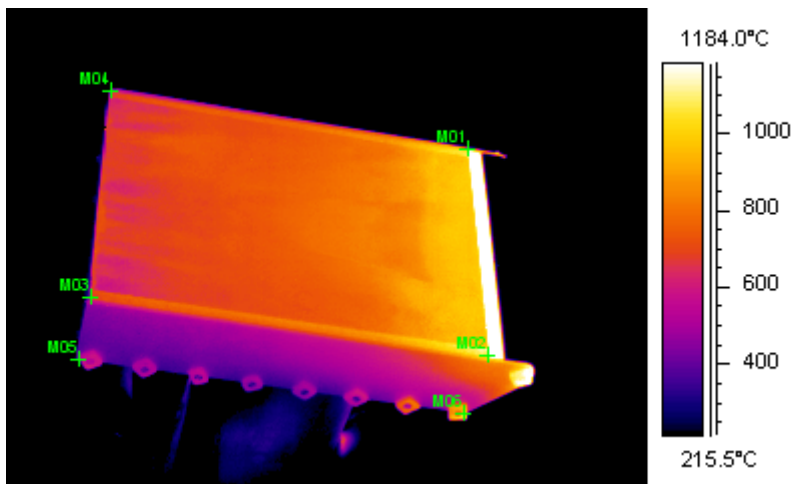


Figure 5.1.2.1. Marker points (in green) used for the post-processing. $\varepsilon=0.83$. 10° configuration.

Once the parameters are known, it is possible also to complete the opposite operation of placing some markers on the IR-images in correspondence of the

thermocouples and pyrometers spots. This is useful for the second post-processing step. The spots on the images are then widened to an area of approx. 6 mm^2 , which corresponds to 6 pixels, as shown in figure 5.1.2.2. The 6 mm^2 area is chosen in order to reproduce the spot encompassed by the pyrometers, so that a direct comparison with their measurements can be achieved. Because of the discrimination incapability of the IR-camera, the local temperature distribution is treated as Gaussian (see section 3.2.5): the temperature average on the spot is thus taken into account.

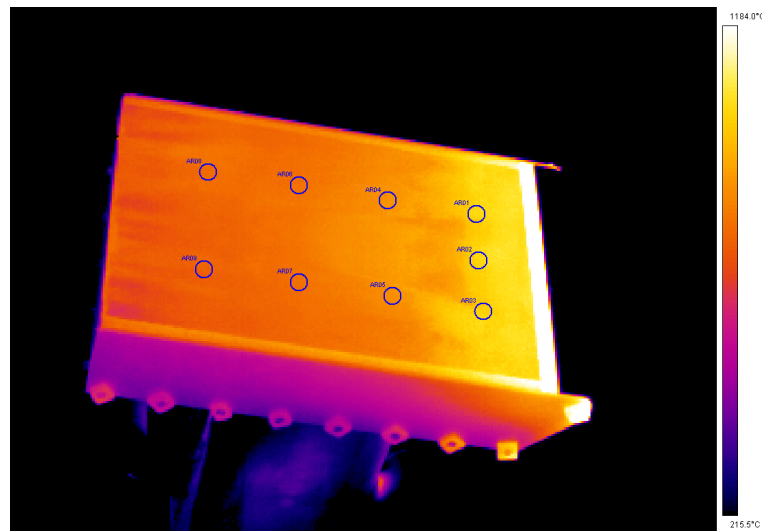


Figure 5.1.2.2. Spots (in blue) used for the post-processing. $\varepsilon=0.83$. 10° configuration.

A comparison between the temperatures measured on the spots by the different devices, as depicted in figure 5.1.2.3, enables beginning the analysis of these results in order to achieve a suitable value of the emissivity, see section 3.2.2.2. Since the amount of the optical set-up transmittance has been fixed through the procedure discussed in section 3.2.3, the emissivity actually is the appropriate value which modifies the product $\varepsilon\tau$ contained in (3.2.2.5) in order to account for possible transmittance disturbances as well as emissivity variations, which can arise at high-enthalpy conditions, as expounded in section 3.2.2.

From the examination of figure 5.1.2.3, it is interesting to evince the fairly good agreement of the trends captured by IR-camera and thermocouples over the spots, in particular the concordance of the slight temperature variation in lateral direction at the last row downstream for the 10° configuration.

IR-camera data for $\varepsilon = 0.80$ and $\varepsilon = 0.84$ are reported in order to principally demonstrate the influence of the emissivity on the evaluation of the IR-camera records.

Best agreement with the other measurements is then obtained for $\varepsilon = 0.83$. Therefore, this value is taken as global emissivity for the analysis of the IR-camera data.

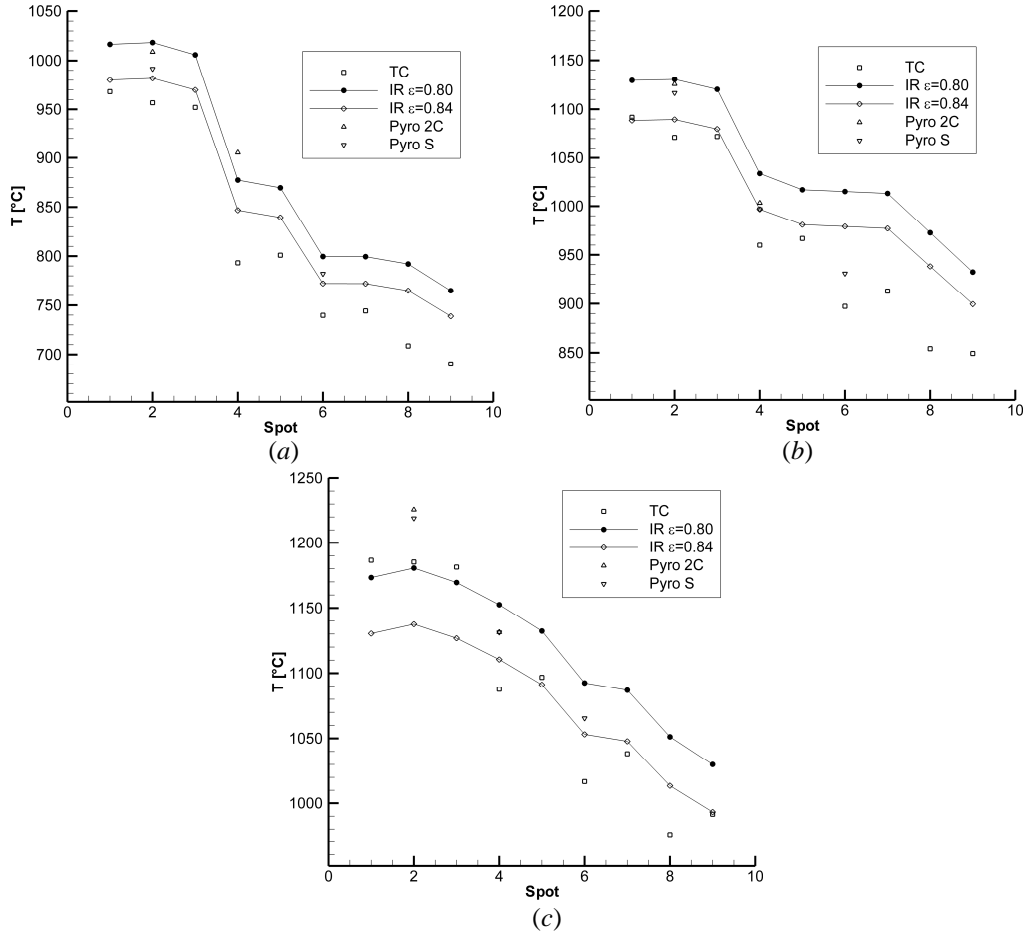


Figure 5.1.2.3. Measured temperatures over the spots with the different devices. (a): test-003, $\alpha=10^\circ$; (b): test-006, $\alpha=20^\circ$; (c): test-008, $\alpha=30^\circ$.

Figure 5.1.2.4, taken from test 005 as an example, points out the good fitting of IR-camera and pyrometers data with the chosen emissivity value. The abbreviations “TC_L”, “TC_C” and “TC_R” refer here and in the following to the thermocouples data at $y=-40$ mm, $y=0$ mm and $y=+40$ mm, respectively.

The agreement of the measurements in lateral direction is noteworthy for both, IR-camera and thermocouples.

Temperature peaks arise at the front and rear edges of the plate. On the latter, the phenomenon can be explained as in section 5.1.1 for the peaks in lateral direction. For the former, the difficulty principally lies on the discontinuity between the two materials (ceramics and KAPYROK), namely on the different

emissivity values, which determine a severe difference in the radiation performances, and on the unlike catalytic behaviour, which can cause the increase of the heat flux loading the C/C-SiC surface. The difficulty of the IR-camera in resolving this material discontinuity cannot be regulated even by setting a suitable value of the emissivity. Unfortunately no reliable data can be achieved with the IR-camera on the frontal and rear surfaces.

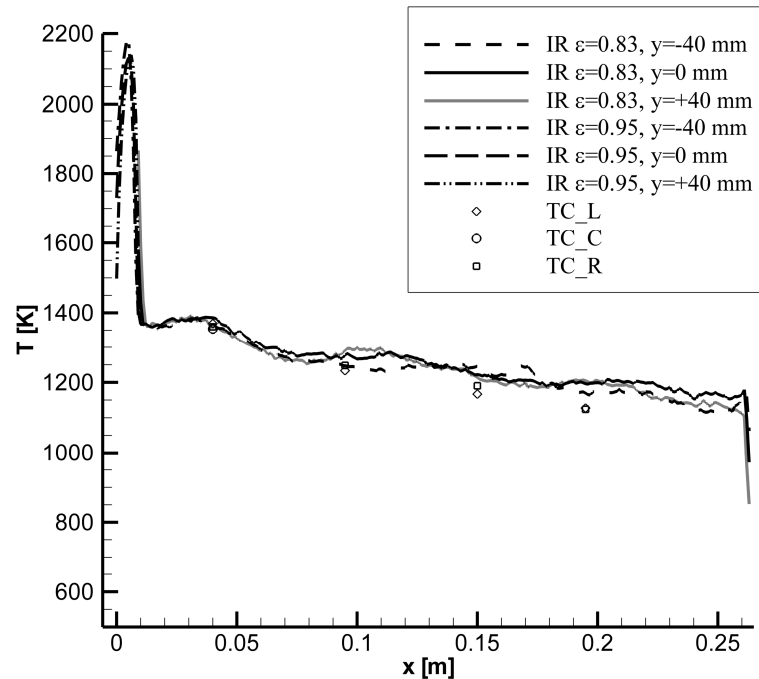


Figure 5.1.2.4. Measured temperatures on the flat-plate. Corrected values. Test-005, $\alpha=20^\circ$.

Once nominal temperature values are assessed, it is possible to go ahead with the estimation of the uncertainties affecting the measurements, as explained in section 3.2.5. The detailed plot of the experimental results is presented in section 5.3 together with the comparison with the numerical results. It can be remarked that the uncertainty affecting thermocouples and pyrometers measurements amounts to ca. ± 10 K, while the one affecting the IR-camera data is ca. ± 20 K.

5.2 Numerical investigations on the flat-plate model

The configuration chosen for the computational investigations consists of the model introduced in section 5.1 exposed to wind tunnel flow conditions. This differs of course from real flight conditions, but allows getting more easily – and cheaper – a comparison with experimental data and hence a straightforward confirmation of the accuracy of the numerical predictions.

Considering the works [30] and [31] on similar configurations and the examination of the experimental results, it is possible to bring some simplifications in the concerned problem. First of all, the flow along the symmetry plane can be reasonably treated as bi-dimensional, in view of the model width of 194 mm and of the rather small nose radius. This fact is confirmed by the measurements in lateral direction, which have shown small temperature variations only.

In the same way, the symmetric structural properties with respect to the longitudinal plane do not introduce three-dimensional effects. The calculations for investigating the symmetry plane can therefore be restricted to a bi-dimensional problem.

The flow is simulated as steady, in virtue of the already mentioned rather long running time of the L3K facility. Moreover, the structure analysis is reduced to a steady 2-D heat transfer problem. This is fine for the examination of the temperature distribution on the horizontal plate, although it does not completely take into account the temperature evolution inside the model, which has been previously shown to need a longer time to reach steady conditions.

The calculations of the structural response are performed assuming ideal thermal contact between the different components of the model.

Computations for all three configurations (10° , 20° and 30° angles of attack) are conducted.

The computational problem is hence very similar to the study carried out in chapter 4 and several considerations can be derived from those results. The preliminary geometry for those investigations was in fact very close to the assembled experimental model. Therefore, the actual geometry basically differs from the previous one only for the length of the horizontal plate and correspondingly of the isolation block and base support, which are ca. 12 mm shorter, but the main geometrical differences are on a region where no crucial effects on the global problem occur.

The coupling interface is thus limited to the surfaces of the horizontal and rear plates as well as of the frontal isolation piece. The flow is assessed to be thermochemically frozen at the nozzle exit, to be nearly uniform and to remain laminar throughout the test chamber. The perfect gas modeling and the flow conditions are taken from sections 4.1 and 4.3 and are sufficiently suitable for the present investigations. Remarks about effects of divergent flow and thermochemistry can then be referred to section 4.7.

The wall is first treated as non-catalytic.

The flowfield and structure modeling follow the guidelines of sections 4.2 and 4.3 and the fluid and structure domains are therefore very similar to the ones of the previous chapter. They are depicted in figures 5.2.1 and 5.2.2.

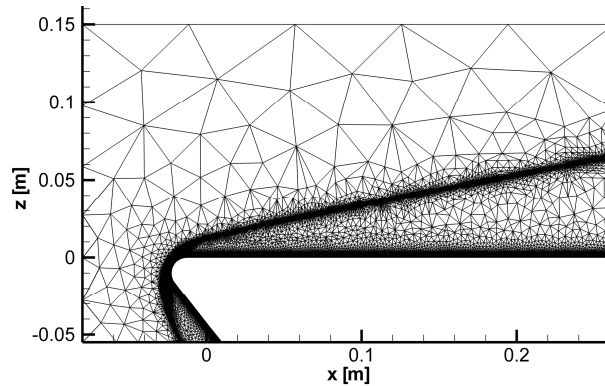


Figure 5.2.1. Fluid domain with final mesh. 30° configuration.

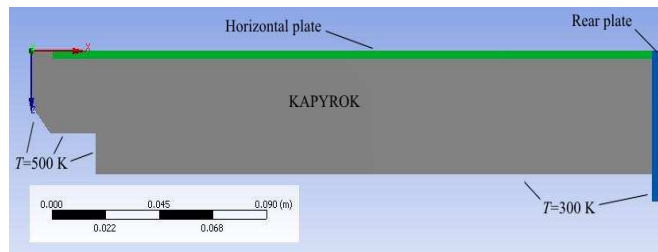


Figure 5.2.2. Structure field and relative coordinate system.

The initial hybrid mesh for the flowfield is in this case composed of ca. $7 \cdot 10^3$ triangular and ca. $5 \cdot 10^3$ quadrangular elements. The latter are distributed in 28 layers in proximity of the surface, with a minimal thickness of $3 \cdot 10^{-5}$ m and a stretching ratio of 1.05. The mesh is then adapted many times within the startup solution of the flow problem and kept unaltered for the successive coupling iterations. The total number of elements of the conclusive very fine grid amounts to ca. $1.5 \cdot 10^5$ and ca. $1 \cdot 10^4$ for the unstructured and structured mesh, respectively. The surface points on the coupling interface are again around 300. The water-cooling of nose and base support is accounted for by setting a uniform temperature boundary condition of 500 K and 300 K, respectively, while the initial temperature distribution over the coupling interface is obtained through the imposition of radiative equilibrium – with the same parameters as before – and then through the structure solution. The multi-grid scheme and the upwind discretization are maintained as in chapter 4.

Analogously, the structure to be computed comprehends the most important components, with uniform temperature boundary conditions at the interfaces with nose and base support. The non-linear temperature-dependent properties of the used materials and the orthotropic behaviour of the C/C-SiC as well as the radiation towards the background are integrated in the thermal analysis. The background temperature is assumed to be constant at 300 K.

The quasi-structured grid relates to section 4.2. A resolution of about $1 \cdot 10^{-3}$ m per element side is regarded as adequate.

The coupling procedure is performed as in the previous chapter.

The results for radiative equilibrium boundary condition are obtained after the startup adaptation cycle. As expectable, they do not remarkably differ from the investigations of chapter 4. The temperature field for the three configurations is depicted in figures 5.2.3 to 5.2.5.

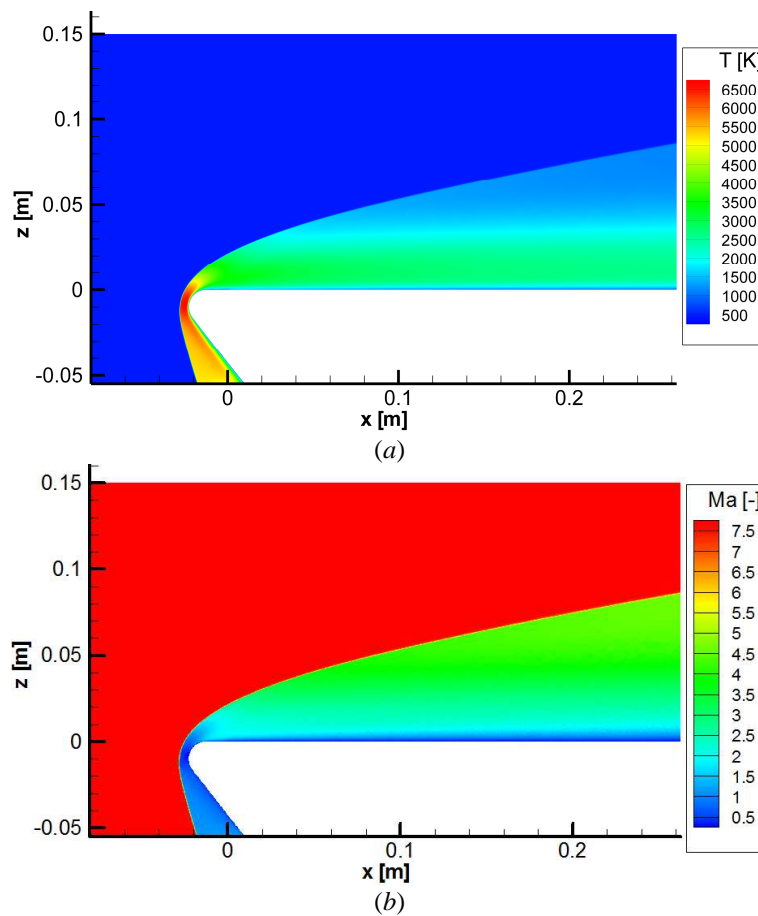


Figure 5.2.3. Distribution of temperature (a) and Mach number (b) in the flowfield. $\alpha=10^\circ$.

The temperature distribution in the fluid domain is characterized by a maximum for all three configurations of about 6630 K in front of the nose, similarly to the reference computations of chapter 4.

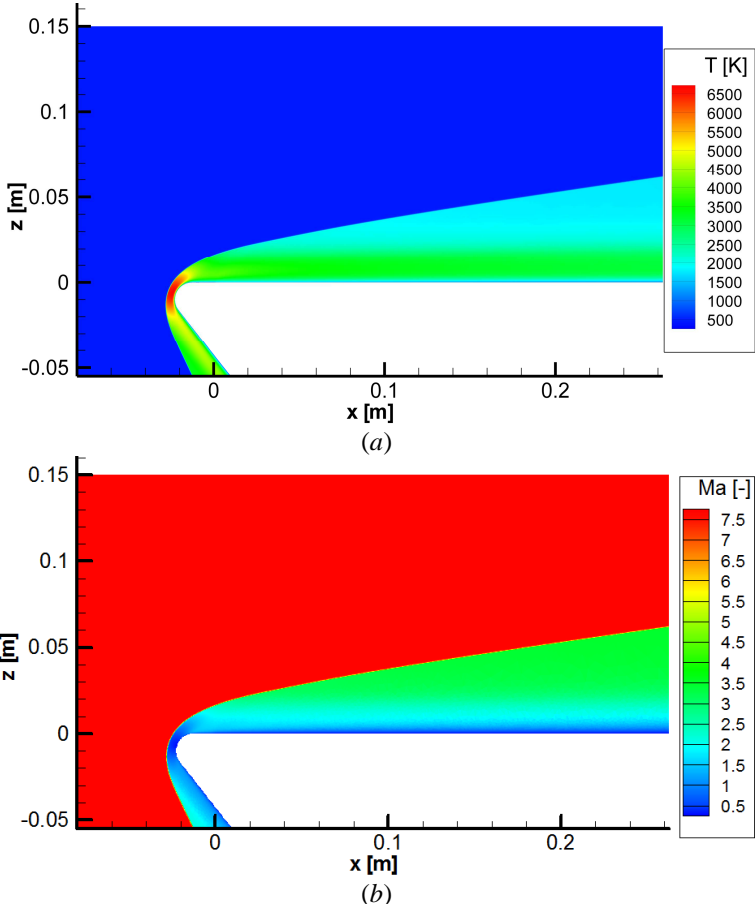


Figure 5.2.4. Distribution of temperature (a) and Mach number (b) in the flowfield. $\alpha=20^\circ$.

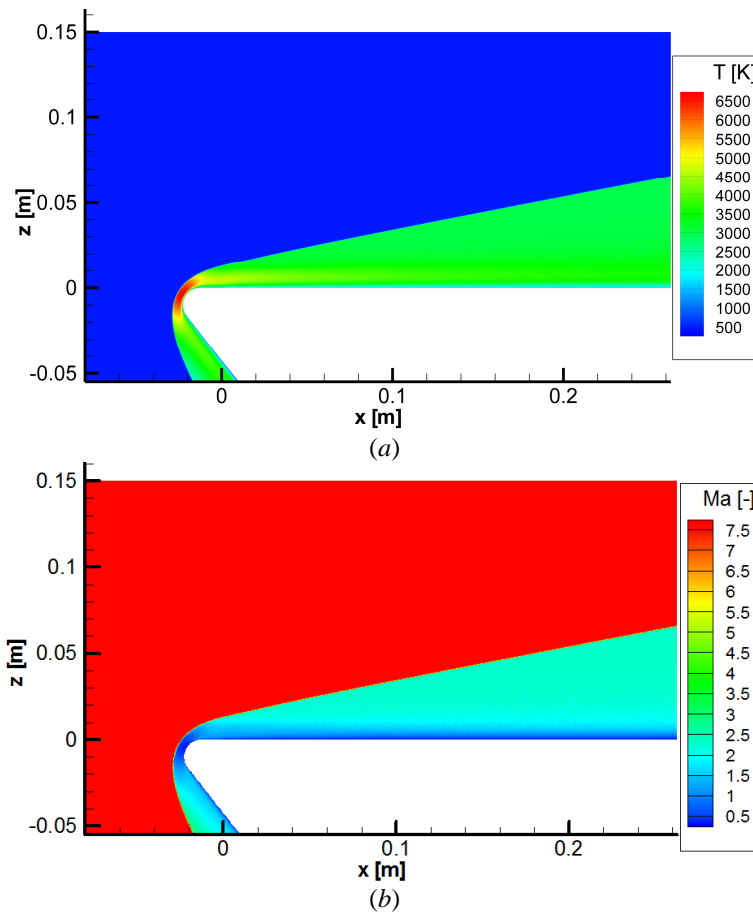


Figure 5.2.5. Distribution of temperature (a) and Mach number (b) in the flowfield. $\alpha=30^\circ$.

Also the temperature distribution on the coupling surface is really close to what has been obtained in section 4.3. As figure 5.2.6 points out, the positive gradient on the fore surface is very pronounced and the temperature reaches a maximal value at the interface between KAPYROK and C/C-SiC. It occurs for all configurations at $x=11$ mm (the connection is at $x=9$ mm) as a consequence of the emissivity difference of the two materials and it amounts to 1169 K, 1260 K and 1339 K for the 10° , 20° and 30° configuration, respectively. After the peak, the surface temperature shows a negative slope along with the longitudinal coordinate down to a value of 933 K, 1032 K and 1133 K for the 10° , 20° and 30° configuration, respectively. The angle of attack has a remarkable effect, since at 30° the surface temperatures are even 100 K and 200 K higher than for the 20° and 10° case, respectively.

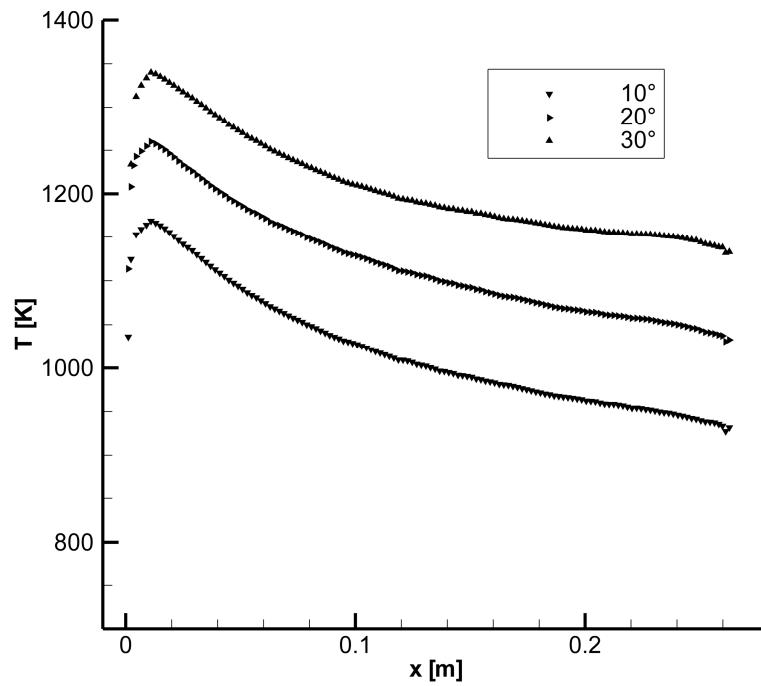


Figure 5.2.6. Temperature distribution on the coupling surface. Perfect gas modeling with radiative equilibrium boundary condition.

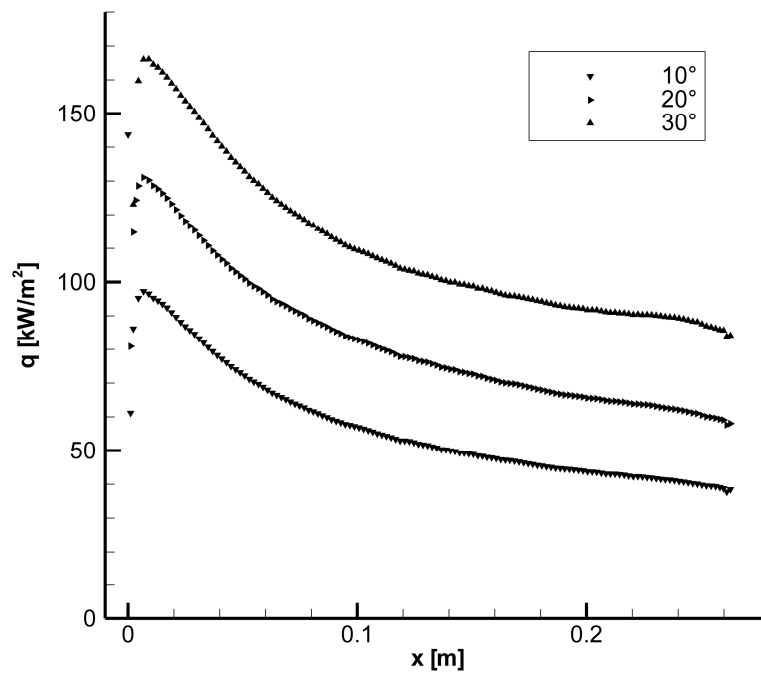


Figure 5.2.7. Heat flux distribution on the coupling surface. Perfect gas modeling with radiative equilibrium boundary condition.

The heat flux trend on the surface keeps in pace with these results, see figure 5.2.7. The load is characterized by a maximum of the fore region of about 100, 130 and 170 kW/m² and evolves on the surface down to a minimum of approx. 40, 55 and 85 kW/m² for the 10°, 20° and 30° configuration, respectively. The coupled simulations are started with the initial heat flux distribution. As already explained, the inter-field iterations after the first one focus on convergence. It is confirmed that 4 coupling iterations are sufficient to reach convergence and that the convergence is stable (i.e. the relaxation parameter Φ is simply set to 1). The convergence of the thermal quantities is summarized in tables 5.2.1 to 5.2.3.

Table 5.2.1. Convergence of the thermal quantities. Perfect gas modeling. $\alpha=10^\circ$.

Iteration	ΔT_{\max}	$\Delta T_{x=0.14\text{m}}$	Δq_{\max}	$\Delta q_{x=0.14\text{m}}$
uncoupled - 1	-2.20E+02	-5.46E+00	9.96E+03	5.10E+01
1 - 2	-2.49E+01	-3.85E-01	4.07E+03	1.07E+01
2 - 3	8.83E+00	1.00E-01	-1.44E+03	-3.83E+00
3 - 4	-2.87E+00	-5.00E-02	4.67E+02	2.21E+00

Table 5.2.2. Convergence of the thermal quantities. Perfect gas modeling. $\alpha=20^\circ$.

Iteration	ΔT_{\max}	$\Delta T_{x=0.14\text{m}}$	Δq_{\max}	$\Delta q_{x=0.14\text{m}}$
uncoupled - 1	-2.36E+02	-5.25E+00	1.09E+04	9.97E+01
1 - 2	-2.35E+01	-4.15E-01	4.83E+03	2.63E+01
2 - 3	9.06E+00	8.00E-02	-1.83E+03	-3.63E+00
3 - 4	-2.97E+00	-1.99E-02	5.88E+02	-3.26E-01

Table 5.2.3. Convergence of the thermal quantities. Perfect gas modeling. $\alpha=30^\circ$.

Iteration	ΔT_{\max}	$\Delta T_{x=0.14\text{m}}$	Δq_{\max}	$\Delta q_{x=0.14\text{m}}$
uncoupled - 1	-2.55E+02	-4.40E+00	1.55E+04	5.94E+01
1 - 2	-2.85E+01	-2.70E-01	1.72E+03	7.32E+00
2 - 3	3.87E+00	4.50E-02	-5.78E+02	-2.56E+00
3 - 4	-5.11E-01	-2.50E-02	2.39E+01	2.22E-01

The structural response is proved to have a fundamental influence on the problem. The combination of the insulating block beneath the horizontal plate with the direction of the fibers in the ceramics causes a component of the heat flux to be transferred to the back, where it is either emitted or further transferred downwards by the rear plate. The frontal temperature maximum is thus mitigated of about 30 K and the peak is generally smoothed to a plateau, which involves 10-20 mm with a few degrees difference, as shown in figure 5.2.8. The maximal surface temperature after the coupling amounts to 1140 K, 1230 K and 1310 K for the 10°, 20° and 30° configuration, respectively. On the other hand,

the radiative equilibrium solution predicts quite well the temperature distribution on the central region, where the variation is less than 10 K.

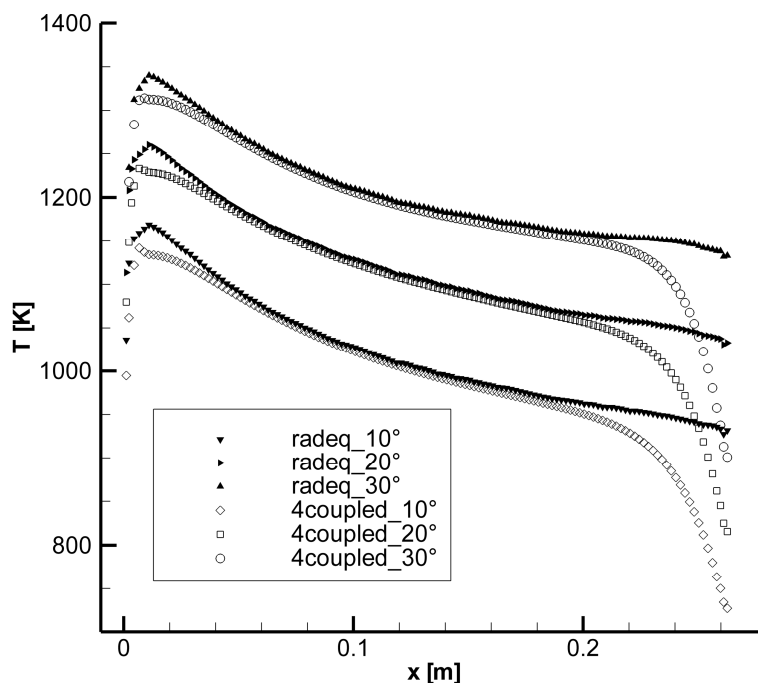


Figure 5.2.8. Temperature distribution on the coupling surface. Perfect gas modeling with fluid-structure interaction and comparison with the uncoupled results.

Anyway, the most distinctive effect is due to the rear plate heat conduction together with its radiation towards the background, which determines a noticeable decrease of the local temperature of 220-255 K. The negative temperature gradient is in this region rather pronounced.

The heat flux shows an analogous behaviour, see figure 5.2.9. The more important variations occur on the frontal and rear coupling surfaces, where the load increases by approx. 10-15 kW/m², while the minor conduction effects on the central domain determine a very slight variation (less than 1 kW/m² in this zone). It is once again interesting that a positive gradient of the heat flux arises on the rear.

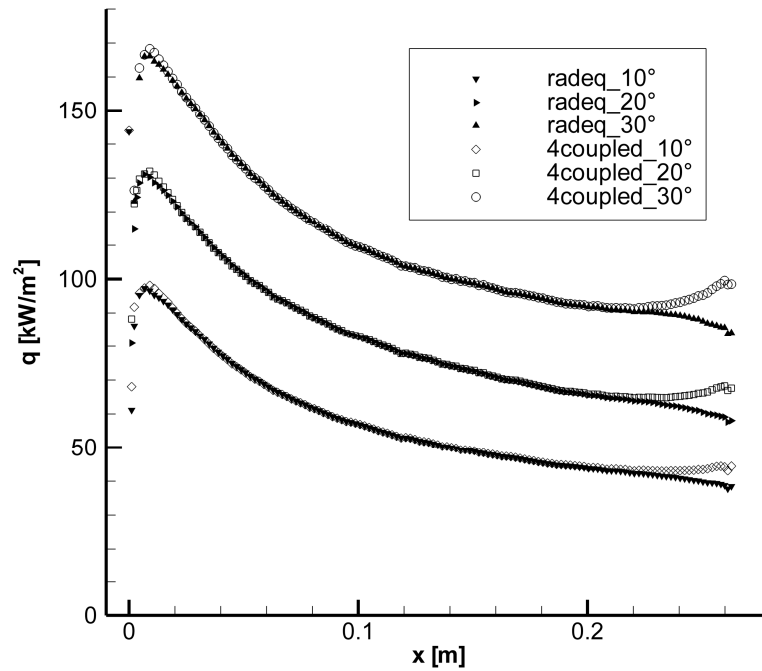


Figure 5.2.9. Heat flux distribution on the coupling surface. Perfect gas modeling with fluid-structure interaction and comparison with the uncoupled results.

The flowfield shows no remarkable differences with the radiative equilibrium simulations.

5.3 Comparison of the results

The first noteworthy aspect which emerges from the comparison of numerical and experimental results is the capability of the computations in capturing the temperature trend on the surface of the horizontal plate. As shown in figures 5.3.1 to 5.3.3, the longitudinal slope of the temperature is very well reproduced, so that the data distributions are nearly parallel. Unfortunately, the IR-camera difficulty in resolving the discontinuities does not enable to achieve suitable measurements in domains close to frontal isolation piece and vertical plate, see section 5.1.2. The comparison is hence not possible on the fore and rear regions of the model, but it properly works on the rest of the investigated plate, where also the other instruments contribute to the evaluation.

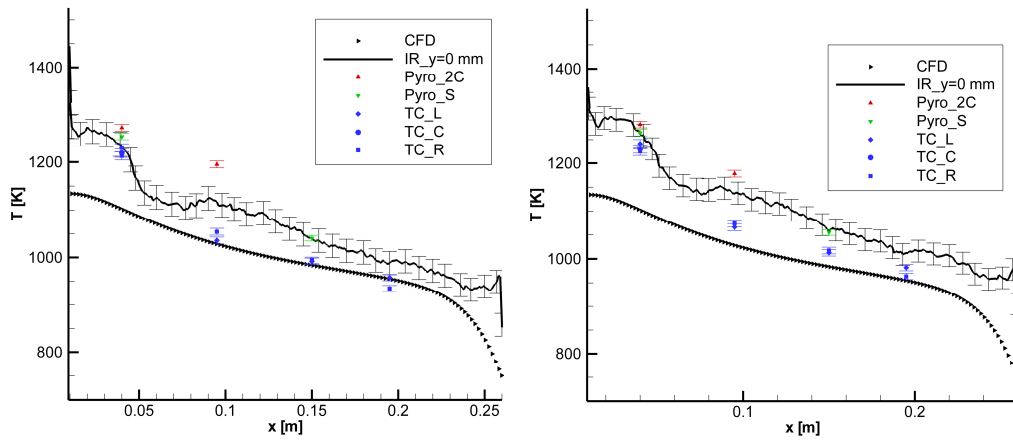


Figure 5.3.1. Comparison of the achieved temperatures on the plate. 10° configuration. Left: test-002; right: test-003.

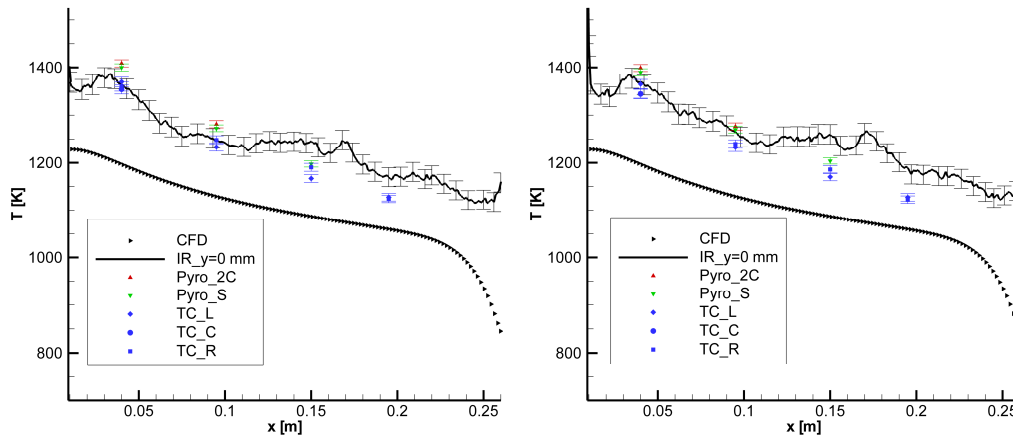


Figure 5.3.2. Comparison of the achieved temperatures on the plate. 20° configuration. Left: test-005; right: test-006.

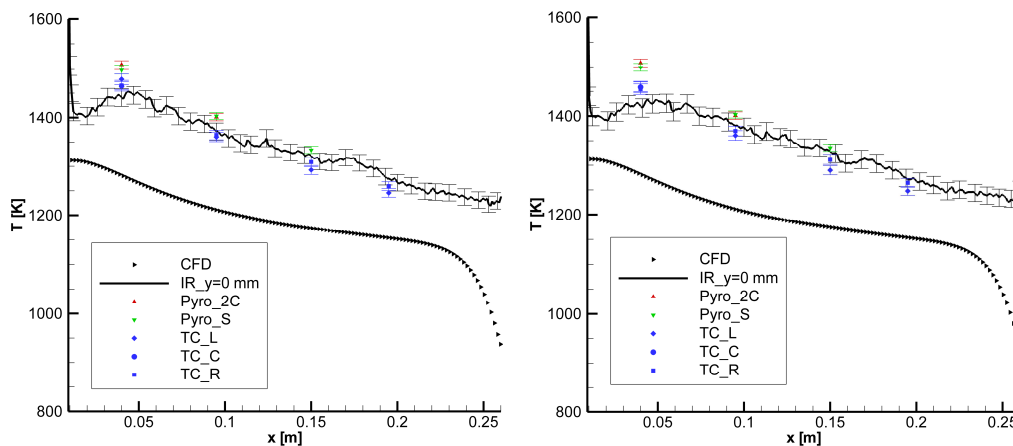


Figure 5.3.3. Comparison of the achieved temperatures on the plate. 30° configuration. Left: test-007; right: test-008.

Although the trends are in general satisfactory captured, there is a remarkable temperature difference between numerical and experimental results. For the 20° and 30° configurations, the difference is almost uniform along with x and amounts to about 150-200 K. On the other hand, it evolves from ca. 150 K on the frontal region down to ca. 70 K on the rear for the 10° case.

The differences between experiments and numerical simulations are summarized in tables 5.3.1 to 5.3.3 for the measurement spots.

Table 5.3.1. Comparison between measured and computed temperatures at the spots.
Temperatures in K. $\alpha=10^\circ$.

x [m]	TC_L	TC_C	TC_R	Pyro 2C	Pyro S	IR $\epsilon=0.83$	CFD_nc
0.040	1241.24	1229.80	1224.95	1281.87	1264.67	1261.17	1105.81
0.095	1066.18	-	1073.99	1178.31	-	1136.76	1029.98
0.150	1012.79	-	1017.26	-	1055.07	1058.48	983.71
0.195	981.73	-	963.33	-	-	1019.89	947.71

Table 5.3.2. Comparison between measured and computed temperatures at the spots.
Temperatures in K. $\alpha=20^\circ$.

x [m]	TC_L	TC_C	TC_R	Pyro 2C	Pyro S	IR $\epsilon=0.83$	CFD_nc
0.040	1364.73	1344.16	1345.07	1398.69	1389.64	1367.92	1200.78
0.095	1232.89	-	1239.78	1276.37	1269.98	1264.98	1130.56
0.150	1170.30	-	1185.87	-	1203.90	1259.92	1086.73
0.195	1127.14	-	1122.28	-	-	1177.96	1053.78

Table 5.3.3. Comparison between measured and computed temperatures at the spots.
Temperatures in K. $\alpha=30^\circ$.

x [m]	TC_L	TC_C	TC_R	Pyro 2C	Pyro S	IR $\epsilon=0.83$	CFD_nc
0.040	1459.62	1458.24	1454.38	1498.69	1492.01	1419.73	1285.84
0.095	1360.70	-	1369.77	1404.40	1404.23	1380.41	1212.52
0.150	1289.72	-	1311.24	-	1338.40	1327.17	1173.74
0.195	1247.86	-	1264.42	-	-	1261.54	1149.26

Two phenomena can be retained as the main reasons which determine these differences. Firstly, chemical interaction effects between gas and ceramics, such as oxidation and recombination at the surface, can considerably intensify the heat load, as discussed in section 1.2.1.

Secondly, a non-perfect contact between horizontal plate and insulating material and between horizontal and rear plates can cause a lack in the heat transfer inside the structure and hence a degradation of the surface temperature mitigation through heat conduction effects.

These two phenomena are numerically investigated in the following section. Unfortunately, the current version of the TAU code has no available modules

which allow studying in detail oxidation and recombination at the ceramic surface. There is, however, the possibility of assuming a full-catalytic behaviour of the surface and drawing some interesting considerations.

5.4 Further numerical investigations

5.4.1 Full-catalytic behaviour of the surface

In order to treat the surface as full-catalytic, it is necessary to switch to a gas modeling which accounts for thermochemical effects. The set-up of the simulations refers therefore to section 4.4. The start solutions have the converged surface temperature distributions achieved in section 5.2 as boundary conditions at the interface. The horizontal and vertical plate surfaces are hence treated no longer as non-catalytic, but as full-catalytic.

The interface heat flux obtained from the initial solution is then applied as load for the structural problem. The converged coupled solution is again obtained after 4 inter-field coupling iterations, but the main variations are confirmed to stand out after the first coupling. Table 5.4.1.1 exemplifies this fact for the 10° case.

Table 5.4.1.1. Convergence of the thermal quantities. Full-catalytic surface. $\alpha=10^\circ$.

Iteration	ΔT_{\max}	$\Delta T_{x=0.14\text{m}}$	Δq_{\max}	$\Delta q_{x=0.14\text{m}}$
nc - 1.fc	4.18E+02	1.72E+02	4.20E+05	4.30E+04
1 - 2	3.09E+01	8.25E+00	3.46E+04	2.54E+03
2 - 3	-2.05E+00	-1.00E+00	-2.61E+03	-3.08E+02
3 - 4	9.56E-01	3.90E-01	3.75E+02	2.20E+01

The heat flux loading the surface is notably enhanced, as discussed in the preliminary chapters. Figure 5.4.1.1 helps to understand how influential the recombination effects on a full-catalytic surface are: the heat flux can even triplicate on the fore domain and the increase on the rear surface is still about 50%.

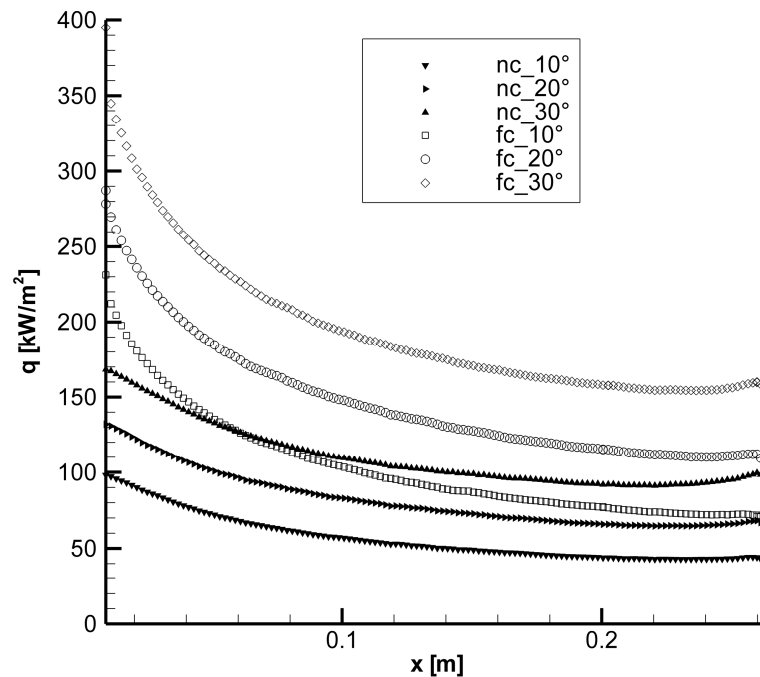


Figure 5.4.1.1. Heat flux distribution on the plate surface. Comparison between non-catalytic and full-catalytic ceramic surface.

The raised thermal load causes a significant increase of the temperature level at the surface. This adds up to 400 K on the front, which corresponds to ca. one third of the non-catalytic maximal values; the difference decreases along with the longitudinal coordinate, but it amounts, however, to approx. 120-150 K on the more downstream region, which corresponds to about 12% more. The differences are remarkable, as pointed out in figure 5.4.1.2.

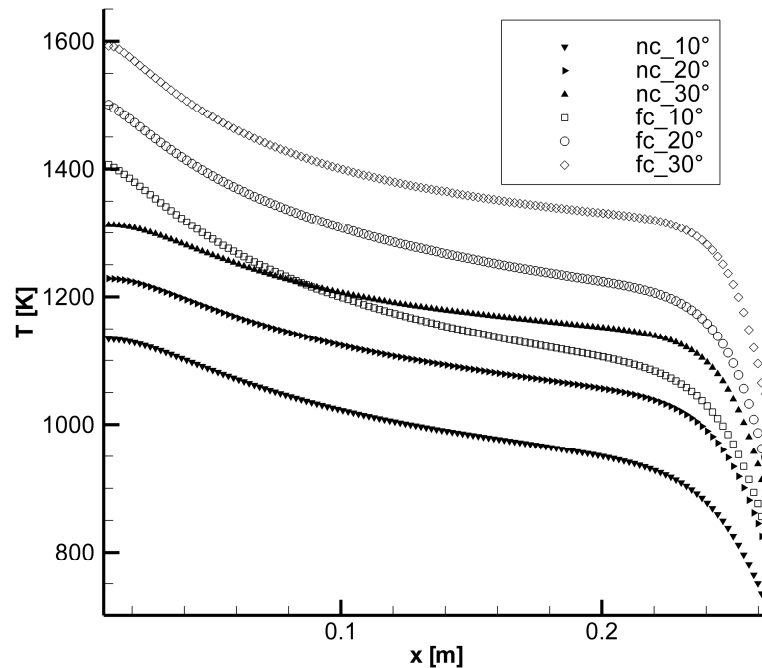


Figure 5.4.1.2. Temperature distribution on the plate surface. Comparison between non-catalytic and full-catalytic ceramic surface.

It is now important to comprehend which relationship between these results and the experimental data exists. Figures 5.4.1.3 to 5.4.1.5 report the comparison with the already available data. Indeed the test results lie in the band between non-catalytic and full-catalytic computations. This indicates a partially catalytic behaviour of the C/C-SiC surface coated by the SiC layer. The investigations by Stewart [22], and in particular the already discussed figure 1.2.1.3, highlight that the recombination coefficients for silicon carbide approach the maximal values just at the temperature levels which the tested plate experiences (although the operating conditions are somewhat different). In fact the experimental data are rather close to the full-catalytic computations for the 20° and 30° configuration, for which the temperature amount is within the range of 1250-1450 K, namely the range at which the recombination coefficient for oxygen in proximity of silicon carbide has a peak. Analogously, the measured temperatures for the 10° case get closer to the full-catalytic results in the fore domain, where the temperature is around 1200-1300 K, but their difference grows downstream, where the temperature level is lower. These facts are pointed out in figures 5.4.1.3 to 5.4.1.5, taken for the sake of depiction only from the test cases 003, 006 and 008.

The differences between experiments and numerical simulations, accounting also for full-catalytic behaviour of the surface, are summarized in tables 5.4.1.2 to 5.4.1.4 for the measurement spots.

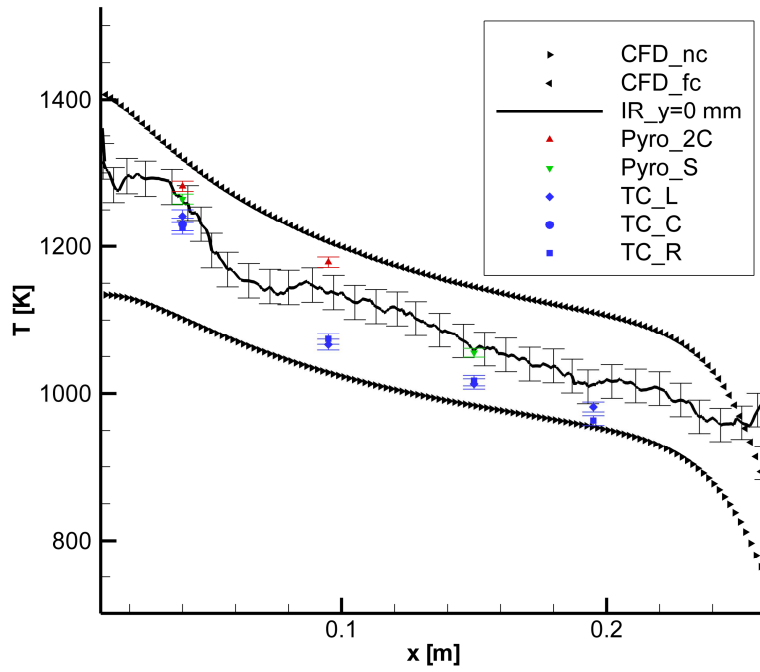


Figure 5.4.1.3. Comparison of the achieved temperatures on the plate. 10° case. Test-003.

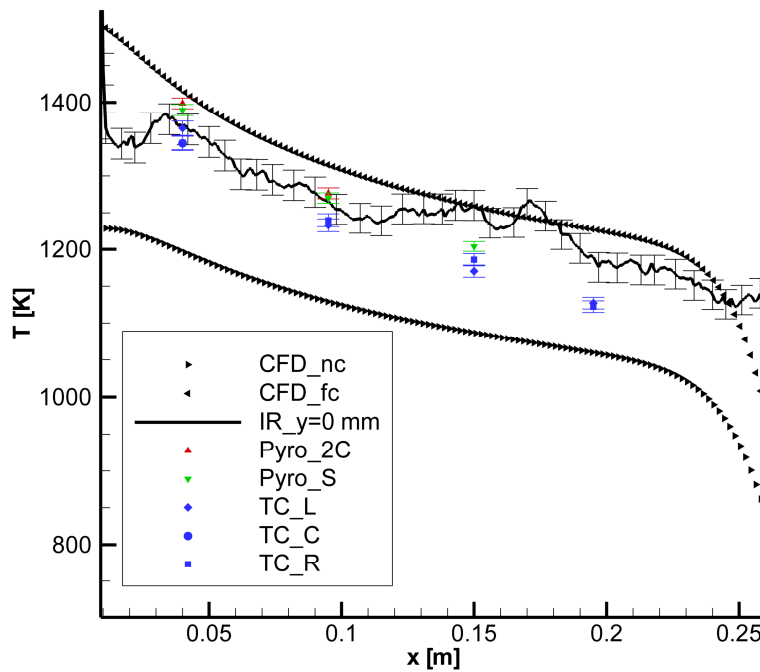


Figure 5.4.1.4. Comparison of the achieved temperatures on the plate. 20° case. Test-006.

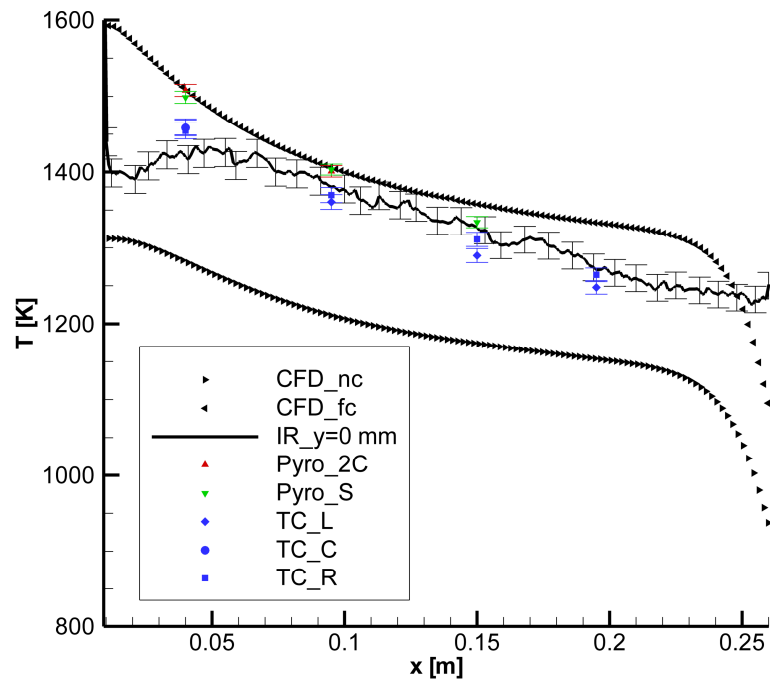


Figure 5.4.1.5. Comparison of the achieved temperatures on the plate. 30° case. Test-008.

 Table 5.4.1.2. Comparison between measured and computed temperatures at the spots. Full-catalytic surface. Temperatures in K. $\alpha=10^\circ$.

x [m]	TC_L	TC_C	TC_R	Pyro 2C	Pyro S	IR $\epsilon=0.83$	CFD_nc	CFD_fc
0.040	1241.24	1229.80	1224.95	1281.87	1264.67	1261.17	1105.81	1305.62
0.095	1066.18	-	1073.99	1178.31	-	1136.76	1029.98	1196.81
0.150	1012.79	-	1017.26	-	1055.07	1058.48	983.71	1138.56
0.195	981.73	-	963.33	-	-	1019.89	947.71	1096.32

 Table 5.4.1.3. Comparison between measured and computed temperatures at the spots. Full-catalytic surface. Temperatures in K. $\alpha=20^\circ$.

x [m]	TC_L	TC_C	TC_R	Pyro 2C	Pyro S	IR $\epsilon=0.83$	CFD_nc	CFD_fc
0.040	1364.73	1344.16	1345.07	1398.69	1389.64	1367.92	1200.78	1410.78
0.095	1232.89	-	1239.78	1276.37	1269.98	1264.98	1130.56	1311.41
0.150	1170.30	-	1185.87	-	1203.90	1259.92	1086.73	1257.76
0.195	1127.14	-	1122.28	-	-	1177.96	1053.78	1220.92

 Table 5.4.1.4. Comparison between measured and computed temperatures at the spots. Full-catalytic surface. Temperatures in K. $\alpha=30^\circ$.

x [m]	TC_L	TC_C	TC_R	Pyro 2C	Pyro S	IR $\epsilon=0.83$	CFD_nc	CFD_fc
0.040	1459.62	1458.24	1454.38	1498.69	1492.01	1419.73	1285.84	1506.88
0.095	1360.70	-	1369.77	1404.40	1404.23	1380.41	1212.52	1406.40
0.150	1289.72	-	1311.24	-	1338.40	1327.17	1173.74	1358.82
0.195	1247.86	-	1264.42	-	-	1261.54	1149.26	1329.16

It must be underlined that the recombination of atomic oxygen is likely to be the principal reason of the increased heat flux at the surface, since at the tested facility flow conditions the mass fraction of atomic oxygen is considerable, whereas the mass fraction of atomic nitrogen is practically negligible (see chapter 4). Oxidation processes at the surface should not be excluded, but their simulation, as well as computations accounting for a partially catalytic behaviour, is not attainable with the currently available tools.

5.4.2 Imperfect thermal contact between horizontal plate and neighbouring components

The possibility of imperfect thermal contact between horizontal plate and insulating material is taken into account by the worst circumstance, namely the absolute absence of heat transfer below the plate. This is treated by means of the straightforward neglect of the KAPYROK block under the plate and by the introduction of an adiabatic wall boundary condition on the ceramic sides in contact with it. The heat load taken from the converged coupled simulations of section 5.2 is applied to the structure, which is modeled as before for all other aspects.

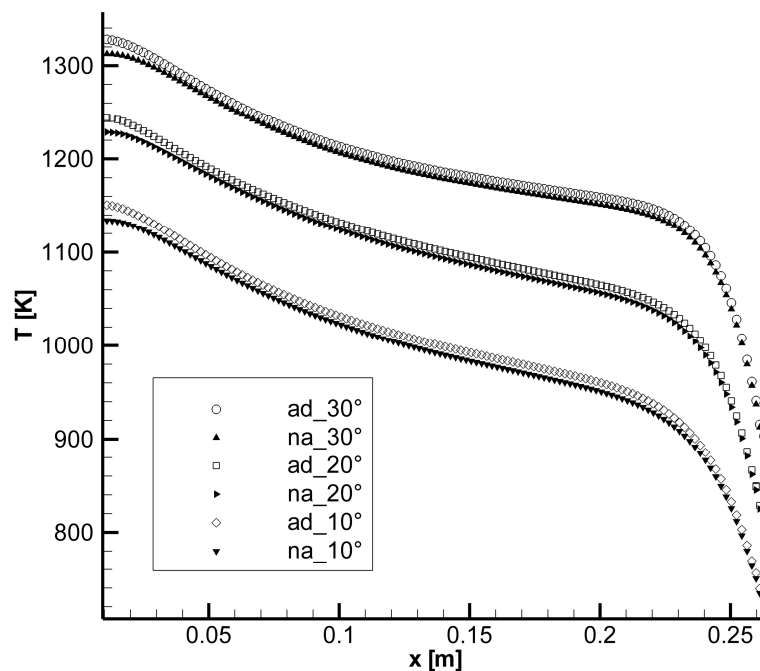


Figure 5.4.2.1. Temperature distribution on the plate surface. Comparison with simulations with adiabatic inferior wall of the plate.

Figure 5.4.2.1 reports the results. The KAPYROK material is confirmed to be an efficient insulating material: the heat conduction inside the block is shown in the

previous investigations to be rather low and the present temperature variation on the plate surface is unsubstantial. It amounts to less than 10 K (less than 1% increase) on almost the whole plate, with maximum values on the front, where it can reach 15 K (which corresponds to about 1.5% more). It can be emphasized that there are no essential quantitative differences owing to the angle of attack.

A possible imperfect thermal contact with the KAPYROK block can be assessed not to represent a fundamental influence on the results. A more remarkable role can be played by an imperfect thermal contact between horizontal and rear plate, since the heat conduction effect in the back have been shown to be significant. The problem is again treated considering the worst circumstance, i.e. neglecting also the complete rear plate. In practice, the horizontal plate is taken into account only, with adiabatic wall boundary conditions on the internal sides.

As explained previously, the heat flux from the converged coupled simulations of section 5.2 loads the structure, and the rest of the numerical set-up is maintained as before. The results are plotted in figure 5.4.2.2. As expectable, the temperature on the back increases in absence of the heat drag through the rear plate. The effect on the temperature distribution on the back is manifest: there is no longer a pronounced negative gradient but a transition to a plateau and even to a slight positive gradient. The increase is comparable to the differences registered between coupled and uncoupled results and reaches even 200-250 K accordingly to the configuration. The relative increase is thus about 25%.

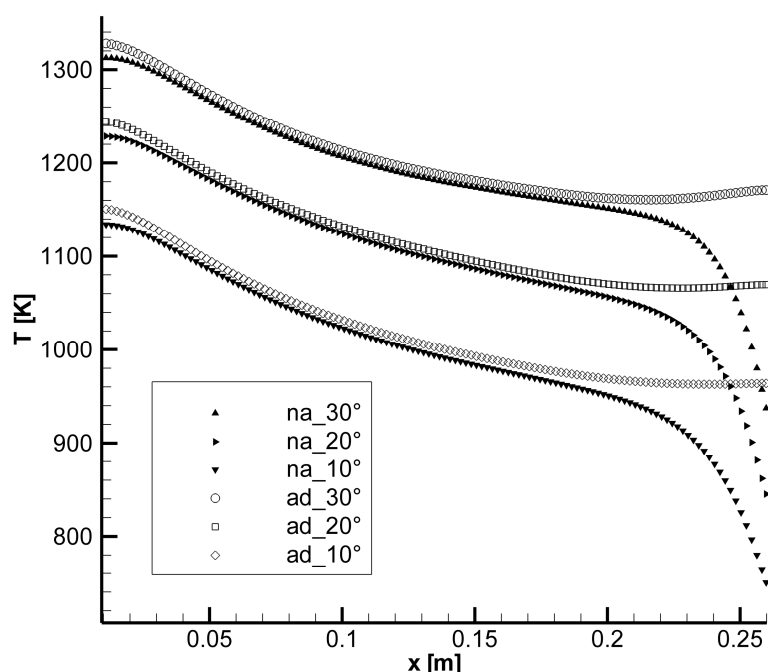


Figure 5.4.2.2. Temperature distribution on the plate surface. Comparison with simulations with adiabatic internal walls.

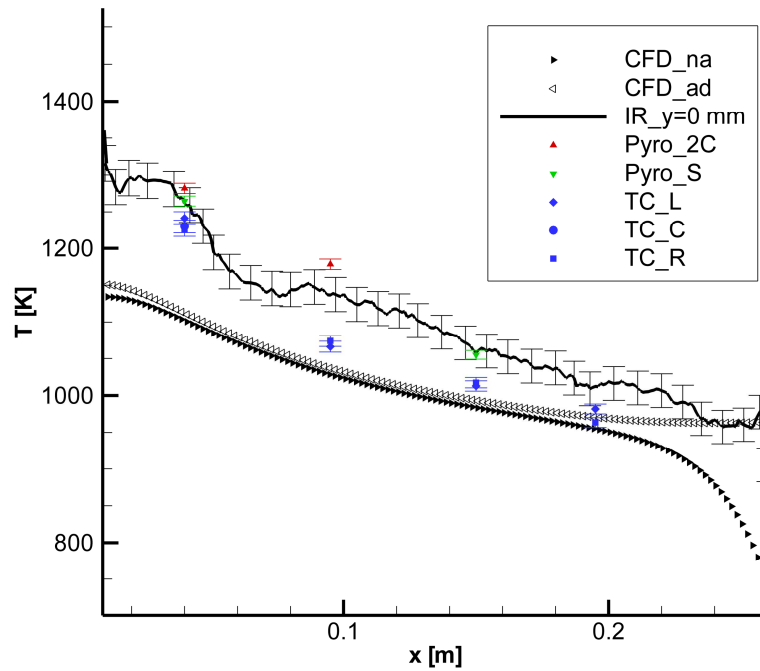


Figure 5.4.2.3. Temperature distribution on the plate surface. Comparison with simulations with adiabatic internal walls. Test-003, $\alpha=10^\circ$.

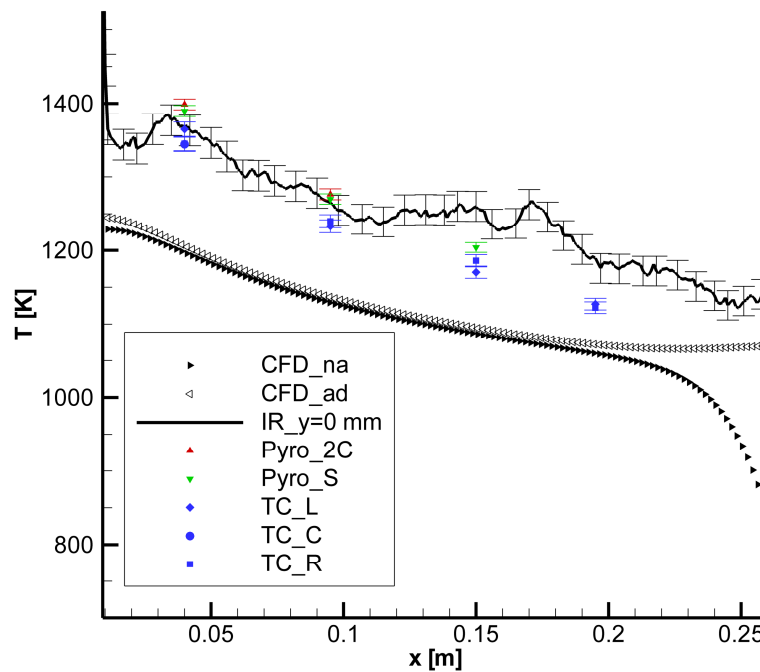


Figure 5.4.2.4. Temperature distribution on the plate surface. Comparison with simulations with adiabatic internal walls. Test-006, $\alpha=20^\circ$.

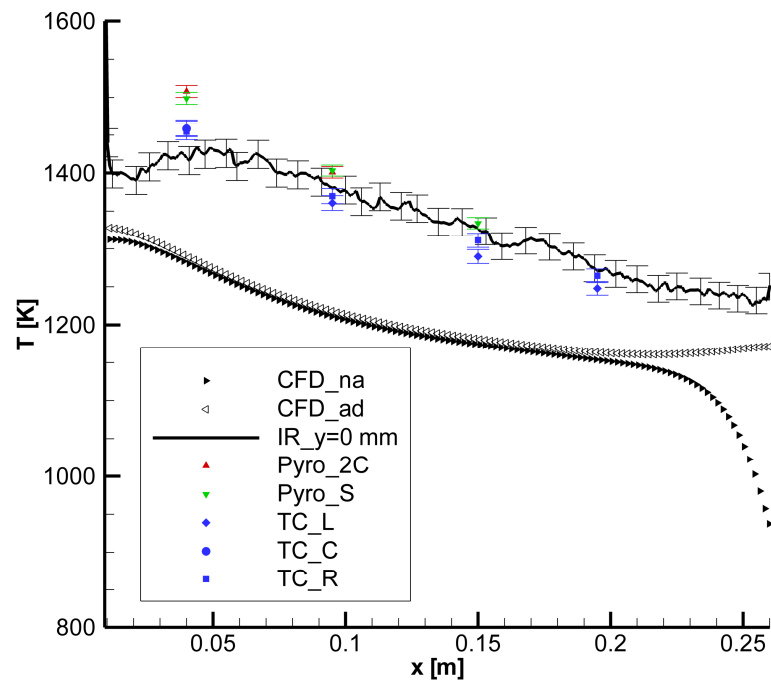


Figure 5.4.2.5. Temperature distribution on the plate surface. Comparison with simulations with adiabatic internal walls. Test-008, $\alpha=30^\circ$.

As displayed in figures 5.4.2.3 to 5.4.2.5, the temperature trend on the rear domain becomes in this way more similar to the experimental results. An imperfect thermal contact between the plates can therefore represent a further aspect which affects the concordance with the computations.

Chapter 6

Conclusions and final remarks

The present work has been focused on the study of the thermal fluid-structure interaction, which involves a spacecraft experiencing high-enthalpy flow conditions. A coupling methodology, which makes use of numerical tools for accurately predicting the thermal load acting on the body surface, represents a fundamental instrument for the design of a spacecraft. Numerical simulations, capable of adequately reproducing the intense fluid-structure interaction occurring at such flow conditions, offer the possibility of an extensive examination of different configurations and of a sensitivity analysis, which would not be available otherwise – or only with extraordinary costs. The correct evaluation of the surface thermal load allows the use of reliable design criteria, which no longer have the necessity of considerable safety margins, with the consequent decrease of the structural mass together with an increase of the payload as well as a reduction of the costs.

Before numerical tools actually come into use, the validation of the coupling procedure and the proof of the exactness of their results are necessary prerequisites. This degree thesis takes its place in this perspective. The application of a suitable physical model capable of appropriately reproducing the fluid-structure interaction phenomena which involve the structure surface, the analysis of the coupled simulations results and their comparison with experiments have been focal points of this work.

The simulation of the flowfield has been performed by means of the TAU code developed at DLR, whereas the structural response has been calculated with the commercial software ANSYS. Coupled simulations have been proved to more effectively reproduce the distributions of the thermal quantities on the surface of the investigated flat-plate model, which is made of the ceramic material C/C-SiC. Temperature peaks have shown to be remarkably smoothed and the temperature distribution to be rather mitigated in general.

Different flow models for the high-temperature gas and for the stream conditions have been numerically investigated in order to understand their impact on the surface quantities, which has been demonstrated to be generally not significant.

For the collection of the experimental data, the model has been tested in the high-enthalpy facility L3K of DLR in Cologne, which enables reaching a steady-state of the temperature distribution on the surface thanks to its rather

long running-time. The instrumentation for the temperature measurement has comprehended thermocouples and optical devices, namely pyrometers and an IR-camera. The tests results have shown to be very good reproducible, the thermal quantities to reach in general a steady state at the surface and to be rather uniform in lateral direction for a considerable portion of the model. Bi-dimensional steady simulations have been therefore retained satisfactory for the numerical investigation of the concerned problem, at least for the model symmetry axis.

The computations have been demonstrated to properly capture the temperature trend on the objective surface. The temperature slope along with the longitudinal coordinate is effectively reproduced, although the temperature values are underpredicted. Some phenomena can be indicated as the reasons of such results: the catalytic behaviour of the ceramic surface, the oxidation reactions at the surface and the imperfect thermal contact between the model components. Further numerical investigations have been conducted in order to understand the impact of a full-catalytic surface and of an absolutely imperfect contact between the components. In particular, the results in the full-catalytic case lie above the experimental measurements, pointing out a partially catalytic behaviour of the ceramics at such temperature levels, while an imperfect thermal contact is likely to be the reason of the temperature underprediction on the rear surface.

Future developments should concern:

- the extensive study of the aerothermodynamic effects occurring at the surface, accounting for the partially catalytic behaviour of C/C-SiC and for possible oxidation processes;
- three-dimensional computations, capable to capture the three-dimensional effects at the model edges;
- the accurate reproduction of the transfer of the thermal quantities at the connection surfaces between the model components;
- the unsteady simulation of the structural response (whereas the flow solution can reasonably be maintained as quasi-steady). The data of the thermocouples integrated inside the model can additionally be used for the validation.

Since the investigated configurations have been tested at only one facility flow condition, other comparisons should be planned for different flow states, with the final aim of validating the numerical environment with real flight experiments.

Appendix A

Properties of the used materials

Table A.1. Principal material properties of C/C-SiC in dependence on the temperature (from ref. [30]).

C/C-SiC	$T=273$ K	$T=473$ K	$T=873$ K	$T=1273$ K	$T=1673$ K	$T=2273$ K
κ_{\perp} [W/(m K)]	11.2	11.2	11.2	10.9	10.4	10.0
κ_{\parallel} [W/(m K)]	18.0	19.3	19.5	19.6	19.5	19.2
c_p [J/(kg K)]	748	1211	1604	1720	1780	1800
ρ [kg/m ³]	1800	1800	1800	1800	1800	1800
ε	0.88	0.89	0.90	0.90	0.89	0.88

Table A.2. Principal material properties of KAPYROK material in dependence on the temperature (from ref. [30]).

KAPYROK	$T=273$ K	$T=473$ K	$T=873$ K	$T=1273$ K	$T=1673$ K	$T=2273$ K
κ [W/(m K)]	0.10	0.10	0.12	0.15	0.23	0.30
c_p [J/(kg K)]	1250	1250	1250	1250	1250	1250
ρ [kg/m ³]	400	400	400	400	400	400
ε	0.95	0.95	0.95	0.95	0.95	0.95

Table A.3. Principal material properties of used copper and stainless steel, considered temperature-independent (from ref. [30]).

	Copper	Stainless steel
κ [W/(m K)]	400	15
c_p [J/(kg K)]	385	500
ρ [kg/m ³]	8900	7900
ε	0.5	0.3

Appendix B

Chemical model

Table B.1. Reaction rates. Gupta model [77]. Reaction rate k defined as:

$$k(T) = aT^b e^{\left(\frac{-c}{T}\right)}. \quad (\text{B.1})$$

$2\text{N}_2 = \text{N}_2 + 2\text{N}$	<i>a</i>	<i>b</i>	<i>c</i>
Forward rate constants	3.72E+15	-1.6	113000
Backward rate constants	2.06E+08	-1.6	0
$\text{N}_2 + \text{O}_2 = \text{O}_2 + 2\text{N}$	<i>a</i>	<i>b</i>	<i>c</i>
Forward rate constants	3.72E+15	-1.6	113000
Backward rate constants	2.06E+08	-1.6	0
$\text{N}_2 + \text{NO} = \text{NO} + 2\text{N}$	<i>a</i>	<i>b</i>	<i>c</i>
Forward rate constants	3.72E+15	-1.6	113000
Backward rate constants	2.06E+08	-1.6	0
$\text{N}_2 + \text{N} = 3\text{N}$	<i>a</i>	<i>b</i>	<i>c</i>
Forward rate constants	1.11E+16	-1.6	113000
Backward rate constants	6.19E+08	-1.6	0
$\text{N}_2 + \text{O} = 2\text{N} + \text{O}$	<i>a</i>	<i>b</i>	<i>c</i>
Forward rate constants	1.11E+16	-1.6	113000
Backward rate constants	6.19E+08	-1.6	0
$\text{N}_2 + \text{O}_2 = \text{N}_2 + 2\text{O}$	<i>a</i>	<i>b</i>	<i>c</i>
Forward rate constants	2.76E+13	-1.0	59500
Backward rate constants	2.30E+04	-0.5	0
$2\text{O}_2 = \text{O}_2 + 2\text{O}$	<i>a</i>	<i>b</i>	<i>c</i>
Forward rate constants	2.76E+13	-1.0	59500
Backward rate constants	2.30E+04	-0.5	0
$\text{O}_2 + \text{NO} = \text{NO} + 2\text{O}$	<i>a</i>	<i>b</i>	<i>c</i>
Forward rate constants	2.76E+13	-1.0	59500
Backward rate constants	2.30E+04	-0.5	0
$\text{N} + \text{O}_2 = \text{N} + 2\text{O}$	<i>a</i>	<i>b</i>	<i>c</i>
Forward rate constants	8.25E+13	-1.0	59500
Backward rate constants	6.88E+04	-0.5	0

$O_2 + O = 3O$	<i>a</i>	<i>b</i>	<i>c</i>
Forward rate constants	8.25E+13	-1.0	59500
Backward rate constants	6.88E+04	-0.5	0
$N_2 + NO = N_2 + N + O$	<i>a</i>	<i>b</i>	<i>c</i>
Forward rate constants	2.31E+11	-0.5	75500
Backward rate constants	5.77E+04	-0.5	0
$O_2 + NO = O_2 + N + O$	<i>a</i>	<i>b</i>	<i>c</i>
Forward rate constants	2.31E+11	-0.5	75500
Backward rate constants	5.77E+04	-0.5	0
$2NO = NO + N + O$	<i>a</i>	<i>b</i>	<i>c</i>
Forward rate constants	2.31E+11	-0.5	75500
Backward rate constants	5.77E+04	-0.5	0
$NO + N = 2N + O$	<i>a</i>	<i>b</i>	<i>c</i>
Forward rate constants	4.62E+11	-0.5	75500
Backward rate constants	1.15E+05	-0.5	0
$NO + O = N + 2O$	<i>a</i>	<i>b</i>	<i>c</i>
Forward rate constants	4.62E+11	-0.5	75500
Backward rate constants	1.15E+05	-0.5	0
$NO + O = O_2 + N$	<i>a</i>	<i>b</i>	<i>c</i>
Forward rate constants	1.60E+03	1.29	19700
Backward rate constants	4.81E+05	0.79	3700
$N_2 + O = NO + N$	<i>a</i>	<i>b</i>	<i>c</i>
Forward rate constants	3.19E+07	0.1	37500
Backward rate constants	7.09E+06	0.1	0

Appendix C

Geometry of the considered models

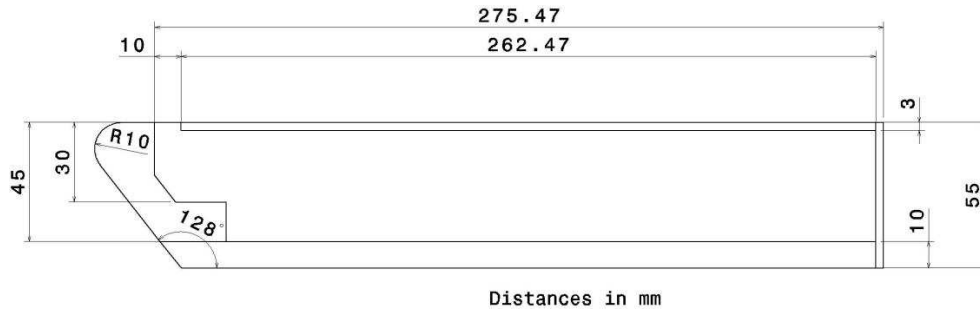


Figure C.1. Bi-dimensional model for the simulations of chapter 4.

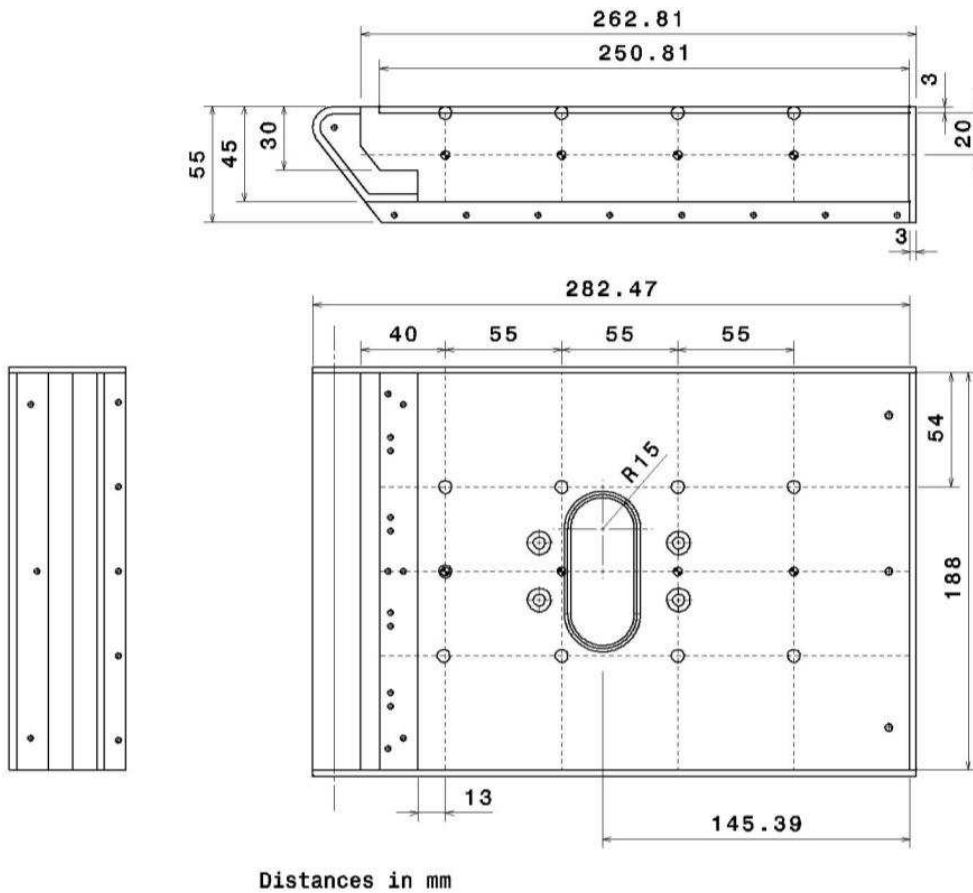


Figure C.2. Investigated flat-plate model. The measurement spots are also shown.

Nomenclature

Latin symbols

c_p	Specific heat capacity at constant pressure	J/(kg K)
D	Multi-component diffusion coefficient	m ² /s
E	Total energy per unit mass	J/kg
h	Specific enthalpy per unit mass	J/kg
k	Reaction rate	mol/(m ³ s)
Kn	Knudsen number	-
L	Representative length of the flowfield	m
M	Molar mass	kg/mol
	Specific radiance	W/m ³
Ma	Mach number	-
N	Number of atoms	-
p	Pressure	Pa
Pr	Prandtl number	-
Q	Heat flux	W
Q_B	Inner energy source term	W/m ³
q	Specific heat flux per unit surface	W/m ²
R	Specific gas constant	J/(kg K)
Re	Reynolds number	-
S	Surface	m ²
Sc	Schmidt number	-
T	Temperature	K
t	Time	s
u, v, w	Velocity components	m/s
V	Volume	m ³
x, y, z	Spatial Cartesian coordinates	m

Greek symbols

α	Absorptivity	-
	Angle of attack	°
	Mass fraction	-
Γ	Domain interface	m ²
γ	Recombination coefficient	-
	Specific heat ratio	-
Δ	Difference	-
δ	Virtual variation	-

Nomenclature

ε	Emissivity	-
κ	Heat conductivity	W/(m K)
λ	Molecular mean free-path length	m
	Wavelength	m
μ	Dynamic viscosity	Pa s
ρ	Mass density	kg/m ³
σ	Standard deviation of temperature distribution	K
τ	Characteristic time	s
	Transmittance	-
Φ	Relaxation parameter	-
ω_s	Mass source term	kg/m ³

Tensors, matrices and vectors

B	Shape function gradient matrix
C	Heat capacity matrix
F	Flux tensor
I	Identity matrix
K	Heat conductivity matrix
Λ	Heat conductivity tensor
N	Shape function matrix
n	Local normal to the surface
P	Stress tensor
Q	Finite element heat fluxes vector
	Source vector
q	Heat fluxes vector
T	Nodal temperatures vector
U	Conservative flow quantities vector
u	Velocity vector

Indices

$()$	Time derivative
0	Reservoir
	Zero point
//	Parallel
\perp	Perpendicular
∞	Free stream conditions
	Inflow conditions
avg	Averaged value
<i>b</i>	Black body
<i>c</i>	Convective

ca	Calibration
chem	Chemical
di	Discrimination
el	Electronic
Eul	Inviscid
F	Fluid
in	Instrument
IR	Infrared camera
λ	Spectral
max	Maximal
min	Minimal
N	Normal
n	External normal
p	Pixel
R	Recombination
re	Reproducibility
ref	Reference
rot	Rotational
r	Radiative
S	Structure
s	Species
T	Total
tr	Translational
u	Background
v	Viscous
vib	Vibrational
w	Wall

Constants

c_0	Light speed in vacuum	$2.99792458 \cdot 10^8$ m/s
h	Planck constant	$6.62606896 \cdot 10^{-34}$ J s
k	Boltzmann constant	$1.3806504 \cdot 10^{-23}$ J/K
\mathfrak{R}	Universal gas constant	8.314472 J/(K mol)
S	Sutherland constant	110.4 K
σ	Stefan-Boltzmann constant	$5.6704 \cdot 10^{-8}$ W/(m ² K ⁴)

Abbreviations

2C-2000	Two-colour pyrometer, temperature range of 800-2000°C
2C-3000	Two-colour pyrometer, temperature range of 900-3000°C
4coupled	Coupled solution after 4 inter-field iterations

Nomenclature

ad	Adiabatic wall
fc	Full-catalytic wall
mv	Measured value
na	Non-adiabatic wall
nc	Non-catalytic wall
pg	Frozen flow (adapted perfect gas properties)
radeq	Uncoupled solution
rg	Range
tggf	Nozzle flow in chemical non-equilibrium
tngg	Model flow in thermochemical non-equilibrium
tnggf	Nozzle flow in thermochemical non-equilibrium
TC	Thermocouple
S-2000	Spectral pyrometer, temperature range of 900-2000°C
S-3000	Spectral pyrometer, temperature range of 900-3000°C

Acronyms

Al	Aluminum
Al ₂ O ₃	Aluminum oxide
C	Carbon
CCD	Charge-coupled device
C/C-SiC	Carbon fiber-reinforced silicon-carbide
CFD	Computational fluid dynamics
CMC	Ceramic matrix composite
CO	Carbon monoxide
Cr	Chrome
CVD	Chemical vapor deposition
DLR	Deutsches Zentrum für Luft- und Raumfahrt e.V.
FEM	Finite element method
FPA	Focal Plain Array
IR	Infrared
N	Nitrogen
Ni	Nickel
NiCr	Nickel-chromium
NO	Nitric oxide
O	Oxygen
Si	Silicon
SiC	Silicon carbide
SiO	Silicon oxide
SiO ₂	Silicon dioxide
SFB	Sonderforschungsbereich
TPS	Thermal protection system

Bibliography

- [1] J.J. Bertin, Hypersonic aerothermodynamics, AIAA Educational Series, Reston, Virginia, 1994. – ISBN 1-56347-036-5.
- [2] E.H. Hirschel, Heat load as a key problem of hypersonic flight, *Zeitschrift für Flugwissenschaften und Weltraumforschung* 16 (1992), pp. 349-356.
- [3] J.D. Anderson, Hypersonic and high temperature gas dynamics, AIAA Educational Series, Reston, Virginia, 2000. – ISBN 1-56347-459-X.
- [4] E. Messerschmidt, S. Fasoulas, Raumfahrtssysteme, Springer-Verlag, Berlin-Heidelberg, Germany, 2000. – ISBN 3-540-66803-9.
- [5] Apollo Program summary report, NASA, Lyndon B. Johnson Space Center, Houston, Texas, April 1975.
- [6] W.E. Neuenschwander, D.U. McBride, G.A. Armour, Shuttle TPS thermal performance and analysis methodology, in: *Shuttle Performance: Lessons Learned*, Pt. 2, NASA, Langley Research Center, Hampton, Virginia, 1983, pp. 1025-1064.
- [7] V.P. Timoshenko, Design and experimental development of the BURAN thermal protection, in: G.E. Lozino-Lozinsky, A.G. Bratukhin (eds.), *Aerospace systems: Book of technical papers*, Publishing House of Moscow Aviation Institute, Moscow, Russia, 1997, pp. 123-136.
- [8] T.J. Horvath, S.A. Berry, N.R. Merski, S.M. Fitzgerald, X-38 Experimental Aerothermodynamics, AIAA Paper 2000-2685, 2000.
- [9] H. Hald, Faserkeramiken für heiße Strukturen von Wiedereintrittfahrzeugen – Simulation, Test und Vergleich mit experimentellen Flugdaten, University of Stuttgart, PhD Thesis, 2001. – ISSN 1434-8454, DLR-FB-2001-17.
- [10] G. Palmer, W.D. Henline, D.R. Olynick, F.S. Milos, High-fidelity thermal protection system sizing of reusable launch vehicle, *Journal of Spacecraft and Rockets*, Vol. 34, No.5, September-October 1997, pp. 577-583.

Bibliography

- [11] A. Gülhan, B. Esser, U. Koch, Experimental Investigation of Reentry Vehicle Aerothermodynamic Problems in Arc-Heated Facilities, *Journal of Spacecraft and Rockets*, Vol. 38, No.2, March-April 2001, pp. 199-206.
- [12] A. Gülhan, Vorlesungsunterlagen, Strömungsfragen der Raumfahrt I, RWTH, Aachen, Germany, 2009.
- [13] G. Koppenwallner, Aerothermodynamik – Ein Schlüssel zu neuen Transportgeräten der Luft- und Raumfahrt, *Zeitschrift für Flugwissenschaften und Weltraumforschung* 12 (1988), pp. 6-18.
- [14] E.R. van Driest, Investigation of Laminar Boundary Layer in Compressible Flows using the Crocco Method, NACA TN 2597, Washington, D.C., 1952.
- [15] Special course on three-dimensional supersonic/hypersonic flows including separation, AGARD Report 764, January 1990.
- [16] B. Esser, Die Zustandgrößen im Stoßwellenkanal als Ergebnisse eines exakten Riemannlösers, RWTH Aachen, PhD Thesis, 1996.
- [17] G. Koppenwallner, H. Legge, Drag of bodies in rarified hypersonic flow, in: J.N. Moss, C.D. Scott (eds.), *Thermophysical aspects of re-entry flows*, Progress in Astronautics and Aeronautics Series, Vol. 103, AIAA, Reston, Virginia, 1986, pp. 44-58.
- [18] C.H. Lewis, E.G. Burgess, Charts of normal shock wave properties in imperfect air, AEDRTDR-64-43, Arnold Engineering Development Center, Arnold Air Force Base, Manchester, Tennessee, March 1964.
- [19] G. Hilfer, Experimentelle und theoretische Beiträge zur Plasma Wand-Wechselwirkung keramischer Hitzeschutzmaterialien unter Wiedereintrittsbedingungen, University of Stuttgart, PhD Thesis, Shaker Verlag, Aachen, 2000. – ISBN 3-8265-7118-5.
- [20] T. Laux, Untersuchungen zur Hochtemperaturoxidation von Siliziumkarbid in Plasmaströmungen, University of Stuttgart, PhD Thesis, Shaker Verlag, Aachen, 2004. – ISBN 3-8322-3128-5.
- [21] T. Stöckle, Untersuchung der Oberflächenkatalyzität metallischer und keramischer Werkstoffe in Hochenthalpieströmungen, University of Stuttgart, PhD Thesis, 2000. – ISBN 3-18-359605-9.

- [22] D.A. Stewart, Determination of Surface Catalytic Efficiency for Thermal Protection Materials - Room Temperature to Their Upper Use Limit, AIAA Paper 96-1863, in: *31st AIAA Thermophysics Conference*, New Orleans, Nevada, June 1996.
- [23] C.L. Jaeck, Analysis of Pressure and Heat Transfer Tests on Surface Roughness Elements with Laminar and Turbulent Boundary Layers, NASA CR 537, Washington, D.C., 1966.
- [24] S.P. Schneider, Hypersonic laminar–turbulent transition on circular cones and scramjet forebodies, *Progress in Aerospace Sciences* 40 (2004), pp. 1–50.
- [25] A.L. Nagel, H.D. Fitzsimmons, L.B. Doyle, Analysis of Hypersonic Pressure and Heat Transfer Tests on Delta Wings with Laminar and Turbulent Boundary Layers, NASA CR 535, Washington, D.C., 1966.
- [26] M. Haupt, H. Kossira, Analysis of Structures in Hypersonic Fluid Flow Including the Fluid-Structure-Interaction, in: *European Conference on Spacecraft Structures, Materials and Mechanical Testing*, Brunswick, Germany, 1999.
- [27] A. Gülhan, B. Esser, Arc-Heated Facilities as a Tool to study Aerothermodynamic Problems of Reentry Vehicles, in: F.K. Lu, D.E. Marren (eds.), *Advanced Hypersonic Test Facilities*, Progress in Astronautics and Aeronautics Series, Vol. 198, AIAA, Reston, Virginia, 2002, pp. 375-403. – ISBN 1-56347-541-3.
- [28] H.H. Hamilton, J.D. Dearing, Effect of Hinge-Line Bleed on Heat Transfer and Pressure Distribution over a Wedge-Flap Combination at Mach 10.4, NASA TN D 4686, Washington, D.C., 1968.
- [29] J.D. Dearing, H.H. Hamilton, Heat Transfer and Pressure Distribution inside the Hinge-Line Gap of a Wedge-Flap Combination at Mach 10.4, NASA TN D 4911, Washington, D.C., 1968.
- [30] R. Schäfer, Thermisch-mechanisches Verhalten heißer Strukturen in der Wechselwirkung mit einem umströmenden Fluid, University of Stuttgart, PhD Thesis, 2005. – ISSN 1434-8454, DLR-FB-2005-02.

Bibliography

- [31] A. Mack, Analyse von heißen Hyperschallströmungen um Steuerklappen mit Fluid-Struktur Wechselwirkung, Technical University of Brunswick, PhD Thesis, 2005. – ISSN 1434-8454, DLR-FB-2005-23.
- [32] B. Esser, A. Gülhan, R. Schäfer, Experimental Investigation of Thermal Fluid-Structure Interaction in High-Enthalpy Flow, in: *Fifth European Symposium on Aerothermodynamics for Space Vehicles*, Cologne, Germany, November 2004.
- [33] S.I. Hong, W.E. Neuenschwander, Internal Convective Heat Transfer Mechanism in Reentry Space Vehicles, AIAA Paper 91-1440, in: *AIAA 26th Thermophysics Conference*, Honolulu, Hawaii, June 1991.
- [34] F. Infed, F. Olawsky, M. Auweter-Kurz, Stationary Coupling of 3D Hypersonic Non-equilibrium Flows and TPS Structures with Uranus, AIAA Paper 2003-3984, 2003.
- [35] E.H. Hirschel, Aerothermodynamic Phenomena and the Design of Atmospheric Hypersonic Airplane, in: *Third Joint Europe/U.S. Short Course in Hypersonics*, Aachen, Germany, October 1990.
- [36] P. Kolodziej, Strategies and Approaches to TPS Design, RTO AVT Lecture Series on Critical Technologies for Hypersonic Vehicle Development, Von Karman Institute, Rhode-St-Genèse, Belgium, May 2004.
- [37] N.K. Hiester, C.F. Clark, Comparative Evaluation of Ablating Materials in Plasma Jets, SRI Rep. No. 18, 1968.
- [38] K.A. Heufer, H. Olivier, Experimental Study of Active Cooling in 8 Laminar Hypersonic Flows, in: A. Gülhan (ed.), *RESPACE – Key Technologies for Reusable Space Systems*, Springer-Verlag, Berlin-Heidelberg, Germany, 2008, pp. 132-150.
- [39] B. Esser, A. Gülhan, Qualification of Active Cooling Concepts in Ground Facilities, in: A. Gülhan (ed.), *RESPACE – Key Technologies for Reusable Space Systems*, Springer-Verlag, Berlin-Heidelberg, Germany, 2008, pp. 104-131.
- [40] W.H. Stillwell, X-15 Research Results with a Selected Bibliography, NASA SP-60, Washington, D.C., 1964.

- [41] W. Krenkel, *Keramische Faserverbundwerkstoffe*, Wiley-VCH Verlag, Weinheim, Germany, 2003. – ISBN 3-527-30529-7.
- [42] H. Weihs, H. Hald, T. Reimer, I. Fischer, Development of a CMC Nose Cap for X-38, in: *52nd International Astronautical Congress IAF*, Toulouse, France, October 2001.
- [43] H. Pfeiffer, Ceramic Body Flap for X-38 and CRV, in: *2nd International Symposium: Atmospheric Reentry Vehicles and Systems*, Arcachon, France, March 2001.
- [44] W. Krenkel, Entwicklung eines kostengünstigen Verfahrens zur Herstellung von Bauteilen aus keramischen Verbundwerkstoffen, University of Stuttgart, PhD Thesis, 2000. – ISSN 1434-8454, DLR-FB-2000-04.
- [45] H.-P. Maier, Thermomechanisches Verhalten von C/C-SiC, Materialkennwerte-Ermittlung, Teilprojekt B2b, in: *Hochtemperaturprobleme rückkehrfähiger Raumtransportsysteme, Arbeits- und Ergebnisbericht des SFB 259*, SFB 259, University of Stuttgart, 2001.
- [46] R. Brandt, G. Neuer, E. Schreiber, Thermisches Verhalten von C/C-SiC, Teilprojekt B3, in: *Hochtemperaturprobleme rückkehrfähiger Raumtransportsysteme, Arbeits- und Ergebnisbericht des SFB 259*, SFB 259, University of Stuttgart, 2001.
- [47] M. Friess, T. Ullmann, E. Schreiber, Materialentwicklung und Herstellungstechnologie für C/C-SiC Bauteile, Teilprojekt B1, in: *Hochtemperaturprobleme rückkehrfähiger Raumtransportsysteme, Arbeits- und Ergebnisbericht des SFB 259*, SFB 259, University of Stuttgart, 2001.
- [48] E.A. Thornton, *Thermal Structures for Aerospace Application*, AIAA Educational Series, Reston, Virginia, 1996. – ISBN 1-56347-190-6.
- [49] P. Perrier, Concepts in Hypersonic Aircraft, in: J.J. Bertin, J. Periaux, J. Ballmann (eds.), *Advances in Hypersonics*, Vol. 1: *Defining the hypersonic environment*, Birkhäuser Boston, Cambridge, Massachusetts, 1992, pp. 40-71. – ISBN 3-7643-3639-0.

Bibliography

- [50] K. Hozumi, Y. Yamamoto, A study for prediction of flight aerodynamic heating using HYFLEX flight and wind tunnel data, AIAA Paper 2001-1826, in: *AIAA/NAL-NASDA-ISAS 10th International Space Planets and Hypersonic Systems and Technology Conference*, Kyoto, Japan, April 2001.
- [51] B.R. Hollis, T.J. Horvath, S.A. Berry, H.H. Hamilton II, R.A. Thompson, S.J. Alter, X-33 Computational Aeroheating Predictions and Comparisons with Experimental Data, *Journal of Spacecraft and Rockets*, Vol. 38, No. 5, September–October 2001, pp. 658-669.
- [52] K. Fujii, S. Watanabe, T. Kurotaki, M. Shirouzu, Aerodynamic Heating Measurements on Nose and Elevon of Hypersonic Flight Experiment Vehicle, *Journal of Spacecraft and Rockets*, Vol. 38, No. 1, January-February 2001, pp. 8-14.
- [53] J.M.A. Longo, Aerothermodynamics – A critical review at DLR, *Aerospace Science and Technology* 7 (2003), pp. 429-438.
- [54] E.H. Hirschel, Aerothermodynamic Phenomena and the Design of Atmospheric Hypersonic Airplanes, in: J.J. Bertin, J. Periaux, J. Ballmann (eds.), *Advances in Hypersonics*, Vol. 1: *Defining the hypersonic environment*, Birkhäuser Boston, Cambridge, Massachusetts, 1992, pp. 1-39. – ISBN 3-7643-3639-0.
- [55] F. Scortecci, F. Paganucci, L. D’Agostino, Experimental Investigation of Shock Wave/Boundary Layer Interactions over an Artificially Heated Model in Hypersonic Flow, AIAA Paper 98-1571, 1998.
- [56] Committee on Hypersonic Technology for Military Application, *Hypersonic Technology for Military Application*, National Academy Press, Washington, D.C., 1989.
- [57] Committee to Assess Current Capabilities and Future Directions in Computational Fluid Dynamics, *Current Capabilities and Future Directions in Computational Fluid Dynamics*, National Academy Press, Washington, D.C., 1986.
- [58] C.A. Felippa, K.C. Park, Synthesis Tools for Structural Dynamics and Partitioned Analysis of Coupled Systems, in: A. Ibrahimbegović, B. Brank (eds.), *Engineering Structures under Extreme Conditions*, NATO Series

III: Computer and System Sciences, Vol. 194, IOS Press, Amsterdam, Netherlands, 2005, pp. 50-110. – ISBN 1-58603-479-0.

- [59] A. Quarteroni, A. Valli, Domain decomposition methods for partial differential equations, Oxford University Press, Oxford, U.K., 1999. – ISBN 1-56347-036-5.
- [60] D.R. Olynick, Trajectory Based TPS Sizing for an X-33 Winged Vehicle Concept, AIAA Paper 97-0276, in: *35th Aerospace Sciences Meeting and Exhibit*, Reno, Nevada, January 1997.
- [61] R. Löhner, C. Yang, J. Cebral, Fluid-Structure Interaction Using a Loose Coupling Algorithm and Adaptive Unstructured Grids, AIAA Paper 95-2259, in: *26th AIAA Fluid Dynamics Conference*, San Diego, California, June 1995.
- [62] J. Blazek, Conservative Coupling Algorithm for Structured-Unstructured Grid Interfaces, AIAA Paper 2002-2974, 2002.
- [63] J. Cebral, R. Löhner, Conservative Load Projection and Tracking for Fluid-Structure Problems, AIAA Paper 96-0797, in: *34th Aerospace Sciences Meeting and Exhibit*, Reno, Nevada, January 1996.
- [64] B. Esser, A. Gülhan, Thermal Fluid-Structure Interaction in Different Atmospheres, ESA SP-631, in: *5th European Workshop on Thermal Protection Systems and Hot Structures*, Noordwijk, Netherlands, August 2006.
- [65] S.A. Berry, T.J. Horvath, R.P. Lillard, B.S. Kirk, A.M. Cassady, Aerothermal Testing for Project Orion Crew Exploration Vehicle, AIAA Paper 2009-3842, in: *41st Thermophysics Conference*, San Antonio, Texas, June 2009.
- [66] ANSYS, Inc., ANSYS User's Manual, 2007.
- [67] T.-R. Hsu, The Finite Element Method in Thermomechanics, Allen and Unwin, Winchester, Massachusetts, 1986. – ISBN 0-04-620013-4.
- [68] C.B. Zienkiewicz, R.L. Taylor, The Finite Element Method, Vol. 1: The Basis, Butterworth-Heinemann, Oxford, U.K., 2000. – ISBN 0-7506-5049-4.

Bibliography

- [69] F.P. Incropera, D.P. DeWitt, *Fundamentals of Heat and Mass Transfer*, John Wiley and Sons, New York, New York, 1996. – ISBN 0-471-30460-3.
- [70] R. Siegel, J.R. Howell, J. Lohrengel, *Wärmeübertragung durch Strahlung*, Vol. 2: Strahlungsaustausch zwischen Oberflächen und in Umhüllungen, Springer-Verlag, Berlin-Heidelberg, Germany, 1991. – ISBN 3-540-52710-9.
- [71] C.B. Zienkiewicz, R.L. Taylor, *The Finite Element Method*, Vol. 2: Solid Mechanics, Butterworth-Heinemann, Oxford, U.K., 2000. – ISBN 0-7506-5055-9.
- [72] *Technical Documentation of the DLR TAU-Code*, Institute of Aerodynamics and Flow Technology, DLR, Brunswick-Göttingen, Germany, 2004.
- [73] S. Chapman, T.G. Cowling, *The Mathematical Theory of Non-Uniform Gases*, Cambridge University Press, Cambridge, U.K., 1970. – ISBN 0-521-07577-7.
- [74] W.G. Vincenti, C.H. Kruger, *Introduction to Physical Gas Dynamics*, Krieger Publishing Company, Malabar, Florida, 1975. – ISBN 0-882-75309-6.
- [75] H. Schlichting, K. Gersten, *Boundary-Layer Theory*, Springer-Verlag, Berlin-Heidelberg, Germany, 2000. – ISBN 3-540-66270-7.
- [76] C. Park, *On Convergence of Computation of Chemically Reacting Flows*, AIAA Paper 85-0247, in: *AIAA 23rd Aerospace Science Meeting*, Reno, Nevada, January 1985.
- [77] R.N. Gupta, J.M. Yos, R.A. Thompson, K.-P. Lee, *A Review of Reaction Rates and Thermodynamic and Transport Properties for an 11-Species Air Model for Chemical and Thermal Nonequilibrium Calculations to 30 000 K*, NASA RP-1232, Washington, D.C., 1990.
- [78] F.G. Blottner, M. Johnson, M. Ellis, *Chemically Reacting Viscous Flow Program for Multi-Component Gas Mixtures*, Technical Report SC-RR-70-754, Sandia Laboratories, Albuquerque, New Mexico, 1971.

- [79] C.R. Wilke, A Viscosity Equation for Gas Mixtures, *The Journal of Chemical Physics*, Vol. 18, No.4, April 1950, pp.517-519.
- [80] J.O. Hirschfelder, Generalization of the Eucken Approximation for the Heat Conductivity of Polyatomic or Chemically Reacting Gas Mixtures, *Proceedings of the Joint Conference on Thermodynamic and Transport Properties of Fluids*, London, U.K., July 1957, pp. 133-141.
- [81] A. Klomfaß, S. Müller, J. Ballmann, Modelling of Transport Phenomena for the Hypersonic Stagnation Point Heat Transfer Problem, AIAA Paper 93-5047, in: *AIAA/DGLR Fifth International Aerospace Planes and Hypersonics Technologies Conference*, Munich, Germany, November-December 1993.
- [82] R.G. LeVeque, *Finite Volume Methods for Hyperbolic Problems*, Cambridge University Press, Cambridge, U.K., 2002. – ISBN 0-521-00924-3.
- [83] D. Hänel, R. Schwane, G. Seider, On the Accuracy of Upwind Schemes for Solution of Navier-Stokes Equations, AIAA Paper 87-1105, 1987.
- [84] N. Kroll, R. Radespiel, An Improved Flux Vector Discretisation Scheme for Viscous Flows, DLR-FB-93-53, DLR, Brunswick, Germany, 1993.
- [85] Y. Wada, M.-S. Liu, A Flux Splitting Scheme with High-Resolution and Robustness for Discontinuities, AIAA Paper 94-0083, in: *AIAA 32nd Aerospace Science Meeting and Exhibit*, Reno, Nevada, January 1994.
- [86] M.N. Macrossian, The Equilibrium Flux Method for the Calculation of Flows with Non-Equilibrium Chemical Reactions, *Journal of Computational Physics*, Vol. 80, No.1, January 1989, pp. 204-231.
- [87] M. Galle, Ein Verfahren zur Numerischen Simulation kompressibler, reibungsbehafteter Strömungen auf hybriden Netzen, DLR-FB-99-04, DLR, Brunswick, Germany, 1999
- [88] T. Gerhold, O. Friedrich, J. Evans, M. Galle, Calculation of Complex Three-Dimensional Configurations Employing the DLR TAU-Code, AIAA 97-0167, 1997.

Bibliography

- [89] A. Mack, V. Hannemann, Validation of the Unstructured DLR-TAU-Code for Hypersonic Flows, AIAA Paper 2002-3111, in: *AIAA 32nd Fluid Dynamics Conference*, St. Louis, Missouri, June 2002.
- [90] A. Jameson, W. Schmidt, E. Turkel, Numerical Solutions of the Euler Equations by the Finite Volume Methods using Runge-Kutta Time-Stepping Schemes, AIAA Paper 81-1259, in: *AIAA 14th Fluid and Plasma Dynamics Conference*, Palo Alto, California, June 1981.
- [91] A. Gülhan, Arc-Heated Facility LBK as a Tool to Study High Temperature Phenomena at Re-entry Conditions, DLR-IB-39113-97A05, DLR, Cologne, Germany, 1997.
- [92] B. Esser, A. Gülhan, Flow Field Characterisation of DLR's Arc-Heated Facilities L2K and L3K, ESA SP-426, in: *Third European Symposium on Aerothermodynamics for Space Vehicles*, Noordwijk, Netherlands, November 1998.
- [93] A. Mack, E. Emran, R. Schäfer, Numerical Rebuilding of a Generic Body-Flap Model in an Arc-Heated Facility, in H.-J. Rath, C. Holze, H.-J. Heinemann, R. Henke, H. Hönliger (eds.): *New Results in Numerical and Experimental Fluid Mechanics V*, Springer-Verlag, Berlin-Heidelberg, Germany, 2006, pp. 289-296 – ISBN 3-540-33286-3.
- [94] D. Weber, M. Nau, Elektrische Temperaturmessung, M.K. Junchheim, Fulda, Germany, 1991. – BR 146.
- [95] A. Gülhan, Application of Pyrometry and IR-Thermography to High Surface Temperature Measurements, RTO-EN-8, in: *RTO AVT Course on "Measurement Techniques for High Enthalpy and Plasma Flows"*, Rhode-St-Genèse, Belgium, October 1999.
- [96] Aachener Quarz-Glas Technologie Heinrich, Quarzglas für die Optik. - Daten und Eigenschaften, Aachen, Germany, 1995. – HQS-SO-DB-05.05.
- [97] http://eom.umicore.com/en/optics/products/coatings/show_coating_Germanium_UCS_01.pdf
- [98] <http://www.korth.de/de/503728952d091450d/503728952d0a21a25.htm>.

- [99] Anlage zur Messung des Gesamtemissionsgrades und des spektralen Emissionsgrads, Institut für Kernenergetik und Energiesysteme, Stuttgart, Germany, 2001. – FB IKE 5TB-207D-G.
- [100] A. Gülhan, Introduction to Pyrometry and Comparison of Different Pyrometer Configurations, VKI Lecture Series on Temperature Measurements, Von Karman Institute, Rhode-St-Genèse, Belgium, April 1996.
- [101] Dr. George Maurer GmbH - Optoelektronik, MAURER-Infrarot-Quotientenpyrometer Typ QKTR 1485, Kohlberg, Germany, 1998.
- [102] Dr. George Maurer GmbH - Optoelektronik, MAURER-2-Farben-Quotienten-Pyrometer Typ QPMRS 65-2-d, Kohlberg, Germany, 1990.
- [103] Dr. George Maurer GmbH - Optoelektronik, MAURER-Infrarot-Strahlungspyrometer Typ KTR-1485-Z, Kohlberg, Germany, 1998.
- [104] Dr. George Maurer GmbH - Optoelektronik, MAURER-Infrarot-Strahlungspyrometer Typ TMRS 85-2-d, Kohlberg, Germany, 1990.
- [105] Land Infrared, MINOLTA/LAND Cyclops 152/152A, Sheffield, England, 1993. – BDA/C152/01.93.
- [106] Land Instruments GmbH, CERTIFICATE OF CALIBRATION 16396, Leverkusen, Germany, September 2006.
- [107] Y. LeSant, M. Marchand, P. Millan, J. Fontaine, An Overview of Infrared Thermography Techniques Used in Large Wind Tunnels, *Aerospace Science and Technology*, Vol. 6, No. 5, September 2002, pp. 355-366.
- [108] AGEMA Infrared Systems AB, Thermovision 570 Operating Manual, Danderyd, Sweden, 1996.
- [109] Land Infrared, Landcal Blackbody Source Type R1500T Operating Instructions, Sheffield, England, 1996 – R1500T/0396.
- [110] CentaurSoft, Online User Manual – CENTAUR v7.0.
- [111] B. Esser, Private communication, 2009.